Bulk Laser Material Modification:

Towards a Kerfless Laser Wafering Process

by

James LeBeau

A Dissertation Presented in Partial Fulfillment
of the Requirements for the Degree
Doctor of Philosophy

Approved August 2015 by the
Graduate Supervisory Committee:

Stuart Bowden, Chair
Christiana Honsberg
Mariana Bertoni
Jeffrey Cotter

ARIZONA STATE UNIVERSITY

December 2015

ABSTRACT

Due to the ever increasing relevance of finer machining control as well as necessary reduction in material waste by large area semiconductor device manufacturers, a novel bulk laser machining method was investigated. Because the cost of silicon and sapphire substrates are limiting to the reduction in cost of devices in both the light emitting diode (LED) and solar industries, and the present substrate wafering process results in >50% waste, the need for an improved ingot wafering technique exists.

The focus of this work is the design and understanding of a novel semiconductor wafering technique that utilizes the nonlinear absorption properties of band-gapped materials to achieve bulk (subsurface) morphological changes in matter using highly focused laser light. A method and tool was designed and developed to form controlled damage regions in the bulk of a crystalline sapphire wafer leaving the surfaces unaltered. The controllability of the subsurface damage geometry was investigated, and the effect of numerical aperture of the focusing optic, energy per pulse, wavelength, and number of pulses was characterized for a nanosecond pulse length variable wavelength Nd:YAG OPO laser.

A novel model was developed to describe the geometry of laser induced morphological changes in the bulk of semiconducting materials for nanosecond pulse lengths. The beam propagation aspect of the model was based on ray-optics, and the full Keldysh multiphoton photoionization theory in conjuncture with Thornber's and Drude's models for impact ionization were used to describe high fluence laser light absorption and carrier generation ultimately resulting in permanent material modification though strong electron-plasma absorption and plasma melting. Although the electron-plasma description of laser damage formation is usually reserved for extremely short laser pulses (<20 ps), this work shows that it can be adapted for longer pulses of up to tens of nanoseconds.

In addition to a model describing damage formation of sub-band gap energy laser light in semiconducting and transparent crystalline dielectrics, a novel nanosecond laser process was successfully realized to generate a thin plane of damage in the bulk of sapphire wafers. This was accomplished using high numerical aperture optics, a variable wavelength nanosecond laser source, and three-dimensional motorized precision stage control.

ACKNOWLEDGMENTS

The credit for this work is shared by many people and institutions for whom and which I am very grateful. There are a few key people and institutions I would like to individually thank. Firstly, I would like to thank Dr. Bowden for his support and unyieldingly triumphant good demeanor. His kindness and lightheartedness has won out in every interaction I have had with him as my advisor. I would also like to thank Dr. Bill Dauksher and Dr. Clarence Tracy for their endless willingness to assist and share their time and expertise. I would also like to thank the institutions of ASU, IGERT SUN, QESST and thus the DOE and NSF for the freedom, resource and direction to pursue new science that their support has provided. I would also like to thank Dr. Christiana Honsberg and Dr. Stephen Goodnick, for finding me and directing me into SPL. Lastly, I would like to thank Dr. Dieter Schroder. I have had good instructors over my many years as a student, yet he surpasses them all.

Despite all the invaluable insight, direction, and support provided by the wonderful groups of people and systems I have been researching under for the past four years, the real credit for the completion of this work goes to my wife and son. Without the fire under my seat, set by my wife’s love and my son’s new existence, I’m afraid I might have never wanted to finish this dissertation.

Very lastly and firstly, I want to thank God for this gift of life -this wondrous puzzle that I certainly cannot piece together alone, especially without Your help.

TABLE OF CONTENTS

Page

LIST OF TABLES

LIST OF FIGURES

Figure Page

Figure Page

Figure Page

Figure Page

Chapter 1

INTRODUCTION

The original motivation for this dissertation was inspired by the need for cheaper and thinner silicon wafers. Due to the obvious importance of vastly increasing the use of renewable energy sources, and the present inhibitory capital cost of silicon based photovoltaics, novel methods to reduce the overall cost of solar cells have become pivotal research topics [1, 2]. The substantial cost of the present wafering technology (wire sawing) and the cost of material waste due to kerf loss will be discussed further in a later chapter. It is the goal of this work to present a laser based solution to the well-defined opportunity of lower cost semiconductor and crystalline dielectric wafers. The process is termed "laser wafering" and is a novel noncontact subsurface laser machining process. The following work revolves around the concept of laser wafering; a technique that uses the nonlinear absorption properties of semiconductors and crystalline dielectrics to produce damage in the bulk of a material leaving the surfaces unchanged. By focusing high intensity sub-band gap laser light into the bulk of a material at high enough focus, permanent subsurface damage can be created. If the damage pits are formed in a thin plane, a layer liftoff method could be used to generate a wafer with limited kerf loss. The following chapter presents first an introduction to the facilitating tool, the laser, and the motivation for this work. Chapter 2 discusses some of the fundamental light-material interactions that govern the absorption of laser radiation as well as some of the more advanced nonlinear interaction concepts. A novel optical model that successfully predicts the generation and geometry of subsurface damage in sapphire is presented in

Chapter 3. Chapter 4 presents and discusses the experimental results found characterizing the control of subsurface damage geometry and compares the observed modified material volumes to predictions from the models. Chapter 5 details how subsurface arrays of damage were successfully formed in the bulk of crystalline sapphire as well as the failed attempts at layer liftoff. The conclusion and suggested future direction of this work are presented in Chapter 6.

1.1 Lasers: A Brief History

The origin of the Laser (Light Amplification by Stimulated Emission of Radiation) can be tied to developments made in radio wave technology and radar science in the early 20th century. The first laser-like device operating at microwave wavelengths was the Maser. Its invention can be attributed to Charles Townes and Arthur Schawlow in 1954, but the first optical light laser was not built until 1960 by Theodore Maiman [3]. Like many revolutionary inventions, the actual credit of invention is muddled and not the result of one person's effort. Gordon Gould was performing parallel work on excitation of molecules to produce coherent light, and the first use of the term "LASER" is attributed to him. Once the concept of coherent light amplification based on multimode optical masers was published by Schawlow and Townes [4] in 1958, it took another two years for the first successful proof of concept- the ruby laser- to be completed by Maiman [3]. Since its invention, many types of lasers have been developed and implemented in a wide range of applications. The main laser technologies can be categorized as gas, solid state, semiconductor, dye, and chemical lasers. The categorizations refer to the active medium in the light amplification and optical feedback system [5].

1.1.1 Basics of Lasing

Lasing happens when stimulated emission occurs in an active medium producing amplified coherent light through optical feedback. Stimulated emission can only happen when there is population inversion, and this occurs when a large enough population of atoms in a given material volume is at an energetically excited state. Spontaneous emission can occur when an atom is at this excited state, and the resulting photon can then cause stimulated emission- a process where an excited atom relaxes due to stimulation from an incident photon. Stimulated emission results in two photons of the same energy and phase; the process is called optical amplification [6]. Coherence occurs because photons resulting from stimulated emission have the same phase and direction. The basic components of a laser include an active medium, pump source, and optical resonator. The active medium is where population inversion occurs and amplified coherent light is formed. The pump source causes population inversion by providing energy to atoms resulting in occupation of excited states. The optical resonator provides optical feedback such that stimulated emission and amplification can occur in the active medium. Figure 1 is a diagram of the basic laser components necessary to form amplified coherent light.

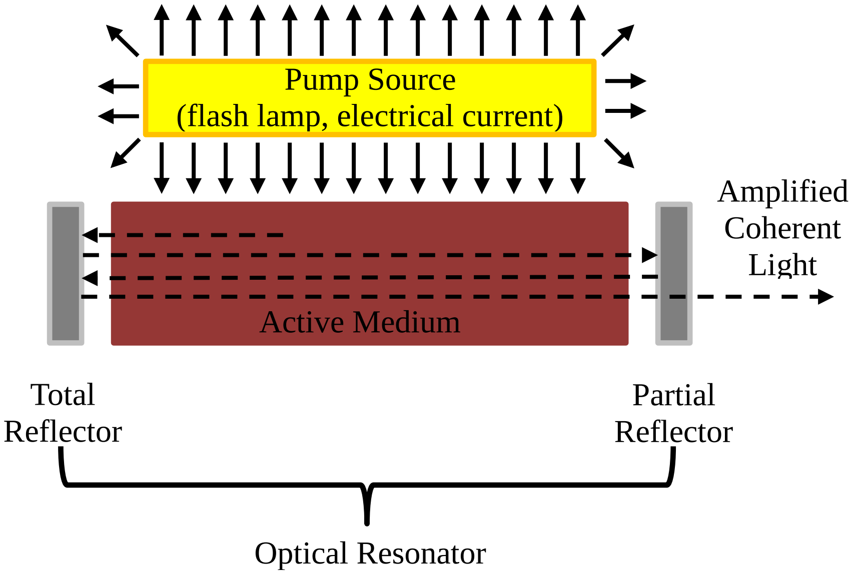

Figure 1**:** Diagram of basic laser components.

Depending of the type of laser, the pump source can be a flash lamp, electrical current, or even another laser source. As mentioned earlier, the active medium can be a solid, liquid, or gas. Common solid-state lasers include ruby, Ti:Sapphire, or Nd:YAG- the laser used in the following experiments. Other solid phase active medium lasers are classified as semiconductor lasers, and these are largely referred to as diode lasers. Common gas lasers are HeNe, CO_2, or excimer lasers. The most common liquid active mediums are found in dye lasers and chemical lasers. Regardless of the active medium, all lasers must have some sort of optical resonator or feedback structure, active medium and pump source to produce amplified coherent light.

Figure 2 shows the basic energy diagram and photon processes correlating with laser light generation. The actual number of energy levels depends on the particular laser and its active medium.

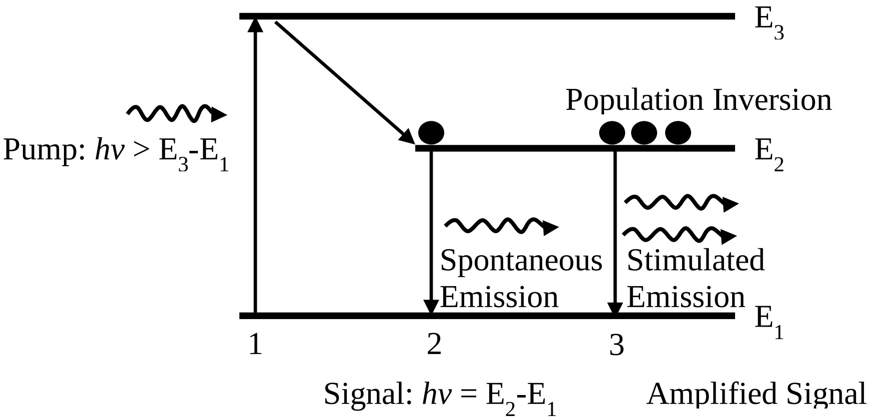

Figure 2**:** Generic energy diagram of active medium.

The pump source provides the energy necessary to cause population inversion. In the diagramed case it is a flash lamp providing a high energy photon. First, the pump photon is absorbed in the active medium and an atom is raised to an excited state E_3. The atom then decays to a more stable excited energy state at a lower energy level E_2. When enough atoms have absorbed pump photon energy and are at the energy level E_2, population inversion occurs. When one excited atom decays and one photon is spontaneously emitted, this photon can now cause stimulated emission of the same phase and coherence. The photons resulting from stimulated emission are fed back through the active medium due to the reflectors until some of the photons escape through the partial reflector as amplified coherent light or a laser beam.

1.1.2 Laser Market Growth

Since the first successful generation of laser light in 1960, the laser has become a widely used device in many areas of manufacturing, medicine, research, communications and other commercial and scientific applications. Like other semiconductor technologies, the laser industry has seen exponential growth since the late 1960s (see Figure 3).

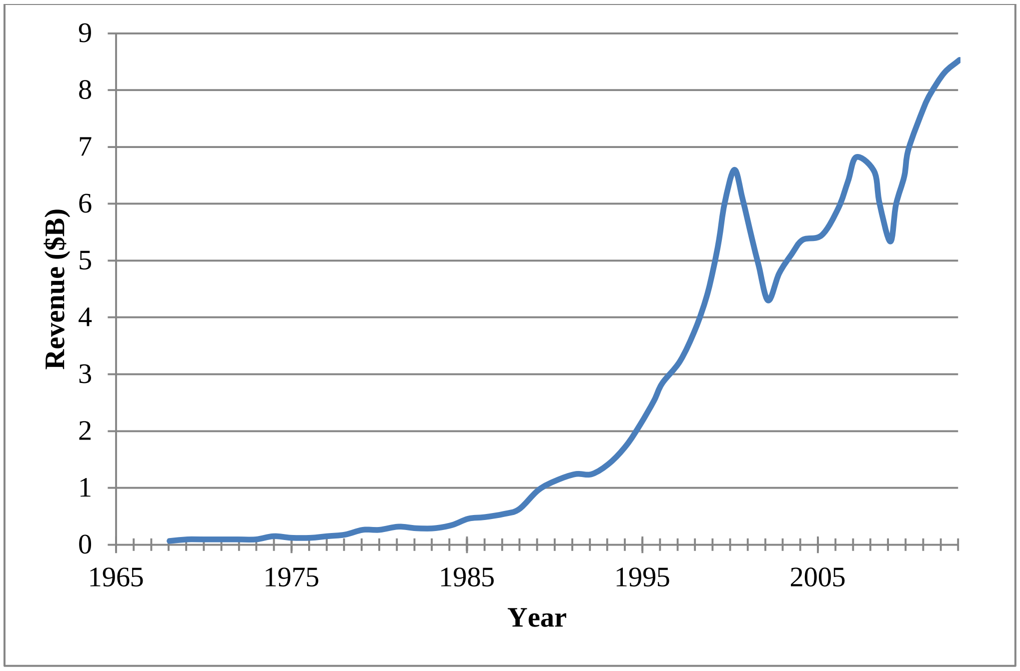

Figure 3: Historical laser market revenue since 1968 [7].

The first application of lasers was in scientific research as a metrology tool and probe used to better understand atomic physics and light-material interaction. Barcode scanning and the laser disc in the 1970s, as well as the compact disc in the 1980s were the first major commercially available applications of the laser [8]. Since their first commercial applications, laser systems have become a hugely successful and enabling technology. As seen in Figure 4, the laser is used in a plethora of market segments, and its applications continue to expand.

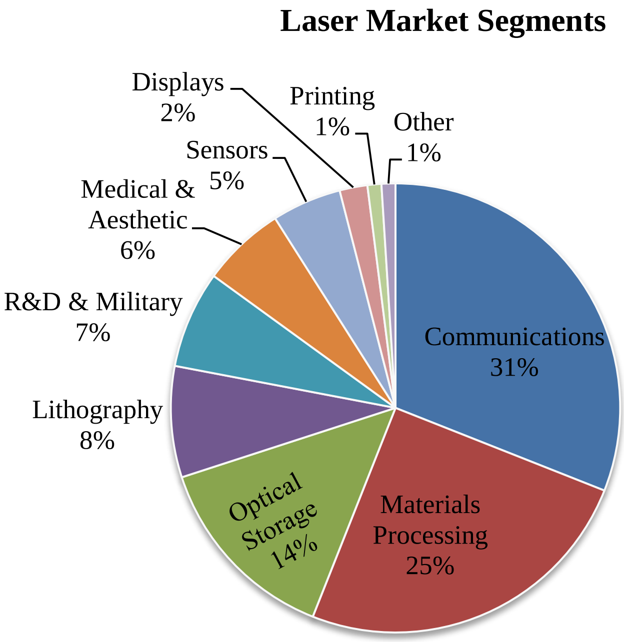

Figure 4: Laser market application segments as a percentage of total laser market in 2013 [7].

According to the "Worldwide Market for Lasers: Market Review and Forecast", the largest market segments in 2013 were communications, materials processing, optical storage and lithography. The majority of laser systems in the communications sector are diode and fiber lasers for fiber-optic communications and data transmission. The materials processing segment applies a wide variety of laser systems dominated by CO_2, solid state lasers and fiber lasers for marking, welding, dicing, annealing, and other bulk materials processing needs. Optical storage refers mainly to the market segment including DVD, CD, and Blu-ray disc readers and writers. The lasers used in optical storage are mostly diode lasers, and although on a steady decline in popularity, optical storage still holds a large portion of the laser market. Lithography is a smaller but quickly growing area of laser application-specifically excimer lasers. The excimer laser is a very low wavelength laser (<100 nm) that allows smaller and smaller feature sizes to be made in IC manufacturing. Because it is the topic of this research, materials processing is the market segment of scope. Since its invention, the laser has been used as a metrology tool, but not until the last few decades has its value in materials processing become known. The laser has become a robust and reliable manufacturing tool through rapid industrialization. The largest laser market revenue comes from applications like laser cutting in automotive manufacturing, laser marking tools, and microelectronics processing for displays [7] and die cutting [9, 10, 11, 12]. Many of the materials processing applications of laser systems can be categorized as laser machining; especially uses like drilling, cutting, welding, and micromachining.

1.2 Laser Machining

Laser machining is an umbrella term used to describe any laser process that changes the physical shape or geometry of a material or material system. As mentioned earlier, some laser machining applications include: cutting, scribing, marking, patterning and drilling. Because of the nature of light, particularly having no volume, tight focus of enormous amounts of energy is possible ($>1\text{GW/cm}^2$). This allows for the permanent change of a material structure in a non-contact manner. Laser melting or vaporization of material is a thermal (now also non-thermal) process that depends on both the optical and thermal properties of a material instead of the mechanical properties. The non-contact nature of laser machining allows for less machine vibration and tool wear. Laser light replaces traditional drill bits or saw blades that wear out, reducing the need for tool replacement and recalibration [13]. The most fundamental application of laser machining is laser drilling. This process involves the focusing of laser light onto the surface of a material at high enough fluence (beam energy per unit area-J/cm^2) to remove material through melting, boiling, and/or ablation. Many other aspects of laser machining can be described by the physics of laser drilling. Figure 5 shows the basic material interactions taking place during laser drilling.

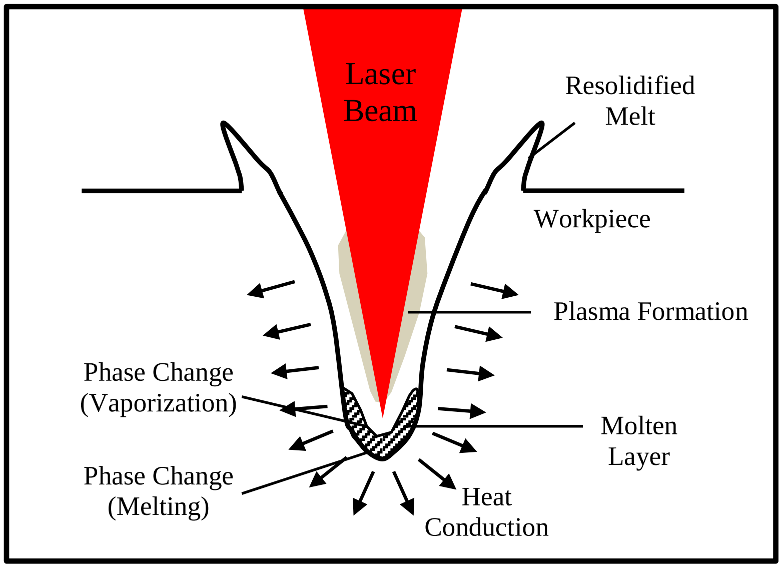

Figure 5: Diagram of laser drilling process [13].

Laser drilling, and thus laser cutting and patterning, is a result of the phase change of a material in the presence of very high light energy density. The coherence of laser light allows it to be focused to small spot sizes and thus generates very high energy density allowing for melting and evaporation of material placed in the focal path. If the laser pulse length is on the 10 ps or greater time scale, the material modification is traditionally described as the result of thermal breaking of bonds and occurs as illustrated in Figure 5. If the pulse is less than 10 ps, as many industrial femtosecond pulses are now capable of, heat conduction negligible and non-thermal melting takes place [14, 15, 16]. Non-thermal melting allows for finer machining resolution and cleaner cuts.

An experiment was done to observe the machinability of silicon using femtosecond-pulsed lasers vs. nanosecond-pulsed lasers in order to assist in the laser system purchase process. A Spectra Physics Ti:Sapphire 140 fs pulse length laser at 1 kHz repetition rate and a wavelength of 1200 nm as well as an Ekspla NT-342A 8 ns pulse length laser operating at 10 Hz and 1200 nm wavelength were used to ablate the surface of a 4" polished silicon wafer. The average power for both systems was around 30 mW and the focusing objective was a 0.28 numerical aperture reflective objective with a gold protective coating. The silicon wafer was fixed to a mechanical stage and placed at the focal point of the respective beam. The wafer was exposed for 1 s; i.e. 10 pulses for the nanosecond laser and 1000 pulses for the femtosecond laser. Following are optical microscope images of the silicon surface showing laser drilling from the femtosecond and nanosecond-pulsed lasers using the same focus and average power (see Figure 6).

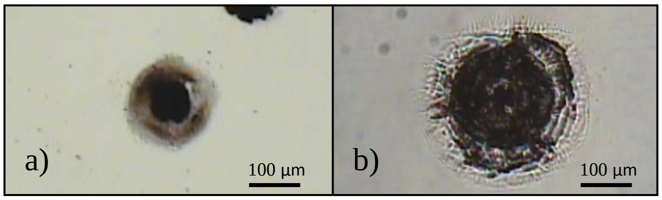

Figure 6: Surface ablation in silicon for a) 140 fs pulse and b) 6 ns pulse.

Both lasers successfully ablated the silicon wafer at and around the focal point of the beam. The thermal effects from diffusion and molten ejection can be readily seen in the optical microscope image of the nanosecond-pulsed hole. The affected area is much larger due to thermal diffusion, and the walls at the edge of the hole show cracking and slag from thermal induced stress and resolidification. On the other hand, the hole generated by the femtosecond pulsed laser is cleaner and displays much more machining precision. Because the femtosecond pulse operates on a time scale where heat cannot be transferred to the material, or phonon scattering is negligible, the phase change is theorized to be substantially electrical; the result of extremely high numbers of excited electrons having enough energy to break bonds between atoms, and is called non-thermal melting [17]. Non-thermal melting will be discussed further in Section 2.5. Ultimately, this study reinforced what other have already stated; if precise and small modified spot sizes are desired, and it can be afforded, a femtosecond laser is the tool of choice [18]. However if more bulk modification is desired at a much lower cost, a nanosecond pulsed laser will certainly do the job [19]. The latter was chosen as a research tool in the development of our novel laser wafering process.

1.2.1 Motivation

Comprising much of the Earth's crust, silicon (Si) is one of the planet's most abundant elements [20]. It is a semiconductor of great use and value, and is the fundamental building block to hundreds of billions of dollars of integrated circuits (IC) and other semiconductor technologies. A quickly growing and widely proven mostly-silicon based technology is photovoltaics (PV). As a 100bil USD industry in 2013; twenty times what it was in 2003, solar PV proves to be an important and viable technology. The PV market is dominated by silicon based technologies at more than 85% market share [21], and one of the most costly entities for a solar module is the silicon wafer on which the solar cell is built; accounting for $0.45 of the 0.77 $/Watt of the standard silicon solar cell cost [1, 22]. Wafer growth and fabrication is a complex and costly process and rightly accounts for high cost. Mono-crystalline silicon is slowly grown form a vat of molten, incredibly pure, polysilicon in a process called the Czochralski growth method. The resulting boule is then cropped into a pseudo-square ingot and adhered to a chuck for wafering by slurry or diamond wire saw. The wafering process accounts for a large cost in capital equipment, and operational wire or slurry costs, but it is the kerf loss from sawing that is most costly. About 55% of the ingot is mostly-irrevocably lost to kerf from the diameter of the wire [23]. Because the highest material cost contributor towards silicon wafer formation is the incredibly pure polysilicon, and half of this material is wasted as kerf, the wire sawing process can be considered the largest cost contributor to the final mono-silicon wafer. The implementation of thin silicon kerfless wafering could result in half to a third the final solar cell cost according to NREL [1]. As stated earlier, the origin of the laser wafering project came from this market opportunity.

The original concept for laser wafering stemmed from a well-known need for thinner and cheaper silicon wafers. As one of the main contributors towards silicon-PV dollars-per-watt cost, novel wafering techniques reducing the cost of the mono-silicon wafers could be a very disruptive technology. This is not a new idea; many groups and large investments have been made in the pursuit of low cost kerfless wafering techniques. Companies like Solexiel, 1366 Technologies, Twin Creeks and SiGen have all attempted to design and implement cost competitive methods to generate kerfless silicon wafers [24]. Many of these companies have gone bankrupt, but much success and progress has been made towards the realization of kerfless thin silicon. One of the most similar technologies to laser wafering is the H^+ ion beam implantation and cleaving techniques developed by SiGen and Twin Creeks. The process involves the implantation of protons at a constant depth inside a thick (>400 µm) silicon wafer or brick with a subsequent thermal process to lift a thin (~20 µm) wafer off of the silicon base [24]. Because the base can be reused, this process is truly kerfless. However, extremely high capital costs and low material performance have hindered its adoption into standard PV manufacturing environments.

Our concept aims to eliminate the need for high cost proton implanters, and instead use light as the medium to create atomic disorder and change the material morphology at a specified depth below the surface of a wafer [25]. Because of the non-linear absorption properties of semiconductors and some transparent insulators, laser light that is transparent to the medium at low intensities is absorbed at high intensities and can cause melting or vaporization. By focusing the laser light to a small enough area beneath the surface of a material, damage could be formed inside the material without affecting the surfaces. If a plane of damage is formed, a layer of material could then be lifted off. Figure 7 shows the basic process concept for laser wafering

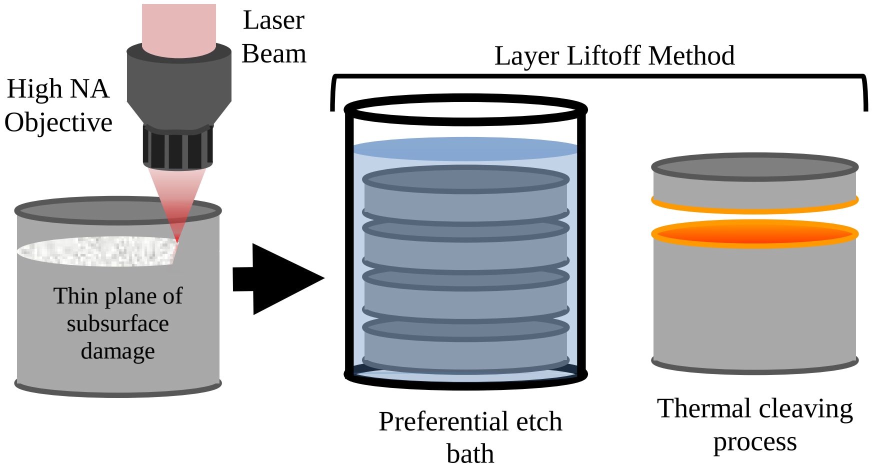

Figure 7: Schematic of laser wafering and layer liftoff process.

After a plane of damage is generated inside a block of the material, a preferential etch bath or thermal or mechanical cleaving process can be used to lift the undamaged layers of material off. The physics, theory and application of subsurface damage formation using focused laser beams are the crux of this work.

Although mono-crystalline silicon was the original target application for this work, early on in the project other materials were pursued. After encountering some yet unresolved issues in imaging damage formed beneath the surface of a silicon wafer, other material applications were sought and sapphire was determined to be a useful candidate. Sapphire (Al_2O_3) is a widely used transparent crystalline dielectric in the LED (light emitting diode) industry as well as other semiconductor industries. Because of its low heat conductivity, high mechanical strength, optical transparency and insulating electrical properties, sapphire is an extremely prevalent and useful material. Sapphire wafers are the most commonly used substrates for LED manufacturing. Sapphire substrates provide a mechanically strong, optically transparent platform and a good epitaxial growth-ready surface for LED manufacturing. Because of optical transparency, it was assumed that permanent subsurface damage generated inside sapphire wafers would be readily visible through optical microscopy. Thus sapphire laser wafering became another area of investigation and potential opportunity for novel science; believing that it would help expose the physics of subsurface laser machining for crystalline transparent dielectrics and semiconductors as well.

Chapter 2

LIGHT MATERIAL INTERACTION

This chapter will present the physics of light absorption by a semiconductor or transparent crystalline insulator. Both linear and non-linear light material interaction will be discussed, particularly the nonlinear refractive index as well as non-linear absorption in the form of multiphoton processes. In this context, non-linear refers to the light intensity dependence of the absorption or refraction phenomena. This chapter will also cover an introduction to the most popular model describing high fluence light material interaction called the Keldysh multiphoton photoionization theory.

2.1 Fundamentals of Light

In order to better understand the interaction of laser light and crystalline materials like sapphire and silicon at high intensity, where non-linear effects become important, the groundwork of linear interactions will be presented. A background of the history and basics of important light-material interactions, especially absorption, have been included in the following section.

2.1.1 Particle-Wave Duality

Light and all other forms of electro-magnetic radiation have been modeled historically with a duality described by wave and particle-like behavior. Classic Newtonian physics was traditionally used to model light as a particle only. However in the late 18th century, Thomas Young definitively showed the wave-nature of light through double slit experiments and resulting interference and diffraction patterns. The wave-nature of light is now classically described by Maxwell's equations for electro-magnetic radiation. A commonly used solution to the Maxwell equations that describes light propagation, especially coherent light, is a plane wave. For a nonmagnetic material, the instantaneous energy as a function of position and time for plane-wave propagation of light can be written as [26]:

$$\mathcal{E}(r,t) = \mathcal{E}_o exp\left[i\omega\left(\frac{N(\omega)}{c}\hat{k}\cdot r - t\right)\right] \tag{1}$$

where $\mathcal{E}_o$ is the electric field amplitude, the angular frequency of the light is $\omega = 2\pi v$ where v is the light frequency, $N(\omega)$ is the refractive index as a function of angular frequency, and $\hat{k}$ is the unit vector in the direction of the propagation vector k. The frequency dependence of the refractive index $N(\omega)$ is a complex number described by [26]:

$$N(\omega) = n(\omega) + iK(\omega) \tag{2}$$

where $n(\omega)$ is the real part of the refractive index related to the velocity of light propagating in a material [27], and $K(\omega)$ is the complex portion of the refractive index called the extinction coefficient and is related to the absorption coefficient.

The absorption coefficient is defined as the inverse of the distance an electromagnetic wave must travel in order for its intensity to decrease by a factor of 1/*e* [26]. Taking the square of the magnitude of the electric field given in eq. 1 the absorption coefficient can be solved as [26]:

$$\alpha(\omega) = \frac{2\omega K(\omega)}{c} \tag{3}$$

where c is the speed of light.

From a particle point of view, light energy was extrapolated from Plank's work on black body radiation and postulated by Einstein to be quantized as a photon of energy [28]:

$$E = \frac{hc}{\lambda} = hv = h\frac{\omega}{2\pi} \tag{4}$$

where h is Plank's constant, c is the speed of light, λ is the wavelength of the light in vacuum, v is the frequency of the light in vacuum and ω is the angular frequency of the light in vacuum. The energy of light was originally used to explain the photo-electric effect, and how even at high intensity, certain wavelengths of light incident on a metal substrate could not free electrons where shorter wavelengths could.

2.2 Light Absorption in Semiconductors

The interaction of light and material has long been an important area of study for many applications. From the observation of the thermal energy provided by sun light to the widespread use of high-speed fiber optic data communication, the light material interaction is fundamental to many aspects of science and technology. From a geometric or ray optics perspective, the basic light material interactions can be summarized as light propagating through a medium, incident on an optical material. The light is reflected, absorbed and transmitted through the material and complies with energy conservation such that:

$$\rho + \tau + a = 1 \tag{5}$$

where ρ is the reflectance, τ is the transmission and a is the absorptance (not to be confused with the absorption coefficient, α, usually given in cm^{-1}). Reflectance is the process by which some of the incident light is reflected off the surface of a material in a diffuse or regular fashion and is the ratio of the reflected flux to the incident flux. Absorptance is the process where the light energy is converted into another energy (heat or electrical) in the material. Absorptance is the ratio of the absorbed flux to the incident flux. Transmittance is the process by which light leaves a material having passed through some amount of bulk material. It is the ratio of transmitted flux to incident flux. Thus the reflectance, transmittance and absorptance are dimensionless numbers less than or equal to one. A diagram of the model case of light transmission and reflection can be seen in Figure 8.

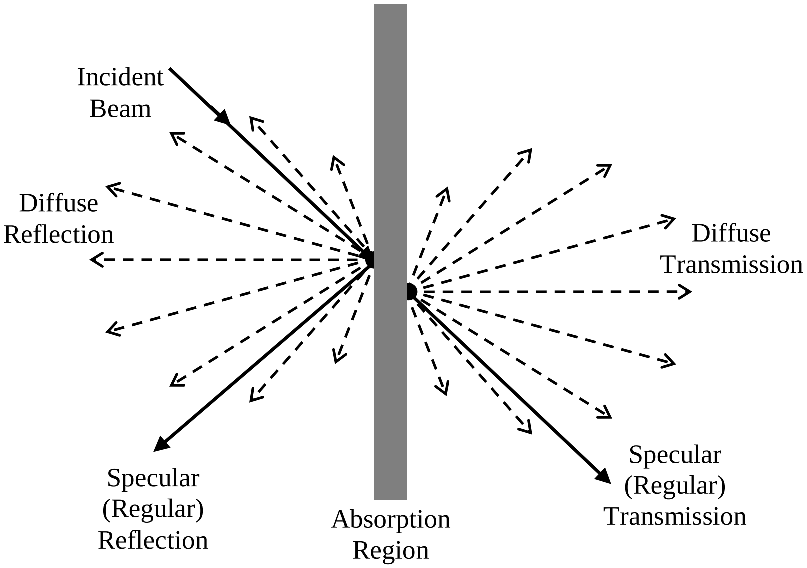

Figure 8: Reflection and absorption of incident light beam [29].

For very polished or microscopically even-surfaced materials, the majority of reflectance and transmittance is specular or regular, and it is diffuse for rough or unpolished surfaces. The research area proposed in this writing is most concerned with the absorption processes of semiconductors and wide band transparent materials. Thus, a straightforward way to quantify the absorption of radiant light in a material is to measure the incident, reflected and transmitted beams. Beer-Lambert absorption is a material thickness (L) and wavelength (λ) dependent absorption that uses the absorption coefficient (α), usually measured in cm^{-1}, to quantify the distance it takes for light of a particular wavelength to be statistically absorbed inside a given material. The transmitted flux can be calculated as:

$$I_T = I_o(1-R)^2 e^{-\alpha(\lambda)L} \tag{6}$$

where I_o is the incident light flux or irradiance, R is the reflectivity calculated from the Fresnel equations of s- and p-polarized light. For normal incidence,

$$R = \left(\frac{n_1 - n_2}{n_1 + n_2}\right)^2 \tag{7}$$

where n_1 and n_2 are the real part of the refractive index for the medium and material respectively. The process of measuring absorption will be further discussed in section 2.3.

2.2.1 Fundamental Absorption

Fundamental absorption is the transferring of photon energy to excitation of electron from valence band to conduction band. This kind of absorption is dependent on the energy of the incident photon as well as the density of states and band structure of a material. For direct band-gap semiconductors, like gallium arsenide (GaAs), the interband transitions involve one photon and one electron. For indirect band-gap semiconductors, like silicon (Si), the transition involves one photon and one or more phonons (quanta of thermal or vibrational lattice energy). A phonon can give or take energy from the photon (phonon absorption or emission) to assist in fundamental absorption allowing momentum conservation requirements to be met. Opposite of a photon, the momentum of a phonon is high relative to its energy. As seen in Figure 9, the energy of the photon must be greater than or equal to the band-gap for direct photon absorption and the sum of the energy of the photon and the assisting phonon must be greater or equal to the band-gap for indirect transitions.

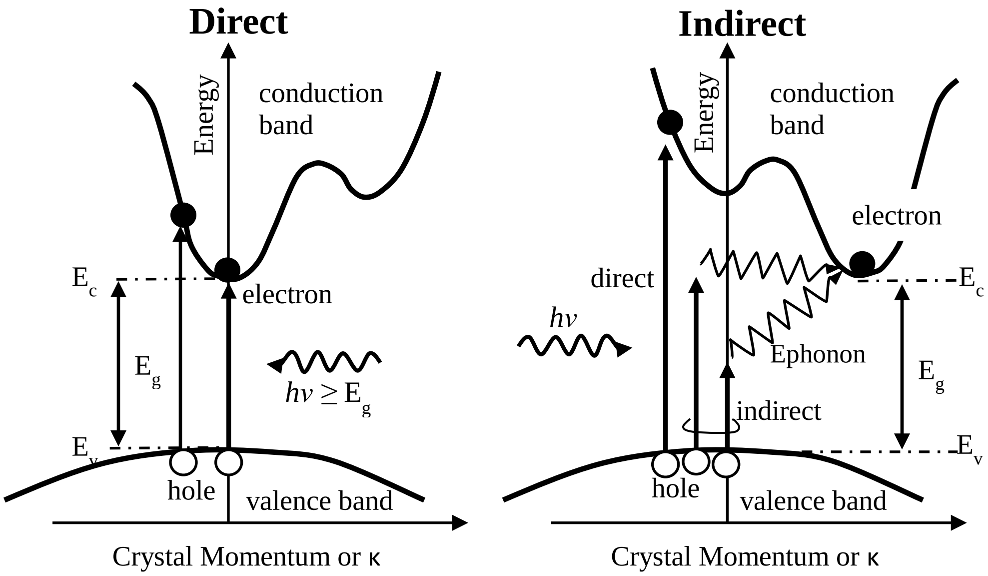

Figure 9: Diagram of fundamental photon absorption process in direct and indirect band semiconductors [30].

Indirect band-gap materials like silicon usually have lower absorption coefficients than direct band materials because of the added requirement of phonon assistance. Direct and indirect band semiconductors both allow phonon assisted absorption, which causes the absorption vs. wavelength plot to stretch around the absorption edge or band-gap and is known as the Urbach tail. This feature is proportional to temperature and is due to band tailing as a result of disorder in the lattice; both structural and thermal. The Urbach tail is also dependent on local dopant concentration, defects, and anything that would cause localized fluctuations in potential and thus cause band-gap variations. Figure 10 shows the absorption spectrum of direct and indirect band-gap semiconductors including the Urbach tail which will be discussed more in the following section.

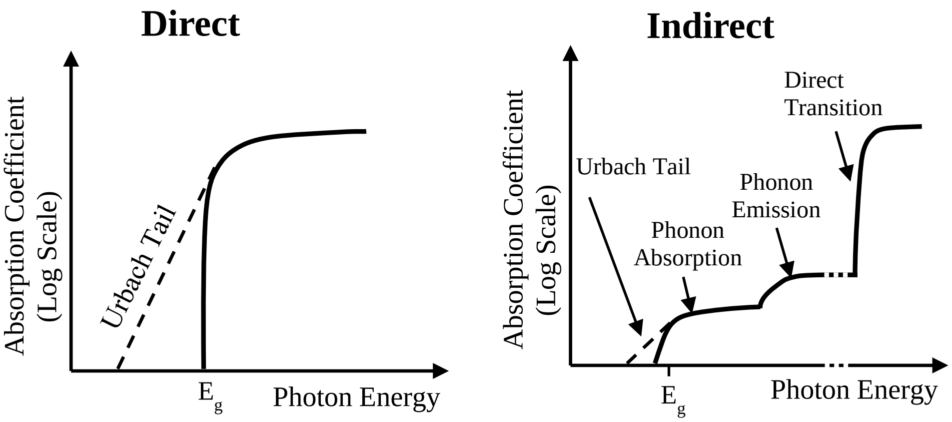

Figure 10: Absorption coefficient for direct and indirect band semiconductors as a function of photon energy [3].

An ideal direct band semiconductor would not absorb sub-band energy photons ($h\nu \leq E_g$). With a parabolic band approximation, the absorption coefficient as a function of photon energy can be obtained from the integral of the joint density of states [31]. Such that the absorption coefficient can be calculated as:

$$\alpha(h\nu) = A(h\nu - E_g)^{1/2} \tag{8}$$

where $h\nu$ is the photon energy, E_g is the band-gap of the semiconductor and A is an experimentally fit constant but can also be calculated as [32]:

$$A \approx \frac{q^2\left(2\frac{m_h^* m_e^*}{m_h^* + m_e^*}\right)^{3/2}}{nch^2 m_e^*} \tag{9}$$

where q is the electron charge, m_h^* is the hole effective mass, m_e^* is the electron effective mass, n is the refractive index, c is the speed of light, and h is Plank's constant. The shape of the direct band absorption curve can be seen in Figure 10. The solid curve shows that there is no absorption below the band-gap.

In an ideal indirect band semiconductor, the absorption from valence to conduction band requires phonon assistance. From Bose-Einstein statistics, the number of phonons at a given temperature can be calculated as:

$$f_{BE}(E_p) = \frac{1}{\exp\left(\frac{E_p}{k_b T}\right)-1} \tag{10}$$

where E_p is the phonon energy, k_b is the Boltzmann constant, and T is the temperature. Phonons can be emitted or absorbed to aid in transition from valence to conduction band. Such that the phonon absorption can be calculated as [31]:

$$\alpha_{absorption} = A[f_{BE}(E_p)](hv - E_g - E_p)^2\ ; hv > (E_g - E_p) \tag{11}$$

and the phonon emission can be calculated as [31]:

$$\alpha_{emission} = A[1 - f_{BE}(E_p)](hv - E_g + E_p)^2\ ; hv > (E_g + E_p) \tag{12}$$

where A is the constant mentioned earlier, hv is the photon energy, E_g is the band-gap, and E_p is the phonon energy. When the energy of the photon is greater than the energy difference between the band edge and the phonon energy but less than the sum of the band edge and the phonon energy, phonon absorption causes the transition from valence to conduction energy [31]:

$$\alpha(hv) = \alpha_{absorption} \tag{13}$$

When $hv > (E_g + E_p)$ phonon emission and absorption can take place, such that the absorption coefficient is [31]:

$$\alpha(hv) = \alpha_{absorption} + \alpha_{emission} \tag{14}$$

The shape of the absorption curve for indirect band semiconductors can be seen in Figure 10. The phonon absorption allows for some absorption of light below the band-gap, but only light that is the phonon energy below the band-gap. However, when the absorption coefficient is measured in real materials, there is absorption of light even at photon energies beneath the band-gap. In reality, the absorption coefficient is low beneath the band-gap of high purity materials, and increases exponentially until above band energy absorption can occur. This sub band energy absorption is due to defects, fluctuations in thermal energy, and variance in lattice vibrations causing localized changes in the band structure or band tails. On a logarithmic scale, the slope of $\alpha(hv)$ below the band-gap energy is seen to be proportional to k_bT and is called the Urbach tail of the absorption curve [33].

2.2.2 Urbach Tail Absorption

The Urbach tail, traditionally seen in absorption measurements of semiconductors and wide band-gap transparent crystals, is a result of band tailing around the band-gap of a material. Band tailing can be caused by local defects, impurities or doping, and its effects can be seen in the bad-gap's dependence on temperature and doping. The shape of the Urbach tail and its effect on the absorption coefficient below band-gap energies can be seen in Figure 10. The absorption coefficient can then be fit to the following equation in the Urbach tail region [34]:

$$\alpha(hv) = \alpha_g exp\left(\frac{hv-E_g}{E_o}\right) \tag{15}$$

where E_o is the characteristic energy of the Urbach edge (experimentally determined), E_g is the band-gap energy and α_g is the optical absorption coefficient at the band-gap energy. The characteristic energy E_o of the Urbach edge determines the slope of the $log(\alpha(hv))$

plot and is proportional to the number of defects, doping concentration [35], and temperature [36] (see Figure 11).

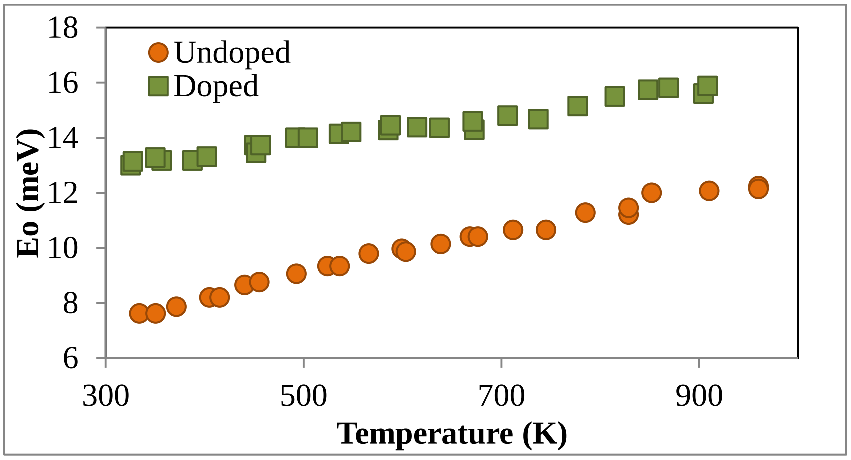

Figure 11: Characteristic energy of the Urbach edge Eo at varying temperature for doped and undoped GaAs [36].

As temperature and doping decrease, E_o decreases; thus reducing the amount of band tailing and non-ideal absorption effects. For very pure materials at very low temperature, the absorption curve at the band edge is close to ideal. However, at low temperature, low doping and high purity, another absorption effect becomes readably visible called excitonic absorption.

2.2.3 Excitonic Absorption

Excitonic absorption happens in semiconductors due to the coulombic interaction of an electron-hole pair called an exciton. A free exciton is an electrically neutral electron-hole pair able to move as a unit in the crystal while a bound exciton is one localized in the vicinity of an acceptor, donor, or neutral atom [30].   The exciton energy E_x is usually hundredths of milli-electron volts to a few milli-electron volts; allowing for a peak in the absorption spectrum beneath the band-gap of a semiconductor (see Figure 12) or transparent crystalline insulator at photon energy [37]:

$$hv = E_g - E_x/n^2, \quad n=1, 2, 3\ldots \tag{16}$$

for direct band semiconductors, and

$$hv = E_g - E_x/n^2 \pm E_p, \quad n=1, 2, 3\ldots \tag{17}$$

for indirect band semiconductors due to phonon emission and absorption respectively. Where n is the order of the exciton, and usually only the first order exciton is resolved in absorption studies: intensities being proportional to $1/n^3$ [37]. The following plot from Sturge shows the effect of excitonic absorption especially at low temperature on the absorption coefficient.

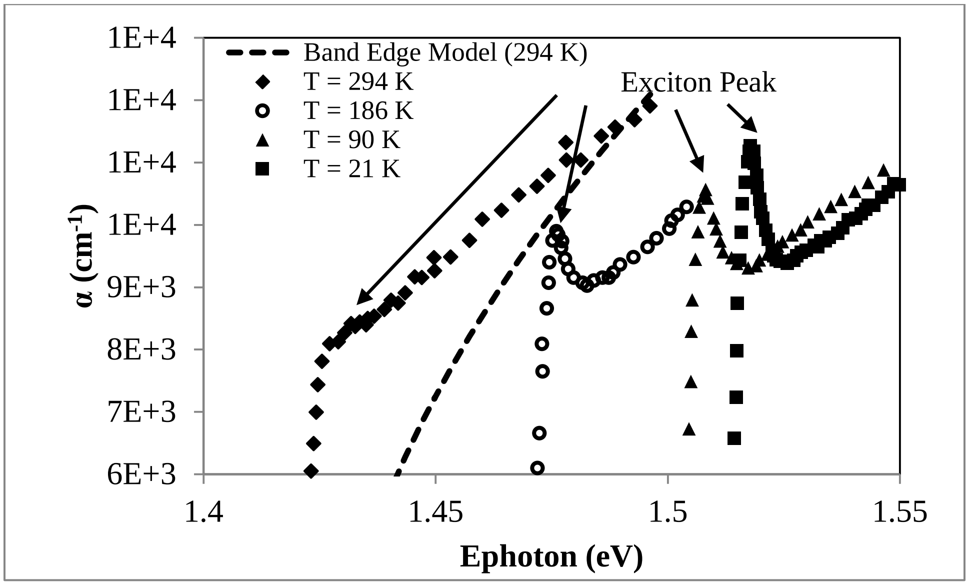

Figure 12: Absorption coefficient at the band edge in GaAs at varying temperature showing exciton peaks [38] compared to band-edge absorption model for direct band-gap semiconductors.

It can be seen that the exciton peak at room temperature is barely visible even in very pure GaAs. However the band stretching caused by the excitonic effect still affects absorption at the band edge despite the lack of a distinguishable peak at the excitonic binding energy. The increased absorption around the exciton binding energy can be seen when comparing the modeled direct band-gap absorption coefficient to the measured absorption even at room temperature (see Figure 12). Because of an increase in phonon assistance, free carriers, and thus band-gap narrowing at higher temperatures, the excitonic effect is blurred. However, at low temperatures, excitonic peaks become readily visible.

An accurate estimate of absorption as a function of photon energy including the excitonic effect at the band edge can be calculated from [38]:

$$\alpha(hv) = a^{*}(hv) f(z) \tag{18}$$

where $a^{*}(hv)$ is the absorption neglecting the excitonic effect, i.e. just band to band absorption or the fundamental absorption discussed earlier, and $f(z)$ is a factor taking the coulomb effect into account [38]:

$$f(z) = z \frac{exp(z)}{\sinh(z)} \tag{19}$$

and for direct band semiconductors,

$$z = \pi \left(\frac{E_x}{hv - E_g}\right)^{1/2} \tag{20}$$

for indirect band-gap semiconductors,

$$z = \pi \left(\frac{E_x}{hv - (E_g \pm E_p)}\right)^{1/2} \tag{21}$$

The exciton binding energy can be calculated from $E_x = m^* q^2 / 2\hbar^2 \kappa^2$, where m^* is the reduced effective mass, κ is the dielectric constant, q is electron charge and $\hbar$ is the reduced Plank's constant [38]. However, it is usually better to fit the exciton binding energy experimentally. As mentioned earlier, the excitonic effect can only be seen at low temperatures and in very pure semiconductors. This is because at higher temperatures and for heavily doped or impurity rich semiconductors, free-carrier absorption mutes out the excitonic effect.

2.2.4 Free-carrier Absorption

A free carrier is an electron or hole free to move within its band. Free-carrier absorption happens when a free electron or hole is excited to even higher energy in the band. This kind of absorption requires a change in momentum provided by phonons or scattering from ionized impurities as well as the energy change provided by photon absorption [32]. A simple description of free-carrier absorption shows that the absorption coefficient of photon energy well beneath the band-edge is proportional to the concentration of free carriers and wavelength raised to the power of r where $1.5 < r < 3.5$ [32]. The power r correlates to relative contributions from optical phonons, acoustic phonons, and impurity scattering.

$$\alpha(\lambda) \propto \lambda^r n \quad or \qquad \alpha(\lambda) \propto \lambda^r p \tag{22}$$

The classical Drude-Zener free-carrier absorption coefficient can be calculated from [39]:

$$\alpha(\lambda) = \frac{\lambda^2 q^3}{4\pi^2 c^3 n^* \epsilon_o} \left[\frac{n}{m_n^2 \mu_n} + \frac{p}{m_p^2 \mu_p} \right] \tag{23}$$

where λ is the wavelength, q is the electron charge, c is the speed of light, n^* is the refractive index, ε_o is the permittivity of free space, n and p are the density of free electrons and holes respectively, m_n and m_p are the electron and hole effective masses, and μ_n and μ_p are the electron and hole mobilities. As shown by Schroder et al. the free-carrier absorption for silicon can be simplified and accurately described by the following equations for n-type and p-type silicon [39]:

$$\alpha_n(\lambda) = 2x10^{-18}\lambda^2 n \tag{24}$$

$$\alpha_p(\lambda) = 1.5x10^{-18}\lambda^2 p \tag{25}$$

where the total free-carrier absorption is a sum of the electron and hole contributions, λ is the wavelength in micrometers, and n and p are the carrier concentrations in cm^{-3}. A fit performed by Clugston et al. on data presented in Pankove's book shows that for n-type gallium arsenide the free-carrier absorption can be approximated by [40]:

$$\alpha_{FC}(\lambda) = 4x10^{-29}\lambda^3 n \tag{26}$$

where λ is the wavelength in nanometers and n is the carrier concentration in cm^{-3}. However, performing a similar fit, the constant was found to be closer to $7x10^{-29}$. At photon energies near and above the band-gap and especially for very pure semiconductors, free carrier absorption has very little effect on the measured absorption coefficient. For photon energies well beneath the band-gap, free-carrier absorption is the dominant absorption mechanism (see Figure 13). Following is a plot showing the effect of doping on the absorption coefficient in GaAs at near-infrared wavelengths.

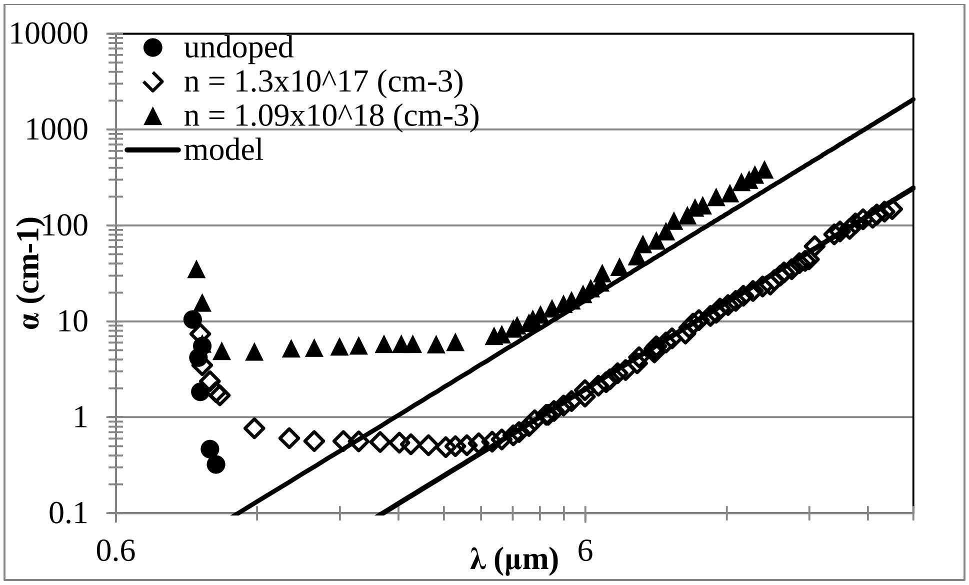

Figure 13: Absorption coefficient as a function of wavelength in GaAs under different carrier concentrations [41].

The λ^r dependence of absorption coefficient can be clearly seen at wavelengths of light where the energy is much less than the band-gap (λ>3μm). A plateau can be seen prior to the onset of observable free-carrier absorption. As this absorption phenomenon is below band-gap energies, it can be assumed to be a result of intra-band absorption (absorption from one band to another band of higher energy), or some other form of impurity band or hot-electron assisted absorption.

2.3 Near Band-Edge Absorption in GaAs and Si

Having discussed the basic physics describing and modeling the linear absorption of light in semiconductors including: fundamental direct and indirect band-gap absorption, Urbach tail absorption, excitonic absorption and free carrier absorption, following is the experimental setup, results and discussion of near band-edge absorption coefficient measurements and modeling performed in Si and GaAs. This study was performed to investigate and observe the capabilities of the Ekspla NT352A and is important as a foundation to the later study of non-linear absorption.

2.3.1 Experimental Setup

An Ekspla NT352A nanosecond pulsed, variable wavelength laser and a thermopile power meter were used to measure the transmission spectrum of Si and GaAs according to the experimental setup seen in in the following figure (see Figure 14).

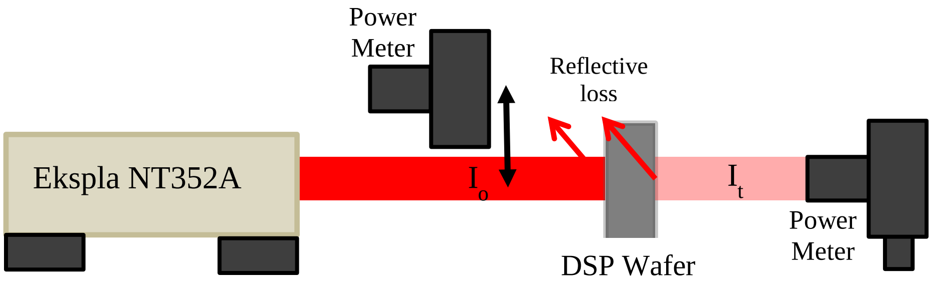

Figure 14: Experimental setup of transmission spectrum measurements.

The Ekspla NT352A was used to produce the incident laser beam from wavelengths of 667 nm to 2,600 nm normal to the surface of a double-side polished (DSP), single-crystal, lightly doped, silicon (Si) or gallium arsenide (GaAs) wafer. A thermopile sensor with 0.1 µW resolution was used to measure the incident and transmitted power by manually moving the sensor into the beam path in front of, then behind, the sample.

Absorption as a function of wavelength can be calculated from the transmission spectrum using eq. 6 such that:

$$\alpha(\lambda) = -\frac{1}{L}\ln\left(\frac{I_T}{I_o(1-R)^2}\right) \tag{27}$$

where I_o is the incident laser flux, I_T is the transmitted flux, R is the reflectivity calculated from eq. 7, and L is the thickness of the wafer. The $(1\text{-}R)^2$ term accounts for front and back surface reflection. Diffuse reflection and transmission are ignored because the incident beam is normal to the surface and both wafers are DSP meaning that surface scattering is low. In addition, the wavelength dependence of index of refraction n_2 for GaAs and Si is ignored because the wavelength range being studied is small enough that the slight index change has minimal effect on the calculated absorption coefficient.

2.3.2 Results and Discussion

The absorption coefficient spectrum for GaAs and Si were measured near the band-edge and compared to published data as well as modeled results using the band-edge absorption model, Urbach tail model, and exciton absorption model. It can be seen in Figure 15 that the measured absorption coefficient is close to previously published absorption coefficient measurements in GaAs by both Sturge [38] and Casey et al [42]. The Urbach tail is seen in GaAs beneath the band edge ($h\nu$<1.424 eV) and the resulting fit for the characteristic energy of the Urbach edge (E_o) was found to be 6.3 meV. This correlates well with Pankove's fits [35] showing E_o varying between 3 meV and 10 meV depending of carrier concentration.

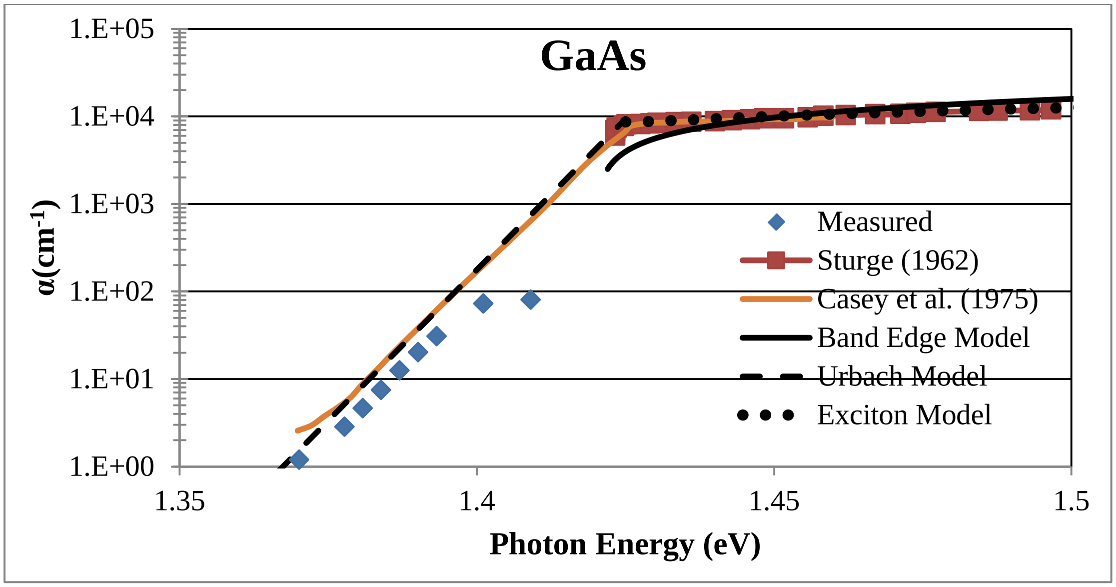

Figure 15: Measured absorption coefficient of GaAs compared to published and modeled data.

It can also be seen from Figure 15 that the band-edge model for absorption in direct band-gap semiconductors does not correlate as well as the exciton model for absorption at the band-edge with measured and published absorption. The band-edge model absorption coefficient (*A*) was found to be 5.6E4 cm^{-1} which correlates well with the calculated value of 3.04E4 cm^{-1}. When corrected for excitonic absorption, the model's deviation from data published by Casey et al. and Sturge was less than 5%. The exciton binding energy was found to be 2.5 meV which is exactly the same as the exciton binding energy (E_x) reported by Sturge [38] and is close to the calculated value of 3.7 meV at 295 K.

Following is a plot of measured absorption for Silicon including published [43] and modeled data. It can be seen that the published data correlates well with what was measured by the variable wavelength laser (see Figure 16).

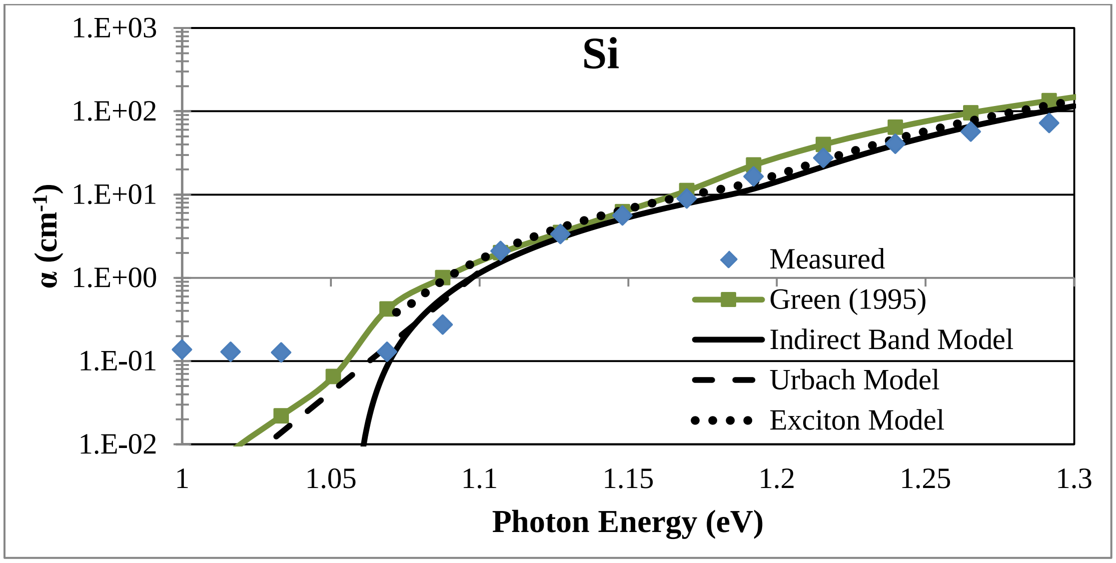

Figure 16: Measured absorption coefficient of Si compared to published and modeled data.

At photon energies less than 1.06 meV, the slight amount of power absorbed in the substrate was not detectable through transmission measurements and thus the lower limit of the measurement technique can be seen. As stated earlier, the system's limitation was due to power fluctuation of the incident beam and the resolution limit of the power meter preventing accurate transmission measurements and thus limiting the measureable absorption spectrum. The observable "hump" in absorption due to phonon absorption can be seen at $hv = E_g + E_p$ which occurs at about 1.18 eV. The best fit value for the phonon energy (E_p) was found to be 60 meV which correlates well with published results for the transverse optical phonon energy that dominates phonon assisted optical absorption (E_p=57.7 meV) [44]. In addition, the indirect-band absorption coefficient (A) was found to be 6.4E3 cm^{-1} which agreed well with the calculated value of 9.95E3 cm^{-1}. The fit for the characteristic energy of the Urbach edge (E_o) was found to be 15 meV and the absorption at the band-edge (α_g) was fit to be 4.5 cm^{-1}. This agrees very well with the measured and published absorption data. The binding energy for excitons (E_x) in silicon is 14.7 meV according to Kittel [45] which agrees well with the best fit value of 10 meV and the Rydberg energy calculation of 2.9 meV. It can also be seen in Figure 16 that the exciton model correction agrees better with Green's absorption data than the measured data. This is most likely due to inaccuracy in absorption coefficient measurement in the high transmission region.

The resolution and precision of the incident and transmitted beam flux measurements made by the thermopile sensor were the limiting components to obtaining broader photon energy spectrum absorption coefficient curves. Because of power fluctuation in the incident beam as well as the measurement error inherent to the thermopile sensor, transmission had to be between 0.07-47 % for both GaAs and Si. For transmission below or above these values, the change in incident to transmitted power is too small to accurately measure I_T/I_o and thus $\alpha(hv)$. Following is a table summarizing the parameters used to describe the absorption coefficient curves including published, calculated and best-fit values (see Table 1).

Table 1: Summary of parameters used to fit band-edge absorption model, Urbach model, and exciton model for absorption coefficient calculations

	Fundamental Absorption						**Urbach Model**		**Exciton Model**
Material	E_g	T	L	n_2	A	E_p	E_o	α_g	E_x
	(eV)	***(K)***	***(cm)***		(cm^{-1})	***(eV)***	***(eV)***	(cm^{-1})	***(eV)***
Si	1.12	300	0.035	3.67	6400*	0.06	0.015	4.5	0.001**
GaAs	1.42	300	0.04	3.7	56000*		0.0063	8000 [35]	0.0025**

*calc. = 9950, 30400 **calc. = 0.0029, 0.0037

The calculated values for A and E_x are from equation 9 and 21 respectively and are included at the bottom of the table for comparison. The purpose of this study was to understand and observe the basic photon absorption processes in semiconductors at the band-edge as well as establish the usability of the Ekspla NT352A variable-wavelength nanosecond laser source as a feasible instrument to measure absorption. Ultimately, it was found that the normal-laser transmission method of absorption measurements is only accurate at measuring absorption for photon energies near the band-gap of the material. If wafer thickness was controlled, by a thinning process for example, the absorption measurements could be accurate for a broader spectrum of light energy. Thinner substrates would allow for more accurate measurements of higher energy photons, and thicker substrates would enable lower energy photon absorption coefficients to be measured.

This experiment was successful in showing the characteristic shapes of absorption near the band-edge in silicon and gallium arsenide. Phonon emission and absorption assisted band-to-band transitions in indirect band-gap semiconductors were distinguishable in silicon, but the direct band-gap absorption edge was not observable in GaAs due to measurement limitations discussed earlier. The sub band-gap absorption mechanisms of excitonic absorption as well as the characteristic Urbach tail were observable in both materials. Because this research involves high fluence laser light focused into a bulk crystal, the linear absorption properties presented earlier do not present a full picture of all important light-material interactions. At high fluence, the interaction of light and material becomes intensity dependent, and the properties are thus called non-linear.

2.4 Nonlinear Optical Processes

The non-linear optical properties of semiconductors and wide band-gap dielectrics are crucial to the understanding of light-material interactions at high light intensity and thus high electro-magnetic field. Since the invention of the laser, it was quickly observed that traditional linear optics failed to describe some of the observations made when material is exposed to high intensity light. The first example of an observed nonlinear optical property, termed second harmonic generation, occurred shortly after the first successful instance of laser light emission in 1960. SiO_2 was used as a harmonic crystal for a ruby laser (694 nm) to produce second harmonic wavelength light (347 nm) [46]. Since the onset of widely available laser systems that can deposit enormous amounts of energy in a small area (>GW/cm^2), nonlinear optics has become an increasingly important area of science both to the development of novel laser systems, and the understanding of material physics. Most simply put, nonlinear optics is "the study of phenomena that occur as a consequence of the modification of the optical properties of a material system by the presence of light" [47].

When discussing nonlinear optics, most text books begin with a description of the defining equation for nonlinear polarization related to optical susceptibility, so that is where we will begin. For an instantaneous dielectric response in an isotropic material, the complete time-dependent polarization can be written as the power series [47]:

$$\bar{P}(t) = \epsilon_o[\chi^{(1)}\bar{E}(t) + \chi^{(2)}\bar{E}^2(t) + \chi^{(3)}\bar{E}^3(t) \dots] \qquad (28)$$

where $\chi^{(2)}$, and $\chi^{(3)}$ are the second-, and third-order nonlinear susceptibilities, and the first-order tensor $\chi^{(1)}$ is the linear susceptibility. $\bar{E}(t)$ is the scalar electric field strength as a function of instantaneous time *t*. Usually the polarization is expressed as a function of radial frequency, but because the assumption was made for instantaneous response, it is a constant implied by the Kramers-Kronig relation [48]. This relation also means that the tensors have a real and imaginary portion. The linear index of refraction and absorption coefficient are dependent on the real and imaginary parts (respectively) of the linear susceptibility tensor $\chi^{(1)}$ such that index of refraction in SI units as a function of radial frequency is given by [48]:

$$n_o(\omega) = \sqrt{1 + \chi^{(1)}_{real}(\omega)} \tag{29}$$

And the linear absorption can be described as [48]:

$$\alpha_o(\omega) = \frac{\omega\, \chi^{(1)}_{imag}(\omega)}{n(\omega)\, c} \tag{30}$$

where c is the speed of light in vacuum and ω is the radial frequency of the light.

The second-order nonlinear susceptibility $\chi^{(2)}$ governs optical processes such as the electrooptic Pockels effect, frequency conversion like second harmonic generation, and quasi-polarization through optical rectification. Frequency conversion happens from induced dipole moments as a result of incident optical waves at high intensity. The induced dipoles are in phase related to the incident radiation and the crystal geometry. The phased array of dipoles then radiate a new coherent wave, and this process is termed harmonic generation [47]. Harmonic generation is important to this project only in that it describes the optical parametric oscillation (OPO) process distinctive of the NT352A laser tool. The second-order nonlinearity is effectively zero in centrosymmetric materials meaning that materials like silicon cannot be readily used to achieve harmonic generation [49]. The phase of the incident light and the crystal symmetry of the optical material are very important to the processes governed by second-order susceptibility, however, second-order effects are largely out of the scope of this work. On the other hand, the nonlinear index of refraction and nonlinear absorption described by the third-order tensor are very important to this research in that they govern the propagation of light at high irradiance. The third-order nonlinear susceptibility $\chi^{(3)}$ defines the nonlinear refractive index, and thus the nonlinear absorption properties of a material.

2.4.1 Nonlinear Refractive Index

The non-linear refractive index, also referred to as the optical Kerr Effect, is related to the third-order contribution to polarization and thus the third-order susceptibility. The total (nonlinear and linear) refractive index defined by first- and third-order polarization can be written as [47]:

$$n = n_o + n_2 I - i\frac{\lambda}{4\pi}(\alpha_o + \alpha_2 I) \tag{31}$$

where n_o is the linear refractive index, I is the intensity of the incident wave in units of W/m^2, α_o is the linear absorption, α_2 is the nonlinear two-photon absorption (which will be discussed in the following section), and n_2 is the nonlinear refractive index in units of m^2/W. The nonlinear refractive index n_2 is related to the real part of third-order nonlinear susceptibility by [47]:

$$n_2 = \frac{3}{4n_o^2\epsilon_o c}\chi_{real}^{(3)} \tag{32}$$

where ϵ_o is the dielectric permittivity and c is the speed of light. Because n_2 is on the order of 10^{-10} to 10^{-20} (cm^2/W) in most materials, the nonlinear index of refraction has little contribution to the overall index at low light intensity. However, at the high intensities achievable with lasers, it can have a very large contribution and ultimately cause a phenomena called self-focusing.

Self-focusing is the result of an intensity dependent change in refractive index n that is due to a positive nonlinear refractive index n_2. The index of refraction changes as a function of intensity causing the beam to focus in on itself. If the proper balance is established between the intensity of the incident beam and the nonlinear refractive index of the material, self-trapping can occur. Self-trapping causes the beam to propagate through the medium without a change in beam width. Both self-focusing and self-trapping are schematically compared to the focus of a beam that does not take into account the nonlinear change in refractive index (see Figure 17). The critical beam power for self-trapping is [47]:

$$P_{cr} = \frac{\pi(0.61)^2\lambda_o^2}{8n_o n_2} \tag{33}$$

where λ_o is the laser wavelength, and the coefficient 0.61 varies slightly for different beam shapes and numerical assumptions. If the incident beam power is greater than the critical power, self-focusing occurs. If the incident power equals the critical power, self-trapping can occur [50]. Note that for pulsed lasers, the peak power of the incident beam must be related to the critical power for self-trapping, not the average power.

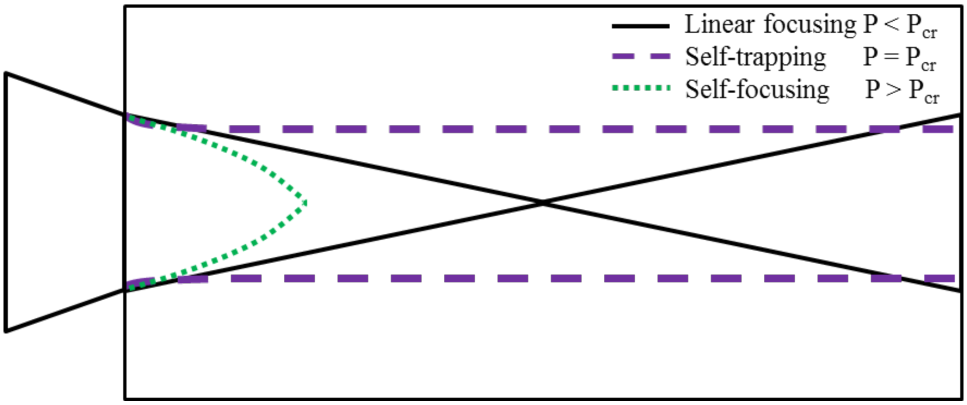

Figure 17: Schematic of self-trapping, self-focusing, and beam focus ignoring nonlinear effects.

For a 5 mJ energy per pulse beam at 6 ns pulse width, which is normal operation values of the NT352A laser, the peak power of 0.83 MW is less than the critical power for self-trapping in sapphire: P_{cr} = 1.23 MW for $n_o = 1.75$, n_2 = 3E-16 cm^2/W [51], and λ_o = 667 nm. However, for silicon, P_{cr} = 22 kW at λ_o = 1.55 µm, $n_o = 3.5$, and n_2 = 4.5E-14 cm^2/W [52]. Thus to avoid self-focusing in silicon, much lower peak power must be used. If the incident power is below that required for self-focusing, the focused beam shape can be accurately described by normal ray-optics methods. The power limits to avoid self-focusing will become important in Chapter 3 where the propagation of a Gaussian beam focused into an optical material is discussed further.

2.4.2 Nonlinear Absorption: Two Photon

Nonlinear absorption refers to the intensity dependence of transmittance in a material specifically due to the increased probability of absorbing more than one photon at a time at high intensity [48]. Thus far, absorption has been treated as a one-photon process referred to as fundamental absorption: the process where a photon is absorbed by a valence electron and that electron is ultimately raised to the energy level of the conduction band. This energy promotion results in a free-to-move electron in the conduction band and hole in the valence band. For photons of energy less than the energy of the band-gap, other processes must govern photoionization and thus absorption. As discussed earlier, transitions of electrons to the conduction band from a photon of sub band-gap energy can happen independent of intensity; some of the linear mechanisms are: free carrier absorption, defect assisted absorption, phonon assisted absorption, intraband absorption, Urbach tail absorption, excitonic absorption…etc. However, at laser achievable intensities (>kW/cm^2), the nonlinear absorption processes become important. As mentioned earlier, the third-order nonlinear susceptibility governs refraction. Consistent with the Kramers-Kronig relationship of linear refraction and absorption, the non-linear absorption, for two-photon absorption, is related to the imaginary portion of the third-order nonlinear susceptibility by [53]:

$$\alpha_2 = \frac{3\omega}{2c^2 n_o^2 \epsilon_o} \chi_{Imag}^{(3)} \tag{34}$$

where ω is the radial frequency of the light, n_o is the linear refractive index, ϵ_o is the dielectric permittivity, and c is the speed of light. Two-photon absorption is a multiphoton process where two photons of energy ($hv < E_g$) possess enough collective energy to raise an electron to the conduction band (see Figure 18). For wider band-gap semiconductors or photons of low energy, higher order (number of photons, $n > 2$) absorption processes happen.

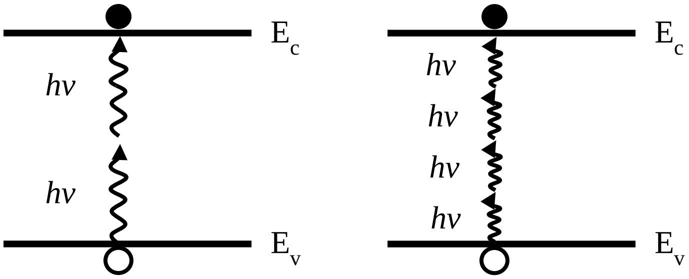

Figure 18: Two-photon absorption and multiphoton (n = 4) absorption processes.

From second-order perturbation theory and for direct band semiconductors, the two-photon absorption coefficient for two photons of the same energy can be calculated as [54]:

$$\alpha_2(\omega) = K \frac{\sqrt{E_k}}{n_o^2 E_g^3} \; F_2\left(\frac{\hbar\omega}{E_g}\right) \tag{35}$$

where the function $F_2\left(\frac{\hbar\omega}{E_g}\right)$ reflects the band structure assumptions, E_k is the Kane momentum parameter which is about 21 eV for most materials, and K is a material-independent constant:

$$K = \frac{2^9\pi}{5}\frac{e^4}{\sqrt{m_o}c^2} \tag{36}$$

where e is the charge of an electron and m_o is the mass of an electron. $K = 1940$ in units such that α_2 is in units of cm/GW and E_g and E_k are in eV [54]. For an indirect band-gap material like silicon, calculation of the two-photon absorption coefficient becomes much more complicated because of the requirement of phonon assistance to reach the indirect conduction band. Direct band-gap assumptions can be made that approximate the two-photon absorption coefficient with dressing factors, but this is out of the scope of this work. If more information about indirect two-photon absorption is desired, refer to Garcia and Kalyanaraman's work [55] or some of Yee's original work on third-order perturbation theory of phonon assisted two-photon absorption in indirect band-gap semiconductors [56, 57]. Because the two-photon absorption coefficients at a variety of laser parameters for many materials have been measured and validated by multiple groups [58, 52], we do not need to utilize any theoretical two-photon absorption approach to calculate photoionization rates and carrier concentration in Si. In addition, the two-photon effects in silicon are often drowned out by free-carrier absorption at higher pulse lengths (>10ps) [59]. Calculating photoionization rates and light induced carrier concentrations ultimately becomes very important to describing the laser induced breakdown of materials, which is the crux of this work. Unlike two-photon absorption in silicon, multiphoton absorption in sapphire most likely needs to be calculated to model photoionization and laser damage. This is because higher order photon absorption coefficients (number of photons >3) required to photoionize sapphire at low wavelengths are very difficult to measure and have not been accurately reported on.

2.4.3 Nonlinear Absorption: Multiple Photon

Presently the most accurate and comprehensive model showing the photoionization rate, and thus the nonlinear absorption coefficient and electron concentration of material in a high intensity laser field is the Keldysh photoionization model. Originally, photoionization was described by classical perturbation theory, and it explained the relationship between band structures and photon absorption in materials. However solving for multiple photon absorption becomes very difficult when a high number of photons are required to raise an electron to the conduction band with energy conservation. As the number of photons required for transitions increases, the perturbation-order required to solve photon material interactions similarly increases. This results in extreme calculation difficulty at multiphoton processes involving 4 or greater photons [60]. Instead Keldysh theorized that the light-material interaction can be treated as if a lattice Hamiltonian were in the presence of a very quickly oscillating electric field Hamiltonian representing the laser light. The treatment of induced electric field in the material from light in this way causes a low-field limit defined by multiphoton photoionization, and high-field limit defined by tunneling. This can be shown using the Keldysh adiabatic parameter [61, 62]:

$$\gamma = \frac{\omega\sqrt{m_r E_g}}{eE} = \frac{\omega}{e}\left[\frac{m_r c n \varepsilon_o E_g}{I}\right]^{1/2} \qquad (37)$$

where e is the charge of an electron, ω is the radial frequency of the light, m_r is the reduced electron-hole mass, E_g is the band-gap of the material, and E is the electric field, c is the speed of light, I is the intensity, n is the refractive index, and ε_o is the permittivity of free space. When $\gamma \gg 1$, multiphoton photoionization dominants the rate equation, and when $\gamma \ll 1$, tunneling photoionization dominates [61]. Figure 19 shows an illustration of the crystal potential of an atom and the dominant ionization method as it relates to the Keldysh adiabatic parameter.

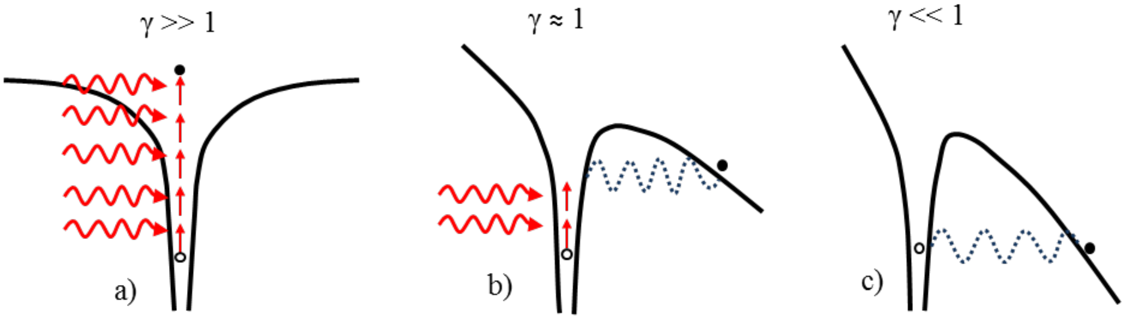

Figure 19: Crystal potential of an atom in a) very low external field showing multiphoton photoionization, b) low external field showing a combination of multiphoton and tunneling ionization, and c) high external field showing just tunneling ionization [62].

From Keldysh theory, the photoionization rate can be calculated as [50]:

$$W_{PI} = 2 \cdot \frac{2\omega}{9\pi} \cdot \left(\frac{\sqrt{1+\gamma^2}}{\gamma} \cdot \frac{m\omega}{\hbar} \right)^{3/2} \cdot Q_k(\gamma, x) \cdot exp\left[-\pi \langle x+1 \rangle \cdot \frac{K(\gamma_1) - E(\gamma_1)}{E(\gamma_2)} \right] \tag{38}$$

where the slowly varying function Q_k is [63]:

$$Q_K(\gamma, x) = \sqrt{\frac{\pi}{2K(\gamma_2)}} \cdot \sum_{n=0}^{\infty} \left\{ exp\left[-n\pi \frac{K(\gamma_2) - E(\gamma_2)}{E(\gamma_1)} \right] \Phi \left[\pi \sqrt{\frac{(2\langle x+1 \rangle - 2x + n)}{2K(\gamma_2)E(\gamma_2)}} \right] \right\} \tag{39}$$

The function x is the laser-modified band gap or effective band gap:

$$x = \frac{2}{\pi}\frac{E_g}{\hbar\omega}\frac{\sqrt{1+\gamma^2}}{\gamma}E\left(\frac{1}{1+\gamma^2}\right) \tag{40}$$

where E_g is the band gap in eV, m is the reduced electron-hole mass, $\hbar$ is the reduced Plank's constant, K and E are complete elliptic integrals of the first and second kind respectively, the symbol $\langle x \rangle$ denotes the integer part of x, and $\Phi(x)$ is the Dawson function where:

$$\Phi(x) = \exp(-x^2)\int_0^x \exp(y^2)\,dy \tag{41}$$

Although not trivial, the Keldysh theory has been solved for multiple material systems in its completeness to calculate the photoionization rate at various electric field strengths and laser parameters [63, 64, 65, 66, 60]. The Keldysh theory has also been used to accurately predict the value of two-photon absorption coefficient as well as the laser-induced-damage-threshold in many wide band-gap materials [62, 66]. In Figure 20, the photoionization rate as a function of electric field can be seen for fused silica irradiated by an 800 nm wavelength laser.

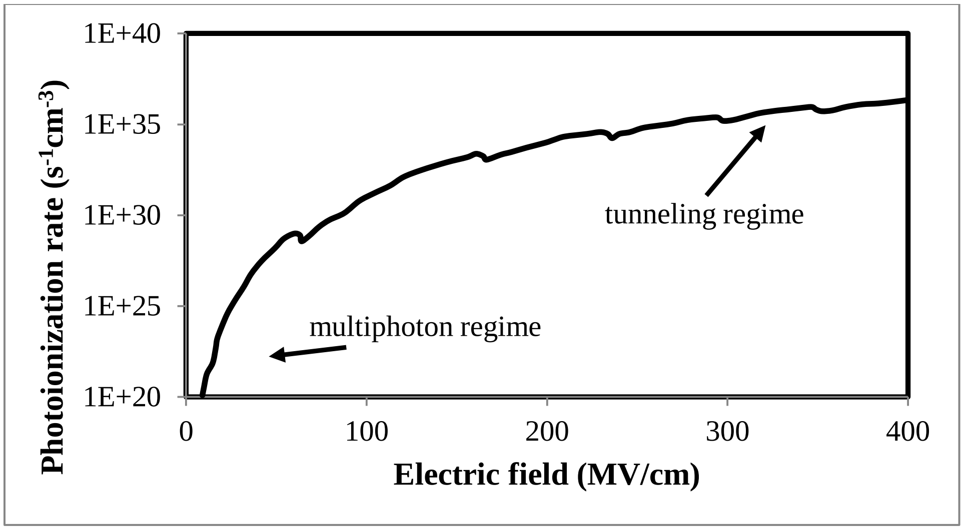

Figure 20: Keldysh photoionization rate for fused silica (E_g = 9 eV) at 800 nm wavelength [64].

As stated earlier, at low electric field the photoionization rate is determined by multiphoton absorption, and at high field strength tunneling dominates. Figure 21 shows the relationship between wavelength and photoionization rate of NaCl for various laser intensities using the Keldysh theory.

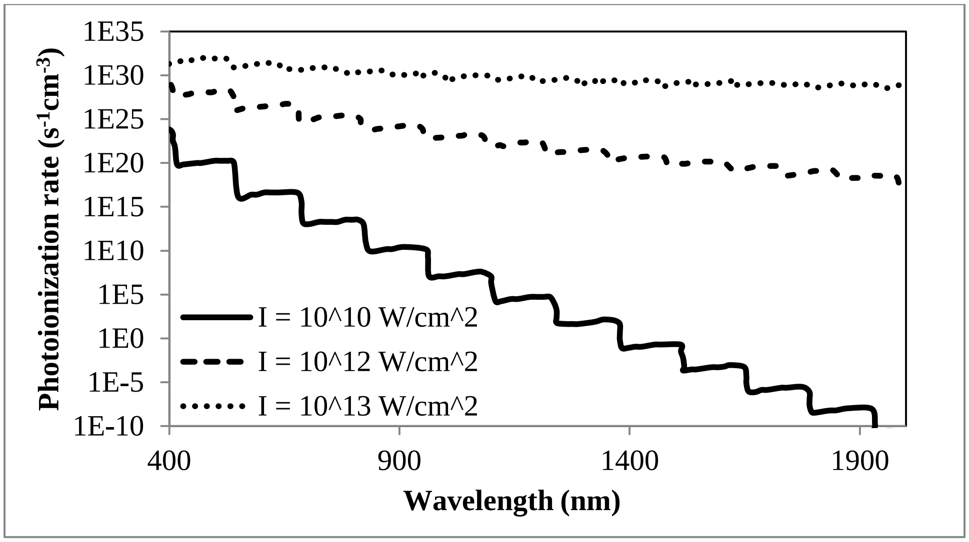

Figure 21: Keldysh photoionization rate for NaCl (E_g = 8.97 eV) for various wavelengths and laser intensity [50].

At high intensity ($I > 10^{13}$ W/cm^2), the wavelength dependence of photoionization becomes negligible. This is because the majority of free-carriers are generated from tunneling as opposed to multiphoton absorption. The calculation of photoionization rate will ultimately aid in the modeling of damage induced in the bulk of semiconductors and wide band-gap dielectrics from high intensity laser irradiation which will be further discussed in the next section.

2.5 Laser Induced Damage

As mentioned earlier, high intensity laser light is often used as a non-contact method to machine materials. Because light occupies no volume, huge amounts of energy can be focused into very small areas achieving intensities large enough to permanently change the structure of a material through melting or ablation (direct vaporization). In pulsed laser systems, because the peak power (energy per pulse / pulse length) can easily reach terawatt magnitude, permanent lattice modification can occur on an incredibly fast time scale (<100fs). In order to begin to understand the laser induced damage mechanisms, the light-material interaction governing the deposition of light energy into a material (absorption) was presented for linear transitions (Section 2.2) and nonlinear transitions (Section 2.4). Below is a flow chart detailing the basic processes and mechanisms of laser interaction with a semiconducting or wide band-gap crystalline dielectric material resulting in laser induced damage (see Figure 22).

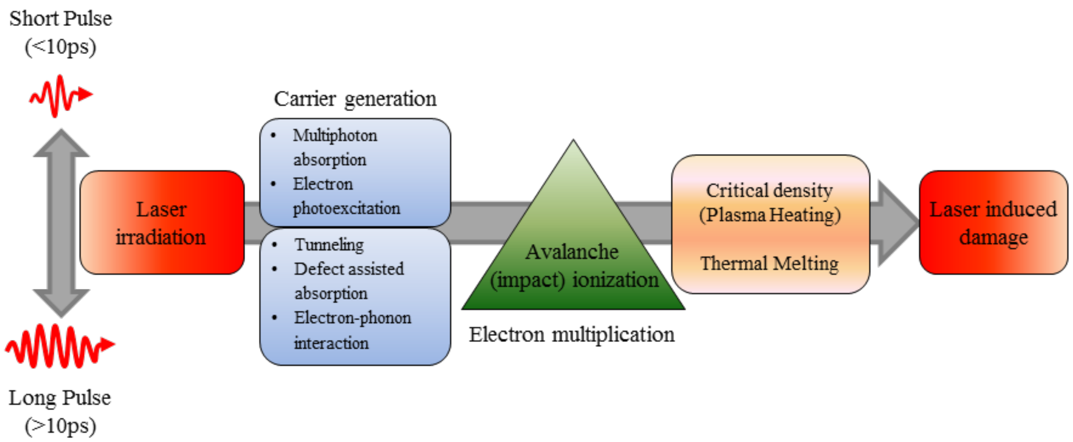

Figure 22: Laser induced damage process for short and long pulse length lasers [67].

For both short and long pulse-length lasers, the breakdown process begins with the absorption of light to generate free-carriers. When enough free-carriers exist in close proximity, avalanche can occur if the laser beam length is sufficiently long enough (greater than a few fs). Then the critical density of free electrons is reached, and an electron-plasma is formed that is extremely strongly reflecting [68]. If the pulse length is longer than a few picoseconds, electron energy can be transferred to the lattice and thermal melting can contribute to the damage process [69]. For very long pulses (longer than 100 ns) the damage mechanism is dominantly thermal. The critical density for plasma formation can be calculated from [70]:

$$N_{crit} = \frac{\omega^2 m \epsilon_o}{e^2} \tag{42}$$

where ω is the laser radial frequency, m is the mass of an electron, ϵ_o is the permittivity of free space, and e is the charge of an electron. It can be seen that the critical density form this calculation is largely material independent, and is about 1e20-1e21 cm^{-3} for near-IR laser light. For short pulses, after the kinetic energy of the electron-plasma is transferred to the lattice through phonon interaction, permanent lattice modification results. For very short pulses (<10 fs), the critical density can be reached before avalanche can take place [71, 72]. For short pulse-length lasers at low intensity in a wide band-gap material, carrier generation is dominated by multiphoton absorption according to the Keldysh adiabatic parameter in equation 37. For high intensity long pulses, tunneling dominates and avalanche ionization is seeded by free-carriers resulting from easily ionizable defect levels and tunneling. In addition, long enough pulses (>100 ps) allow for electron-phonon interactions thus adding another element of complexity to the description of light absorption. For extremely short laser pulses (<100 fs), laser induced damage has often been described by the photoionization rate from multiphoton absorption and tunneling where recombination can be ignored. But for longer pulses, the generation of carriers, onset of avalanche, phonon interaction, and achievement of critical carrier density for melting becomes a more complicated problem that might need to include thermal effects.

There is a $\tau^{1/2}$ correlation of damage threshold with pulse width for pulses longer than 20 ps as observed by Stuart et al. for a 1053 nm wavelength laser (see Figure 23). This is consistent with data found by other groups for sub picosecond ablation of wide band-gap dielectrics [73, 71, 63].

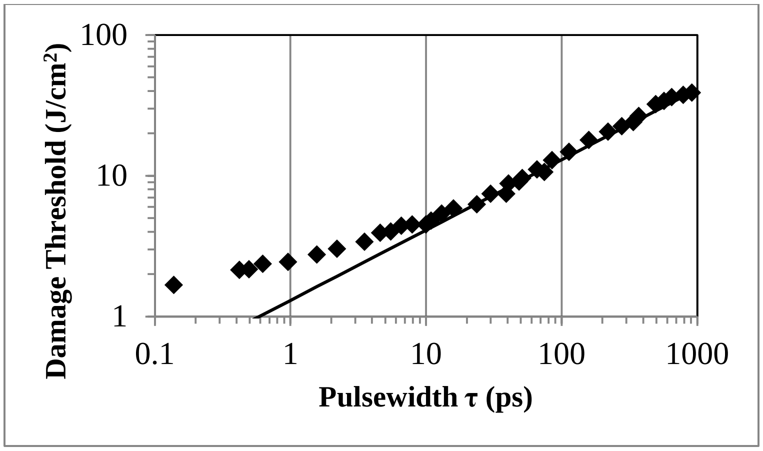

Figure 23: Laser induced damage threshold as a function of pulse width in fused silica [72].

A long enough pulse allows for electron energy to be transferred to the lattice while the material is still being irradiated by the laser. This results in a damage threshold that is also dependent on phonon assistance and the thermal properties of a material. Thus, thermal diffusion and lattice heating are important to the modeling of laser induced damage mechanisms for sufficiently long pulses [72].

2.5.1 Beam Propagation and Carrier Generation in Silicon

In silicon, it has been shown that near-IR absorption of laser light can be modeled by the intensity of the propagating laser beam as a function of radial and z-position from the following equation [59]:

$$\frac{dI(r,z)}{dz} = -\alpha I(r,z) - \alpha_2 I^2(r,z) - \sigma_{ex} N I(r,z) \qquad (43)$$

where *I(r,z)* is the irradiance as a function of r- and z- position, α is the linear absorption coefficient, α_2 is the two-photon absorption coefficient, σ_{ex} is the absorptivity of laser-generated free carriers, and *N* is the density of free carriers. Carrier density is determined by [74]:

$$\frac{dN(r,z)}{dt} = \frac{\alpha I(r,z)}{\hbar\omega} + \frac{\alpha_2 I^2(r,z)}{2\hbar\omega} \tag{44}$$

where $\hbar\omega$ is the photon energy. This model ignores carrier diffusion and recombination because for short pulses, the carrier lifetime can be much larger than the pulse length and the diffusion length during the pulse is negligible. Other groups have performed similar calculations on beam propagation and carrier generation including temperature effects, diffusion, and recombination [69].

According to Boggess et al., for pulse lengths longer than 8 ps of photon energy near the band edge in silicon (λ ≈ 1 µm), the two-photon absorption (TPA) coefficient can be negligible in modeling the transmission of laser radiation [59]. This would mean that the nonlinear absorption of photons is dominated by free carrier absorption (FCA) and/or linear absorption (LA). However when short pulse lasers are used (pulse length < 50 ps), TPA becomes important to the modeling of nonlinear absorption and its effects on transmission. Following is the experimental results of Boggess et al. showing transmission as a function of laser fluence compared to fitted modeling results.

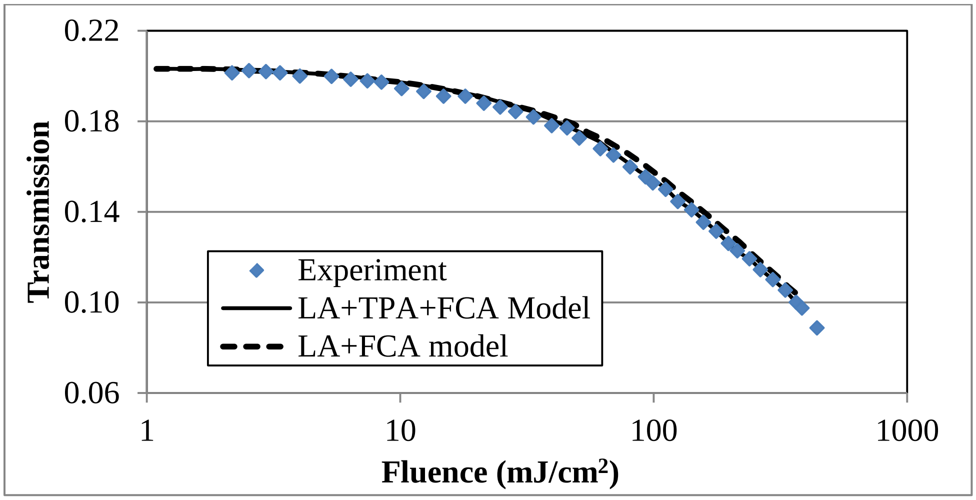

Figure 24: Transmission as a function of fluence for pulse width is 69 ps, wavelength is 1.064 µm, on a wafer of silicon that is 1.2 mm thick [59].

It can be seen from Figure 24 that for 69 ps laser pulses at 1.064 μm wavelength, two-photon absorption is not hugely significant to the transmission measurement. However, this nonlinear absorption method was used to measure two-photon absorption coefficients (α_2) in silicon as well as linear absorption (α) and free-carrier absorption (σ_{ex}) coefficients. By measuring the nonlinear transmission, and fitting for free-carrier and linear absorption, the two-photon absorption coefficient can be calculated. The results for FCA, TPA, and LA absorption coefficients calculated form the nonlinear transmission measurements in the picosecond regime for near-IR wavelength proved to be close to those measured by other groups and other techniques [59].

2.5.2 Beam Propagation and Carrier Generation in Sapphire

In wide band-gap crystalline materials where the free carrier concentration at room temperature is low, the carrier generation process is largely a result of multiphoton photoionization, tunnel photoionization, and avalanche ionization [72]. The general equation describing the carrier density is [64]:

$$\frac{dN}{dt} = W_{PI} + n_{ava}(I)N \tag{45}$$

where $W_{PI}$is the Keldysh photoionization rate from eq. 38, I is the laser intensity, and n_{ava} is the avalanche ionization rate which will be discussed further in the following chapter. This equation can be modified to include the availability of bound electrons in the valance band as well as recombination [64]:

$$\frac{dN}{dt} = (W_{PI} + n_{ava}(I)N)\left(1 - \frac{N}{N_{max}}\right) - \frac{N}{\tau_s} \tag{46}$$

where N_{max} is the maximum valence electron density, and τ_s is the electron trapping time.

Calculating the rate of free carrier generation as it correlates to incident beam intensity has historically allowed for the accurate prediction of the laser induced damage threshold in many wide band-gap materials as well as the beam propagation factors like transmission and reflectance at high intensity [72, 63, 64, 75, 76, 68]. The damage threshold for fused silica at various pulse widths can be seen in Figure 25.

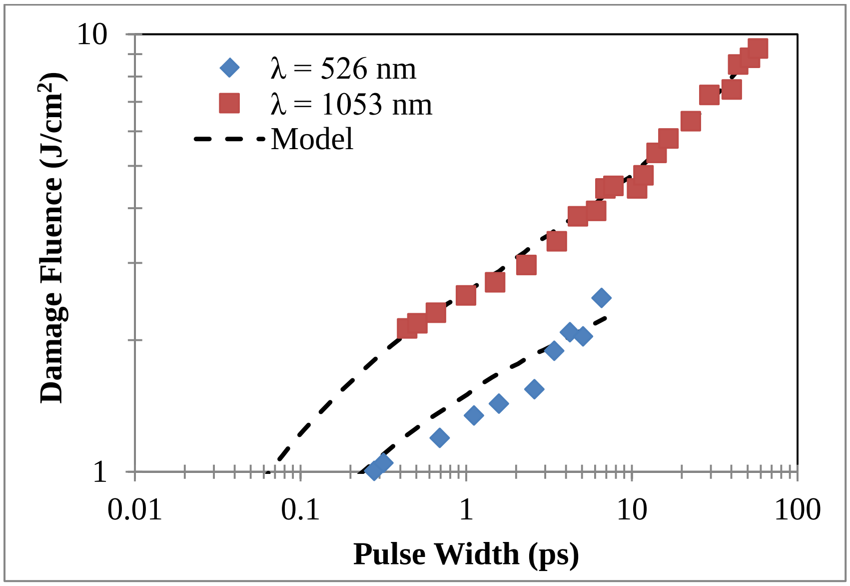

Figure 25: Measured and calculated threshold fluence for fused silica at 1053 nm and 526 nm wavelengths [72].

Stuart's model includes avalanche and photoionization terms calculated from Keldysh theory. It can be clearly seen that the model predicts damage threshold well for extremely short laser pulse widths. Accurate prediction of laser induced damage threshold will become important in the following chapter.

Chapter 3

SUBSURFACE LASER MODIFICATION MODEL

This chapter presents the evolution of the modeling process from a basic optical model used to describe laser fluence throughout the beam path and focal volume, towards a more comprehensive model detailing the light absorption process and spatial carrier concentration in time. The optical model uses Snell's law and basic ray-optics to describe the path of focused light through two mediums of different indices of refraction. The more thorough modeling effort will be deemed the "electron-plasma model" as the threshold for subsurface damage will be determined by carrier concentration and the electron-plasma absorption discussed in Chapter 2. The combination of both models to describe the propagation and absorption of light in the bulk of a semiconducting or insulating crystalline material is the crux of this work.

Both models are adapted for silicon material properties and sapphire. The modeling of bulk laser damage formation in silicon and sapphire is not novel [77, 78], however to the best understanding of this author, this is the first instance of modeling using the full Keldysh theory combined with ray-optics beam shaping to accurately describe and predict damage geometry in sapphire at nanosecond pulse lengths. In addition, the following model was used to better understand why damage contained in the bulk of silicon is much more difficult to generate.

3.1 Ray-Optics Model

The first modeling approach taken to describe and predict subsurface damage formation in the bulk of a transparent material was a ray-optics approach. By simply following the path of light, in a particle frame-of-mind, through air and focused at high numerical aperture in the bulk of a material, the fluence at and around the focal volume at the Gaussian peak pulse energy could be calculated. This was then compared to published surface ablation damage thresholds for similar wavelengths, pulse widths and materials and used to estimate the damage volume in the bulk of the material. The simple ray-optics approach limited by published laser induced damage thresholds was found to be roughly accurate in predicting the damage shape in bulk sapphire, and helped to understand some difficulties in controlling laser damage formation in bulk silicon.

3.1.1 Subsurface Focus Gaussian Laser Beam Model

Following is a description of the ray-optics model that was used to describe the beam propagating through air and focused beneath the surface of a material to show the beam intensity or spatial fluence at and around the focal point. The beam was assumed to be Gaussian TM_{oo} and the Gaussian spot radius or beam waist at the focal point could be approximated by [79]:

$$w_o = \frac{2\lambda f}{\pi D n_1} \tag{47}$$

where λ is the laser wavelength, f is the focal length of the focusing optic, D is the diameter of the beam at the optic and $n_1$is the refractive index of air as seen in Figure 26.

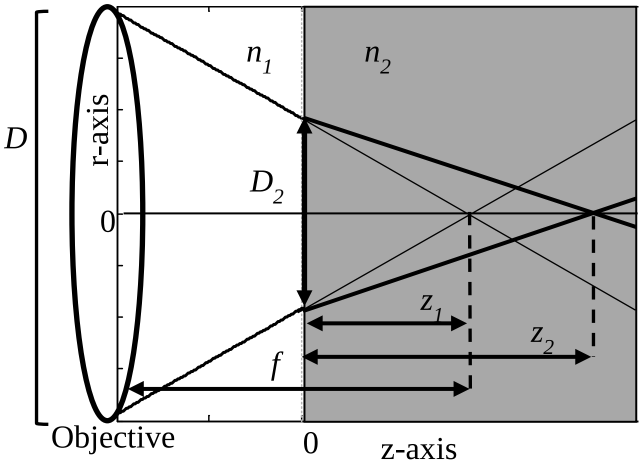

Figure 26: Diagram of subsurface focus model parameters.

The Rayleigh Range can then be calculated for the beam if it were focused into air or sapphire:

$$Z_{R,air} = \frac{\pi w_o^2}{\lambda} \tag{48}$$

$$Z_{R,sapphire} = n_2 Z_{R,air} \tag{49}$$

where n_2 is the real part of the index of refraction of sapphire assumed to be 1.77 at λ=667nm [80] . From Snell's law, it can be found that the focus depth into sapphire is:

$$z_2 = \frac{n_2}{n_1} z_1 \sqrt{1 + \frac{n_2^2 - n_1^2}{n_2^2} \left(\frac{D_2}{2z_1}\right)^2} \tag{50}$$

where z_1 is the focal depth in air and D_2 is the beam diameter at the interface of sapphire and air. If $D_2 \ll z_1$, then the focal depth into the material can be approximated as $z_2 \approx n_2 z_1$ and the focused spot size in the sapphire remains the same as in the material [81]. The beam radius as a function of *z*-position is:

For $z \leq 0$, or in air:

$$w(z) = w_o \sqrt{1 + \left(\frac{z - z_1}{Z_{R,air}}\right)^2} \tag{51}$$

For $z > 0$, or in sapphire:

$$w(z) = w_o \sqrt{1 + \left(\frac{z - z_2}{Z_{R,sapphire}}\right)^2} \tag{52}$$

And the irradiance as a function of radius and *z*-position is [82]:

$$I(r, z) = (1 - R)I_o \left(\frac{w_o}{w(z)}\right)^2 exp\left(\frac{-2r^2}{w(z)^2}\right) \tag{53}$$

where R is the reflectivity, $I_o = I(0,0)$ or the max intensity at the beam waist and can be calculated for a circularly symmetric beam as:

$$I_o = \frac{2P}{\pi w_o^2} \tag{54}$$

where *P* is the average incident beam power [82]. Following are the modeling results of the basic ray-optics equations for light focused in a medium of index of refraction of 1.77 (sapphire [83]) or 3.44 (silicon [84]) at different average beam powers (see Figure 27).

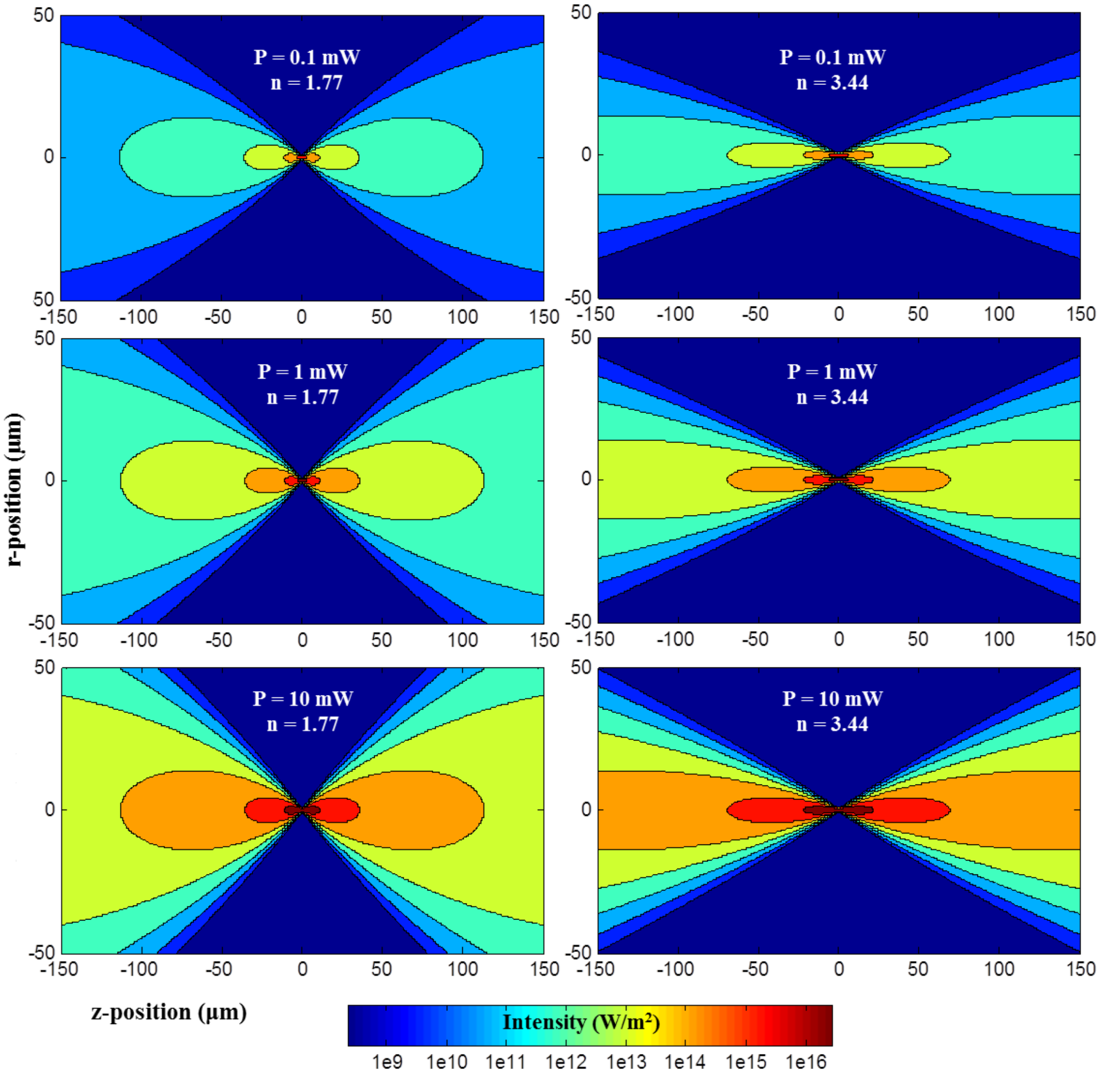

Figure 27: Ray-optics model results of beam intensity for focusing optic NA = 0.50 in sapphire and silicon at various average beam powers.

It can be seen that the higher index of refraction of silicon causes the light to focus in a longer beam waist and results in a larger Gaussian spot size and larger Raleigh range using the same numerical aperture optics. A lower index material like crystalline sapphire allows for tighter focus and smaller spot sizes.

The peak laser intensity (W/m^2) threshold for damaging a material can be calculated from the fluence threshold (J/cm^2) using the following equation:

$$I\left(\frac{W}{m^2}\right) = 1e13 * \left(\frac{F(\frac{J}{cm^2})}{t\ (ns)}\right) \tag{55}$$

where F is the laser damage threshold in J/cm^2 and t is the pulse width of the beam in nanoseconds. From published damage thresholds for comparable pulse length lasers the peak laser intensity threshold before permanent material breakdown occurs can be estimated. These values are 3.5E14 W/m^2 in sapphire (210 J/cm^2 [85]) and 8E12 W/m^2 in silicon (5 J/cm^2 [86]) for a nanosecond pulse width laser. From these thresholds, the region of permanent damage could be roughly estimated.

However, because no absorption term is included, the ray-optics model only accurately describes the light path and spatial fluence for a low intensity beam of photon energy less than the band energy and where no material modification occurs. It merely shows where in the material laser fluence or intensity might be high enough to cause permanent damage. In order to roughly account for material modification and absorption, the laser fluence can be assumed to be entirely absorbed at and before the focus depth (z_2) in the material such that no irradiance is calculated after the focal point. Following is a two index model showing beam focus through air (n=1) into the bulk of a low index (n = 1.77) and high index (n = 3.44) material assuming the beam is entirely absorbed at and before the focal point. The average beam power is held constant at 1 mW while the focal depth is varied from 10-100 μm (see Figure 28).

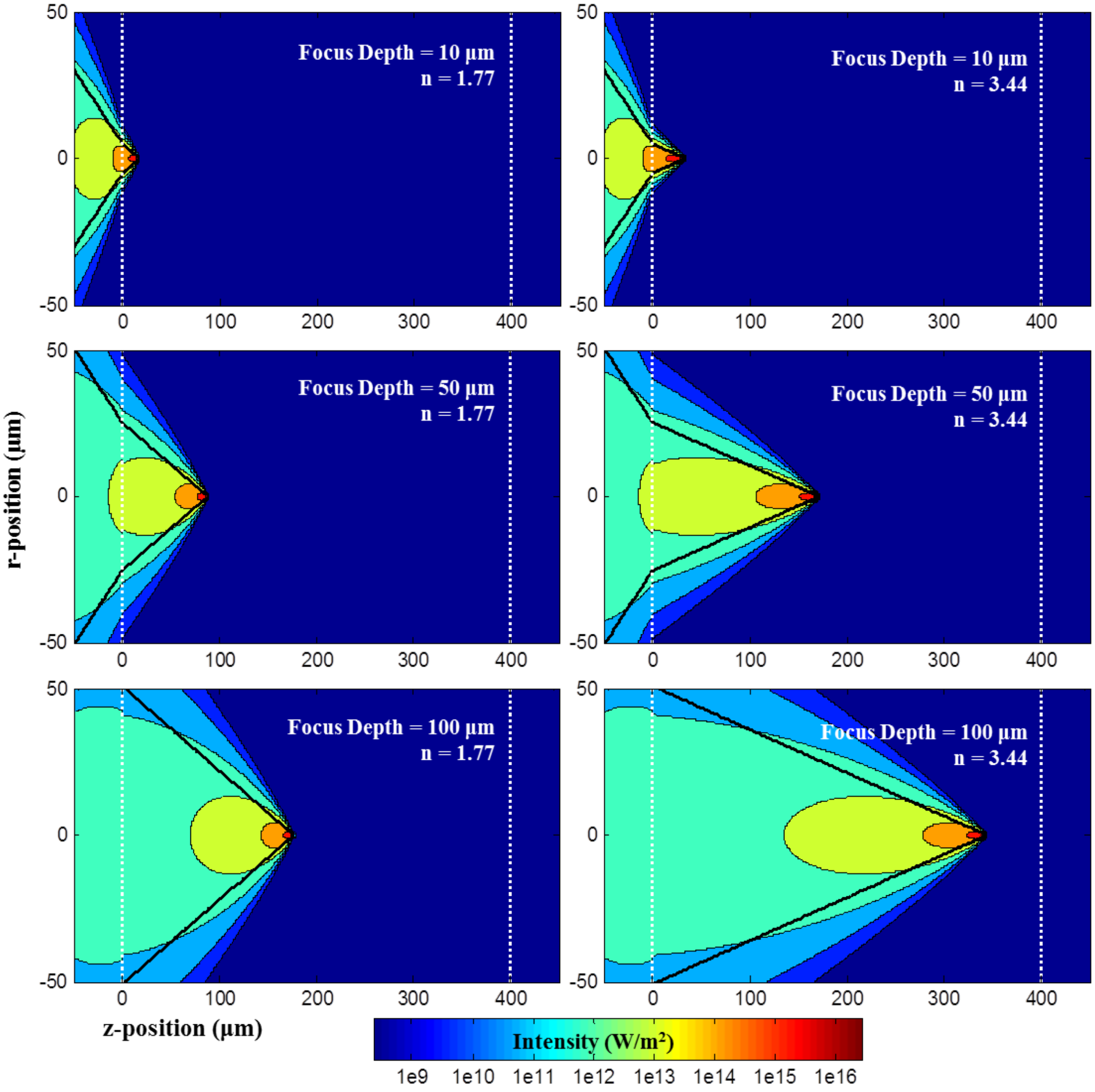

Figure 28: Ray-optics model results for various focal depths in silicon and sapphire.

The index on the outsides of the vertical white dotted line is the index of refraction for air. The material thickness was set to 400 µm for both materials. It can be seen that the higher index of refraction material stretches the actual focal depth much farther into the bulk than the lower index material. Following is the results of the optical model showing the effect of changing the optics-particularly numerical aperture. Keeping the focal depth constant at 80 μm, the average beam power at 1 mW, and same indices of refraction, the changes in spatial intensity can be seen (see Figure 29).

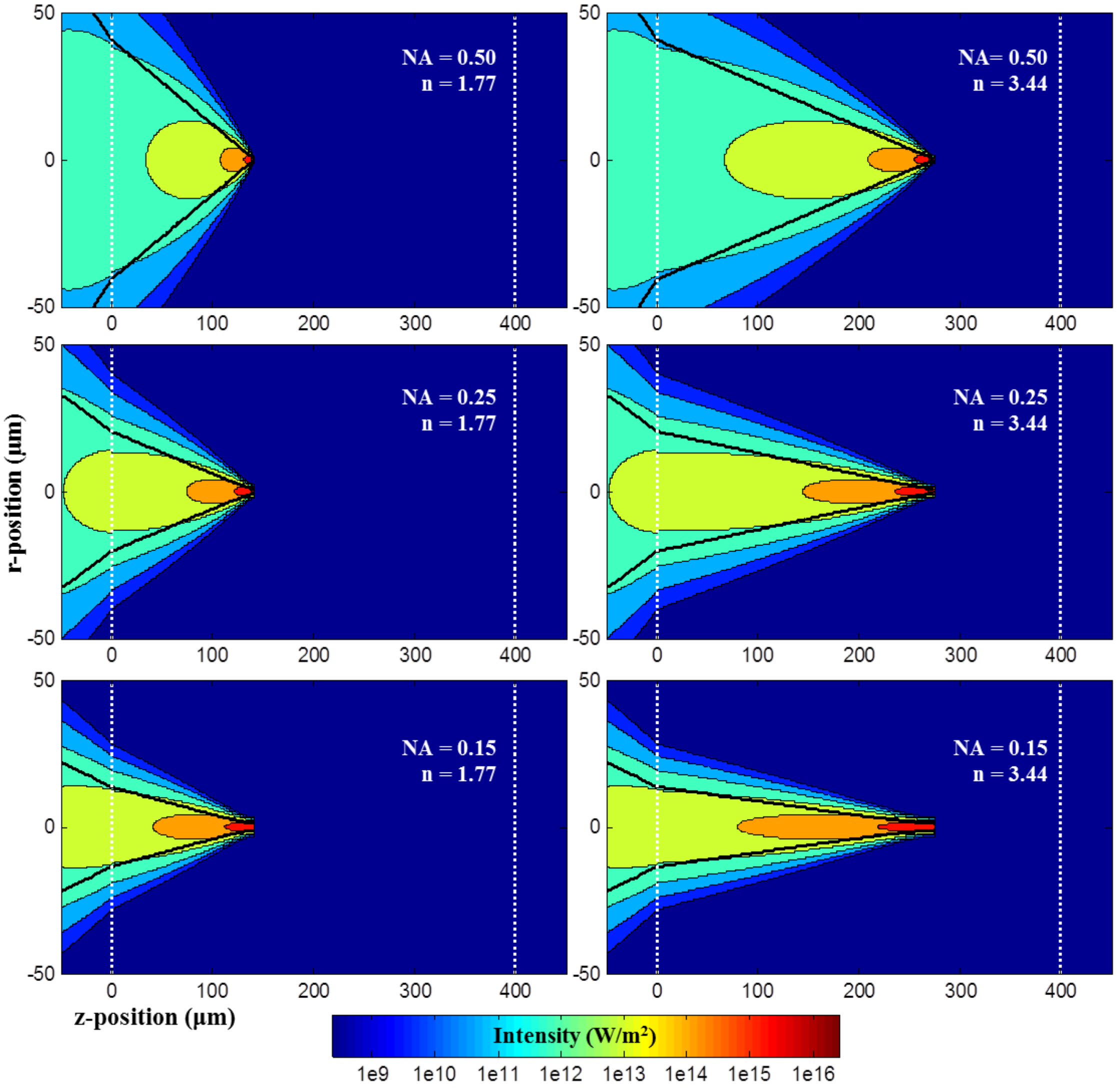

Figure 29: Ray-optics model results showing the effect of numerical aperture

It can be seen that the numerical aperture greatly affects the shape of the spatial intensity inside the bulk material. The low NA objective results in a larger Rayleigh range that might not allow for internal modification.

That the intensity is not calculated after the focal point is not an entirely erroneous assumption if the beam is operating well above the intensity or fluence for permanent material modification. As discussed in Chapter 2, after multiphoton photoionization and electron avalanche generate enough free carriers, strong plasma absorption occurs. Strong absorption will happen first at the focal point causing the material at that point to appear opaque to the rest of the incoming beam. The process of electron-plasma breakdown as it relates to high fluence laser damage will be discussed further in the electron-plasma modeling section. Regardless, subsurface damage spot depth, being the thickness in the z-direction of permanently modified material, could be calculated by finding the region where fluence equals or exceeds the laser induced damage threshold. Following is a plot showing the laser intensity at $r=0$ as a function of depth in a material with a set index of refraction of 3.44 and objective focus of 0.50 NA (see Figure 30). The average laser power was set to 1 mW and the published damage thresholds for silicon and sapphire are shown as reference points.

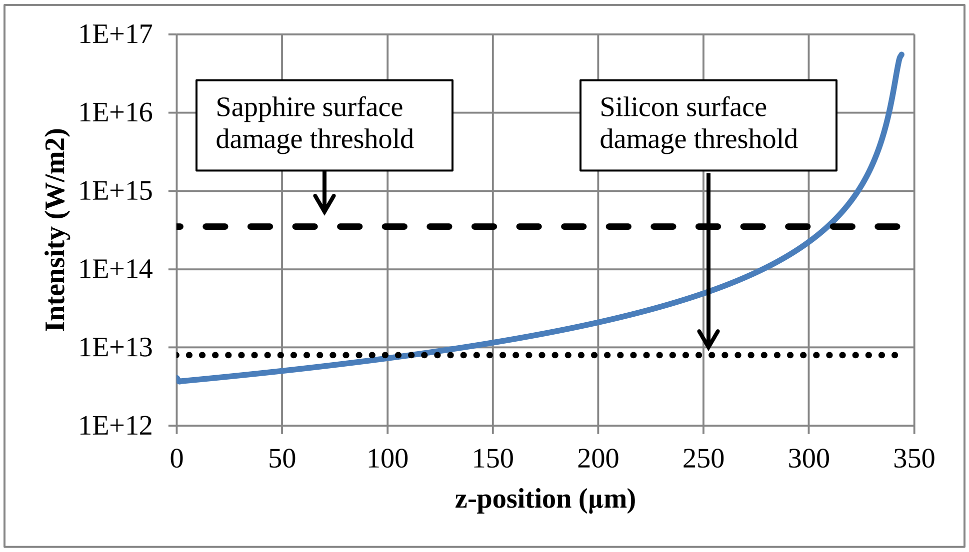

Figure 30: Intensity as a function of depth in a material

The spot depth in the z-direction that exceeds the damage threshold could be calculated from this plot. It can be seen that the region for possible damage is much larger for silicon than sapphire. The purely ray-optics model is compared to experimental results in order to show this modeling method's accuracy in the following chapter (see Chapter 4).

3.2 Electron-Plasma Laser Material Modification Model

In order to better describe the absorption process of high fluence laser light in the bulk of a material resulting in permanent damage, another modeling approach had to ensue. As discussed in the later part of Chapter 2, multiphoton photoionization and impact ionization dominate the absorption process at the intensities relevant to laser material modification. Thus to model the attenuation of the beam as it is absorbed in the material and better determine the region were permanent damage is formed, an electron-plasma model was used. Traditionally, electron-plasma breakdown is reserved for very short pulse length lasers (<20 ps), and thermal melting due to changes in absorption from phonon interaction are used to describe long pulse length laser damage [68, 73, 87, 63]. However, like for most binary assumptions, a balance should be attempted to best describe reality. Because the nanosecond regime is neither extremely short nor long pulsed, the real damage mechanism is likely to be both thermal and non-thermal. It is part of the goal of this work to show that the absorption of photon energy is best described by the carrier generation model for the 6ns laser used in damage characterization experiments; in other words, the bulk material modification that happens due to high intensity transparent light can still be described by electron-plasma breakdown in the low nanosecond time regime, but a correction factor would be expected. This approach to describe laser induced bulk damage of material is not entirely novel, but it has not been used as the sole description of the light absorption method resulting in bulk material modification from a nanosecond laser pulse.

A simple justification for an electron-plasma damage model can be found in the characteristic thermal diffusion length, which can be calculated from [88]:

$$L = \sqrt{\frac{2\tau\kappa}{\rho C}} \tag{56}$$

where κ is the thermal conductivity (W/m K), ρ is the density (kg/m3), C is the specific heat capacity (J/kg K), and τ is the pulse length of the laser. Following is a table of the physical constants for sapphire and silicon used to calculate the characteristic thermal diffusion length [89, 90].

Table 2: Material properties of sapphire and silicon

Material	**ρ (kg/m^3)**	**κ (W/m K)**	**C (J/kg K)**	**L (μm)**
Silicon	2328	150	700	1.05
Sapphire	3980	27	761	0.33

The characteristic thermal diffusion length for a 6 ns pulse in sapphire is 0.33 μm. This value is orders of magnitude less than the observed damage dimensions from a single pulse and less than the Gaussian spot size. Meaning that, although thermal properties of the material are important to modeling the damage mechanism most accurately, thermal transport is not significant enough to include the temperature dependence of light absorption for this pulse width. In other words, the change in absorption mechanism due to heating of the material does not happen on a quick enough time scale (or in a large enough volume) to effect the pulse propagation. Instead the rapidity of carrier generation and ionization better portray the light absorption and material modification process. A similar approach has been used to ignore the effects of electron diffusion on the formation of damage in the nanosecond time regime [91].

3.2.1 Transient Carrier Generation

In order to account for the transient nature of carrier generation, the original ray-optics intensity equation must be modified to include the Gaussian time dependence of the pulse energy resulting in the following description of fluence in the beam path [92]:

$$I(r,z,t) = I_o(1-R)\left(\frac{w_o}{w(z)}\right)^2 exp\left(\frac{-2r^2}{w(z)^2}\right)\exp\left(\frac{-t^2}{\tau^2}\right) \qquad (57)$$

where τ is the pulse length and the other variables are the same as in equation 53.

The rate equation for carrier generation, as presented in Chapter 2, (Equation 45) includes the Keldysh photoionization rate W_{PI} (Equation 38) and an impact ionization or avalanche ionization rate n_{ava}. The Keldysh photoionization rate describes multiphoton photoionization and tunnel ionization, where the avalanche rate incorporates free carrier absorption and impact ionization from high energy free-carriers. Following is the relationship between calculated photoionization rate from the Keldysh theory as a function of beam intensity for various wavelengths where the material band gap was set to 7.5 eV (see Figure 31).

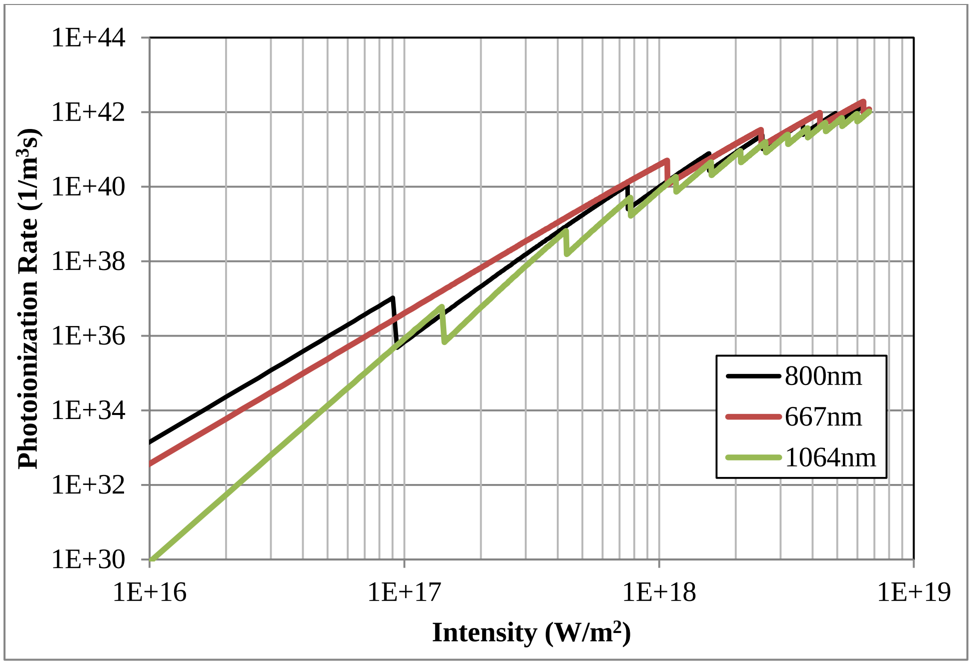

Figure 31: Photoionization rate as a function of intensity for various wavelengths

The various spikes are a result of assumptions inherent to the Keldysh model, particularly where the Bessel function in the denominator is zero resulting in a singularity. The physical explanation for the assumption is a result of transitions from different number of photon contributions [93, 94]. It can be seen that at high intensity (fluence or field), the wavelength has little effect on ionization rate [95]. Material band gap, on the other hand, has a large effect on photoionization rate which can be seen in the following figure for Keldysh photoionization rate as a function of intensity where wavelength was set to 800nm (see Figure 32).

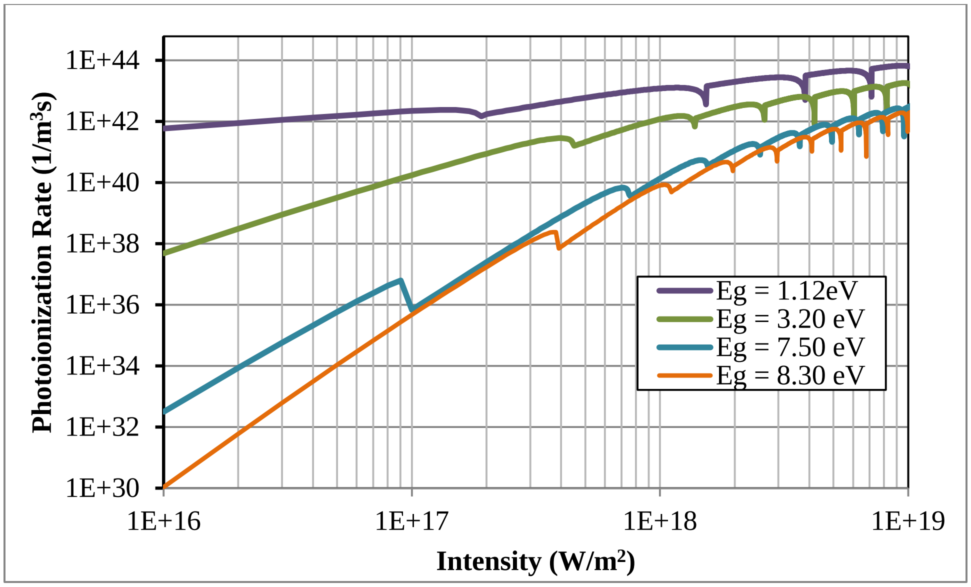

Figure 32: Keldysh photoionization rate as a function of intensity for various material band gaps

The band gap of the material has a large effect on the photoionization rate. It can be seen that for silicon depending on the assumption of indirect (Eg = 1.12 eV) or direct band (Eg = 3.2 eV) absorption, the curve for photoionization rate is substantially different. Although the Keldysh theory for photoionization does describe the onset of absorption in the rate equation, the carrier concentration dependence of avalanche or impact ionization causes it to be much more important to the transient development of carriers and absorption of light at high intensity.

There are two dominant models to describe electron avalanche, or impact ionization: Thornber model and Drude model. Thornber's model for impact ionization can be used over the Drude model due to its simplicity and accuracy when modeling laser induced electron avalanche-particularly the electric field dependence of the impact-ionization rate. According to Thronber, the impact-ionization rate as a function of electric field *E* can be calculated as [63]:

$$n(E) = \frac{v_s eE}{E_g} exp\left\{-\frac{E_{\text{I}}}{E\left(1+\frac{E}{E_{Phonon}}\right)+E_{kt}}\right\} \tag{58}$$

where v_s is the saturation drift velocity (2e7 cm/s), e is the electron charge, E_g is the band gap, E_{I}, E_{Phonon}, and E_{kt} are the field energies for carriers to overcome from scattering (ionization, optical phonon, and thermal scattering). The coefficient values were taken from Thronber's original work for silicon, and extrapolated from values for SiO_2 for modeling impact ionization in sapphire [96, 73]. The intensity of the laser light is related to the electric field by [64]:

$$I = nc_o\varepsilon_o|E^2| \tag{59}$$

where n is the refractive index of the medium, c_o is the speed of light and ε_o is the permittivity of free space. Thus the impact-ionization rate can be calculated in terms of laser light intensity $n(I)$ which will be used later to calculate the rate equation for carrier generation rate dN/dt.

The Drude model has been used by Stuart et al. and other groups to describe impact-ionization [72, 92, 64]. He determined that by the flux-doubling boundary condition, the avalanche ionization coefficient could be calculated as the cross section of inverse bremsstrahlung absorption over the effective band gap and is proportional to laser intensity [72]. Such that the avalanche coefficient can be calculated as [64]:

$$\beta = {}^{\sigma}/_{U'} \tag{60}$$

the cross section of inverse bremsstrahlung absorption is:

$$\sigma = \left(\frac{1}{nc_o\varepsilon_o}\right)[e^2\tau/m(\omega^2\tau^2 + 1) \tag{61}$$

and the effective band gap is:

$$U' = (2 - \frac{m}{m_e})(E_g + \frac{e^2E^3}{4m\omega^2}) \qquad (62)$$

where n is the refractive index, c_o is the speed of light, ε_o is the permittivity of free space, e is the charge of an electron, τ is the electron collision time (1 fs), m is the effective mass of an electron, ω is the radial frequency of the light, m_e is the free electron mass, E_g is the band gap of the material, and E is the electric field strength.

The rate equation for carrier generation taking into account Keldysh multiphoton photoionization and tunneling as well as Thronber impact-ionization can then be written as [63]:

$$\frac{dN(r,z,t)}{dt} = W_{PI}(I) + n(I) * N(r,z,t) \qquad (63)$$

where $W_{PI}(I)$ is the calculated Keldysh photoionization rate as a function of intensity I discussed in Chapter 2 (Equation 38), $n(I)$ is the Thornber impact-ionization rate as a function of intensity (Equation58,59), and $N(r,z,t)$ is the carrier concentration in the material. If the Drude model is used, the rate equation becomes [64]:

$$\frac{dN(r,z,t)}{dt} = W_{PI}(I) + \beta(I) * I * N(r,z,t) \qquad (64)$$

Following is a table summarizing the material and physical constants used to solve Thornber and Drude impact ionization rates as well as the full Keldysh multiphoton photoionization theory (see Table 3).

Table 3: Constants used to solve Thornber and Drude impact ionization rates

Constant		Silicon	Sapphire
Index of Refraction	n	3.44	1.767
Band Gap	E_g	1.12 eV, 3.2 eV	8.3 eV
Reduced Effective Mass	m_r	0.86m [64]	0.3m [97]
Saturation Velocity	v_s	1.1E5 m/s	2E5 m/s
Ionization Field	$\mathrm{E_I}$	1.66E8 V/m	3E9 V/m
Optical Phonon Field	$\mathrm{E_{phonon}}$	2.2E7 V/m	3.2E8 V/m
Thermal Field	$\mathrm{E_{kt}}$	1.15E6 V/m	1E6 V/m
Electron Mass	m	9.103E-31 kg	
Charge of an Electron	e	1.602E-19 C	
Speed of Light	c_o	3E8 m/s	
Permittivity of Free Space	ε_o	8.85E-12 F/m	
Planks Reduced Constant	$\hbar$	1.054E-34 J s	

Following is the graphical comparison of the calculated impact-ionization rates from the Drude and Thornber models for impact ionization $n(I)$ and $\beta(I) * I$ respectively (see Figure 33).

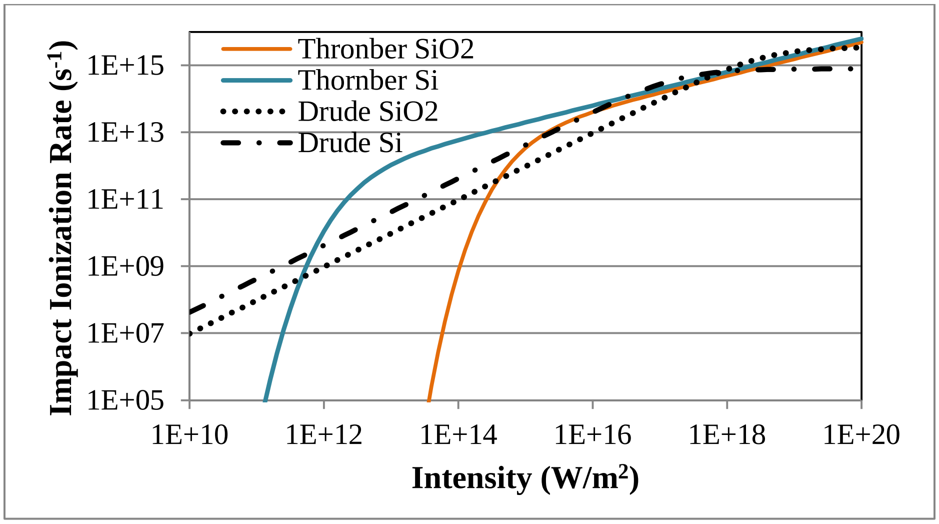

Figure 33: Comparison of Thornber and Drude models for impact ionization rate

It can be seen that the Drude model results in much higher impact ionization rate at low electromagnetic field strength and thus low light intensity. The high impact ionization rate at low intensity resulting from the Drude model causes a poor fit when compared to observed laser damage, so Thornber's approach was ultimately settled on as the best description of electron avalanche. The carrier density as a function of time can be calculated from Equation 63. Figure 34 shows the calculated evolution of carrier density from a 140 fs pulse width compared to a 6 ns pulse width laser at similar peak power in a material where E_g = 7.5 eV. The carrier density was calculated for multiphoton absorption only (MPA) as well as multiphoton absorption and impact ionization from electron avalanche (AVA) using Thornber's model as it more realistically described low filed ionization rate.

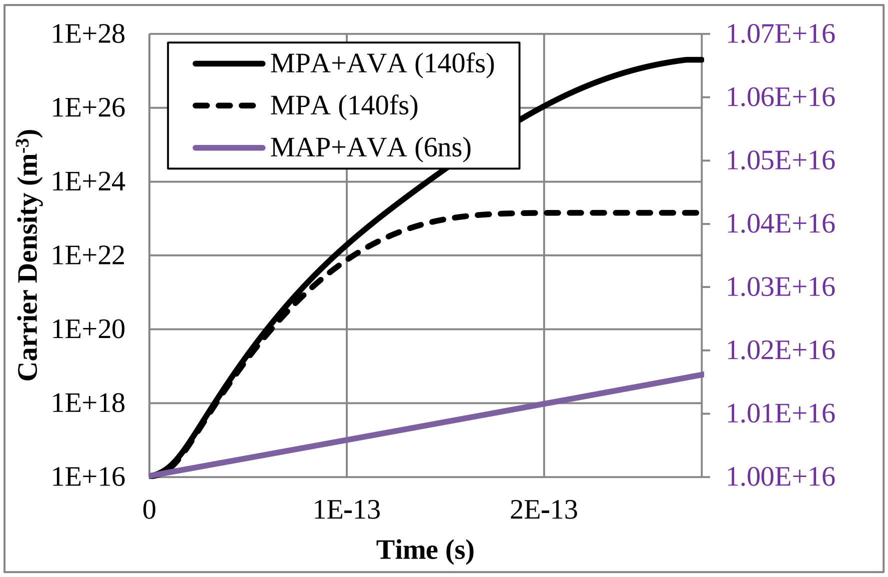

Figure 34: Carrier density as a function of time for 140fs and 6ns pulse width lasers.

When only multiphoton absorption is taken into account, the carrier density from the 140 fs laser is not high enough to cause plasma breakdown. Instead the increase in carrier density from avalanche ionization must also be included to accurately predict laser induced damage [72, 98, 99]. Because the laser power is still low early in the Gaussian beam, the increase in carrier density for the 6 ns pulse is negligible in the femtosecond time regime. However, closer to peak energy for the 6ns pulse, the photoionization rate and impact ionization rate are similar to the femtosecond values resulting high enough carrier density to cause permanent damage before carriers recombine or diffuse away. In order to account for beam attenuation due to absorption by multiphoton photoionization and impact ionization, the change in beam intensity can be described by the following equation [100]:

$$\frac{dI}{dz} = -\epsilon \frac{dN}{dt} \tag{65}$$

where ϵ is the average energy of electrons in the conduction band estimated as $1.5E_g$ [100]. The carrier concentration as a function of depth into the material can be calculated by simultaneously solving Equation 65 and Equation 63 which was done using an iterative solver in MatLab. The region in which the critical carrier density (Equation 42) is exceeded, which is about 2E27 m^{-3} for applicable wavelengths [91, 72, 76], was defined as the damaged or permanently modified volume. Following are the model results for the beam intensity in sapphire at the peak of the laser pulse ignoring absorption and accounting for absorption from the electron-plasma model (see Figure 35). The average pulse energy was set to 5 mW, the wavelength of light was 667 nm, the pulse width of the laser was 6ns, the numerical aperture of the focusing optic was 0.50, and the focusing depth was set to 150 µm.

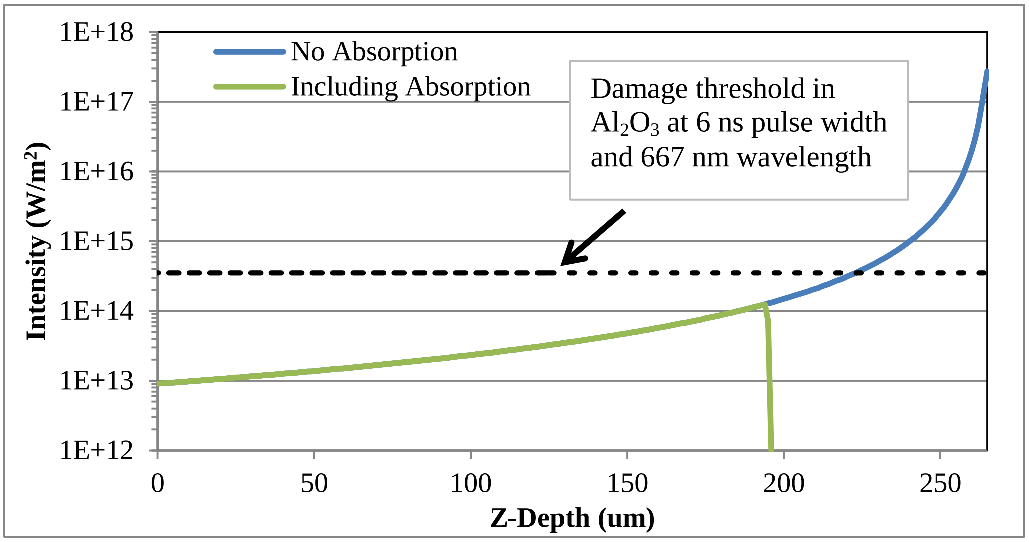

Figure 35: Electron-plasma model showing beam intensity vs depth in sapphire at peak pulse energy

It can be seen that the absorption due to multiphoton photoionization and particularly electron avalanche is very high allowing for negligible light penetration after the high carrier region. During the evolution of the beam, as the beam energy increases, the high carrier region increases in volume until the peak of the pulse is reached. Thus the electron density at the peak of the pulse will represent the largest possible material volume where permanent laser damage could occur. In silicon, the laser induced damage threshold is much lower, such that at 5 mW average power under the same focus, the damage threshold is achieved on the surface. Thus the average power has to be substantially lowered to encourage only subsurface damage. In addition, to promote multiphoton absorption and reduce linear absorption, a higher wavelength of light must be used. Following is the same plot of laser intensity as a function of depth in the material for silicon (n = 3.44) where focus depth, NA, and pulse width are the same but average power is set to 0.05 mW, and wavelength to 1.2 µm (see Figure 36).

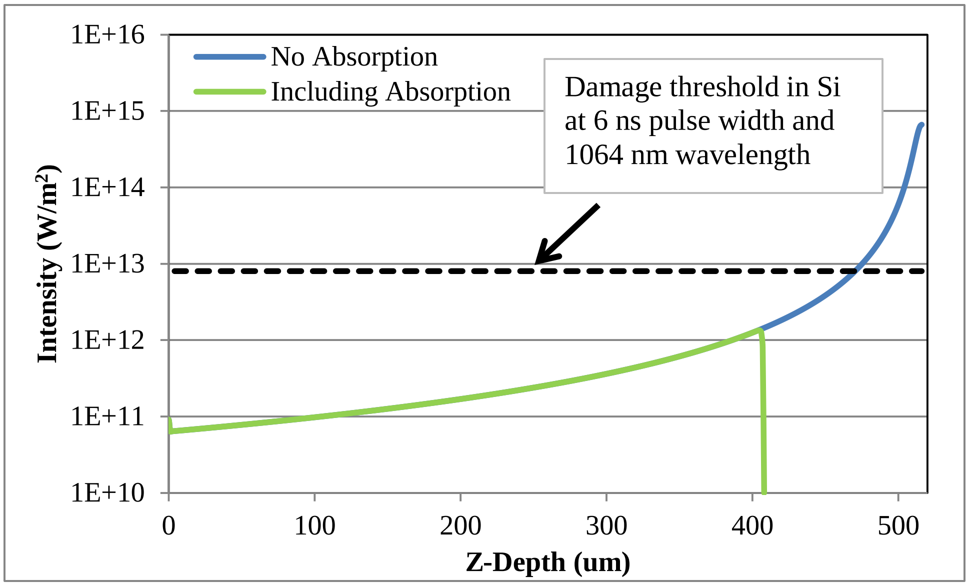

Figure 36: Electron-plasma model showing beam intensity vs depth in silicon at peak pulse energy

If the average laser power was set to 5 mW like in the previous example with sapphire, the damage would have occurred on the surface and laser fluence would not have made it into the bulk. But because fluence is only high enough to cause strong electron-plasma absorption in the bulk when 50 µW average power is used, surface damage can theoretically be avoided. Following is the electron-plasma bulk-laser damage model results for silicon and sapphire for various wavelengths (see Figure 37). The average laser power is set to 1 mW, the focus depth to 100 µm, and the numerical aperture to 0.50 for both materials. It can be seen that the wavelength changes from 600-1200 nm has negligible effect in bulk laser damage geometry in sapphire, but there is a very large effect in silicon.

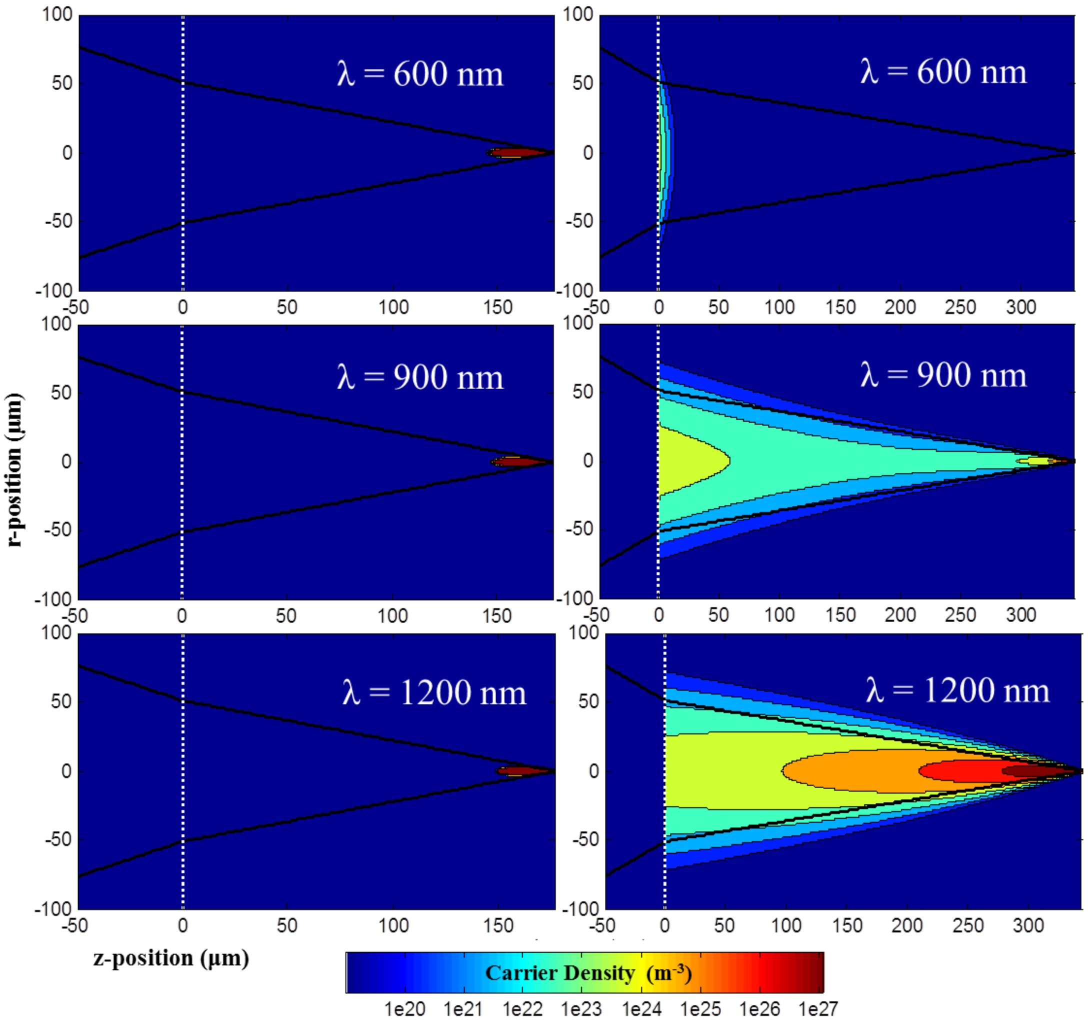

Figure 37: Electron-plasma model results for various wavelengths in sapphire and silicon

It can be clearly seen that wavelength has little effect on damage geometry in the bulk of sapphire. The independence of wavelength on photoionization rate for these wavelengths is logical because they are all of energy far below the band-gap of sapphire and the Keldysh multiphoton photoionization and avalanche ionization processes dominate. For silicon, however, 600nm (2.1 eV) and 900 nm (1.4 eV) light are both higher energy light than the band gap of silicon (1.12 eV) such that linear absorption has substantial contribution to the light absorption and carrier generation process. Thus, linear absorption is significant for lower wavelength light preventing bulk damage formation. This is consistent with other modeling efforts in silicon [74]. It is easily concluded that to generate laser damage in the bulk of a semiconductor or transparent insulator, light of photon energy less than the material band gap is suggested and at intensity low enough to avoid surface damage or self-focusing.

Chapter 4

BULK LASER DAMAGE EXPERIMENTS

This chapter presents the progress made on the design and development of a laser wafering tool and process. It also presents experimental verification of the ray-optics and electron-plasma bulk laser damage models as well as the characterization of nanosecond bulk laser damage formation in sapphire. From the onset of this project, a major hurdle was choosing and acquiring the appropriate laser system to perform subsurface laser damaging of silicon, specifically. As mentioned earlier, the original vision of the project was to design a tool that would form thin-silicon wafers in a low cost manner using a subsurface laser modification technique. As discussed in the previous chapter, the laser wavelength would need to be of photon-energy lower than the band-gap of the material. For silicon with a band-gap of 1.12 eV, the correlating wavelength is 1.1 µm. Theoretically, the laser system would have to operate at wavelengths greater than 1.1 µm to reduce linear absorption at shallow depth and allow damage to be formed deep in the bulk of the material at and around the focal point. Thus we began to look at near- to mid-infrared laser systems of high enough pulse energy to ablate silicon.

4.1 Preliminary Experimentation: XRT in Si and GaAs

As mentioned earlier, there were two near-IR laser systems available for study on ASU's campus: a nanosecond Nd:YAG pumped OPO that operated from 340-1600 nm wavelength at just enough power to ablate silicon, and a femtosecond Ti:Sapphire pumped OPA that operated from 800-1200 nm also at enough power to surface ablate silicon. Surface damage characterization tests were run on both systems to look at the focal spot interaction with the surface of the material, and it was quickly seen that both systems were capable of ablating the surface of silicon when the beam was under slight (NA = 0.1) focus (see Section 1.2). A manual micrometer-controllable x,y,z, translation stage as well as a tight focusing objective that had high damage threshold were purchased to assist in the first subsurface damage experiments. We knew that the beam would have to be extremely tightly focused to ensure that the focal point was as small as possible so that damage was more likely to be formed only at and near the focal point. Thus we purchased NA = 0.28 and NA = 0.50 reflective objectives with gold protective coating which increased the reflectivity and damage threshold for near-IR light. Light was focused at the surface of the material and at various depths incrementally stepping into the material to attempt to generate damage at multiple levels in the bulk in a periodic arrangement of locations relative to the surface of the wafer. This procedure was run using both the nanosecond and femtosecond laser systems on Si and GaAs at various average power levels from 0.25 mW to 30 mW, and the damage was inspected with optical and IR microscopy as well as x-ray topography (XRT) to observe permanent lattice changes. The XRT image was compared to optical microscopy images at the focal spots to look for discrepancy: if a spot was seen in the XRT image and not in the optical microscope image, it could be assumed that subsurface damage was successfully formed. Following is an image of the XRT scan compared to optical microscopy (see Figure 38).

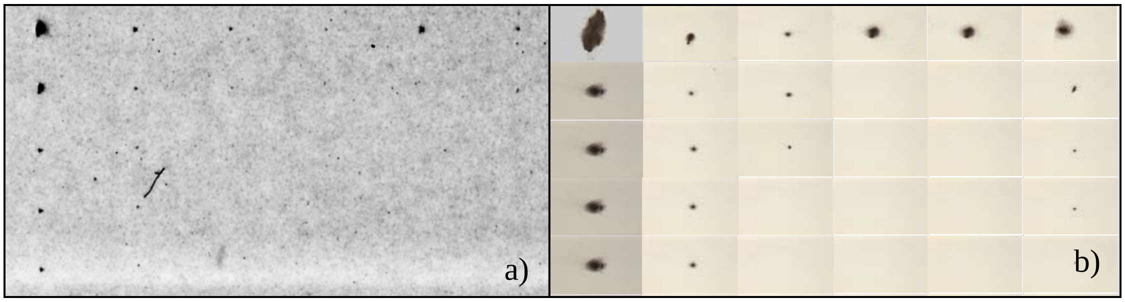

Figure 38: Silicon [100] after periodic ablation spot formation from 140 fs, 1200 nm, 1 kHz laser a) x-ray topography, and b) optical microscope images

The XRT scan was just high enough resolution under slight magnification (digital or optical) to see the dark spots correlating to permanent lattice changes. The XRT image was then compared to the images observed with the optical microscope to see if permanent lattice changes were formed where there was not visible surface damage. Following is the first XRT image of a full GaAs wafer ever performed at the LeRoy Eyring Center at ASU. The crystal defect spotting made it impossible to distinguish laser damage from vacancies and point defects in the GaAs lattice (see Figure 39).

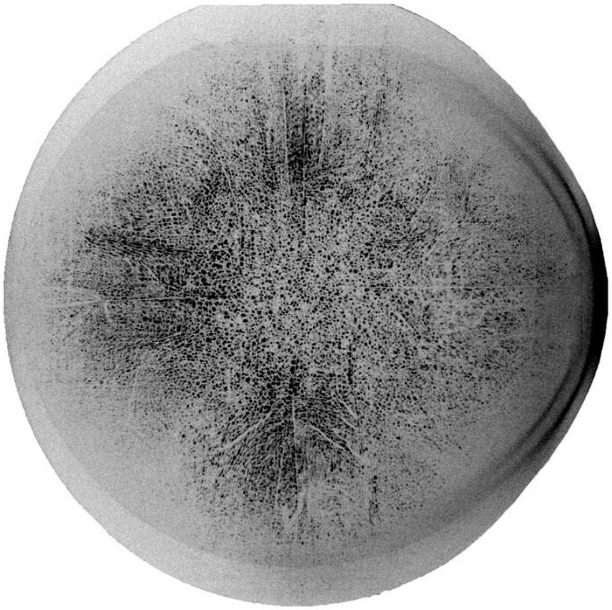

Figure 39: XRT Image of GaAs wafer

The femtosecond and nanosecond pulse width lasers were both unsuccessful in demonstrating permanent subsurface damage in this way in Si and GaAs. From this failure, other tests were attempted including pattern formation that might allow for lower resolution XRT detection of permanent subsurface lattice modification, IR-microscopy compared to optical microscopy imaging, and through-to-rear side ablation to attempt to ablate the rear side of the wafer through the material leaving the front surface unaltered. All showed that either subsurface damage was not being formed in Si or GaAs at these focuses (0.28 and 0.50 NA), these average power levels (0.25-30 mW), or with these pulse lengths (10 ns or 140 fs), or that XRT and IR-microscopy were not adequate imaging methods. Thus, to better understand laser induced subsurface damage formation and make progress on a proof of concept for the laser wafering project, the direction of investigation moved from bulk silicon laser damage formation towards wide band gap transparent crystals [101, 102]. For decades, fused silica has been patterned in the bulk using sub-surface laser techniques for ornamentation purposes as well as three-dimensional photonics [103], biochip device fabrication [104], and three-dimensional optical storage [105]. Thus the decision was made to investigate bulk laser damage formation in a transparent crystalline material. Having large recycled quantities on hand combined with potentially more marketable applications, sapphire became the material for investigation and a nanosecond variable wavelength laser was the tool of choice.

4.2 Bulk Laser Modification of Sapphire

The following section presents the setup, experimentation methods, and results achieved characterizing the bulk laser damage formation process in sapphire wafers and the applicable controls over the damage geometry. In addition, it provides ray-optics and electron-plasma model comparison to the achieved damage geometries for a given laser power, numerical aperture, wavelength, and number of laser shots.

4.2.1 Variable Wavelength Laser

A variable wavelength laser was settled upon as the best possible experimentation tool for two reasons; firstly, the variable wavelength aspect of the tool made for a useful research device, and secondly, nanosecond regime was the shortest pulse length affordable. An Ekspla NT-352A was purchased as it was a higher peak beam power version with a wider wavelength range than the nanosecond tool used for preliminary studies. Following is a photograph of the laser system and the control pad on the optical table (see Figure 40).

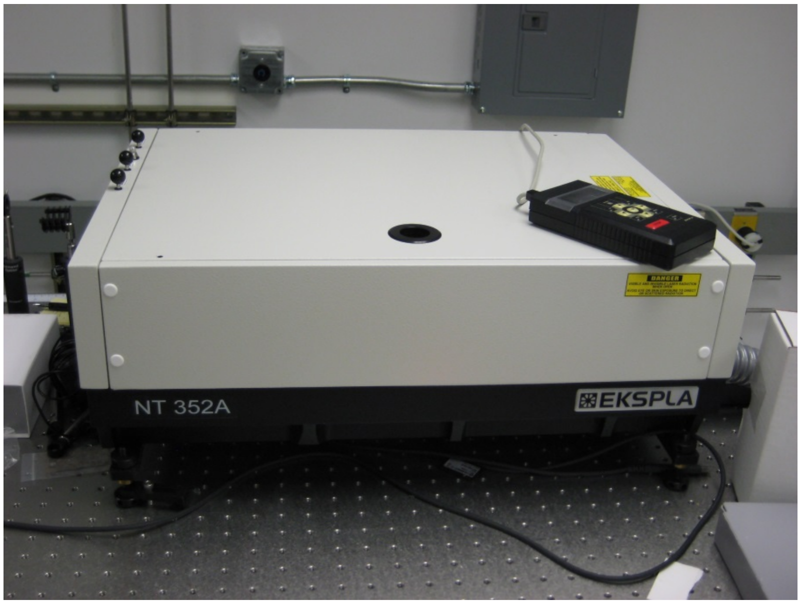

Figure 40: NT-352A variable wavelength laser and handheld control pad

The Ekspla NT-352 system included a pump which was a 532nm Nd:YAG pump laser and an optical parametric oscillator (OPO) system. Following is a table summarizing the variable wavelength laser system specifications (see Table 4).

Table 4: Ekspla NT-352A system specifications [106]

OPO	
Wavelength range:	
Signal	670-1064 nm
Idler	1065-2600 nm
Linewidth	<10 cm^{-1}
Scanning step:	
Signal	0.1 nm
Idler	1 nm
Pulse duration:	
Signal	3-5 ns
Idler	3-5 ns
Polarization:	
Signal	horizontal
Idler	vertical
Pump Laser	
Pump wavelength	532 nm
Max pump pulse energy	230 mJ
Pulse duration	6ns
Beam quality	Gaussian in far field
Beam divergence	< 0.5 mrad
Pulse energy stability (Std. Dev.)	< 2.5 %
Typical beam diameter	6 mm
Pulse repetition rate	10 Hz

The system could operate at a large range of wavelengths with narrow line width (<10 cm-1). In addition, the pulse energy at all wavelengths in the operating range was high enough to cause permanent surface damage on silicon under appropriate focus. Following is a plot showing the maximum energy per pulse at any given wavelength the Ekspla-NT352A system can achieve (see Figure 41).

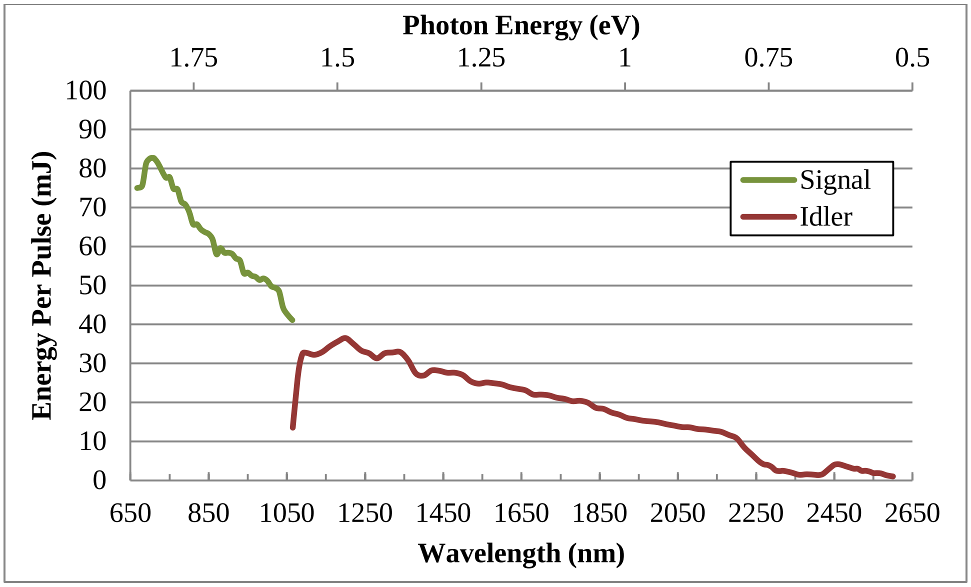

Figure 41: Maximum energy per pulse vs wavelength or photon energy for the Ekspla NT-352A variable wavelength laser system

The OPO operates in a signal mode from 667-1064 nm wavelength range then an idler mode from 1065-2600 nm in accordance with the following equation [95].

$$v_p = v_s + v_i$$

where v_p is the frequency of the pump laser, v_s is the signal frequency and v_i is the idler frequency. Depending on the desired wavelength, the signal or idler is removed using a Rochon prism. Wavelength could be set by the handheld control pad or by command via RS232 port. In addition, the energy per pulse from the Nd:YAG could be diminished by increasing the delay time between the flash lamp and the electro-optical signal (EO delay) which is also controlled by the handheld control pad or RS232. Following is a picture of the internal components of the variable wavelength laser system (see Figure 42).

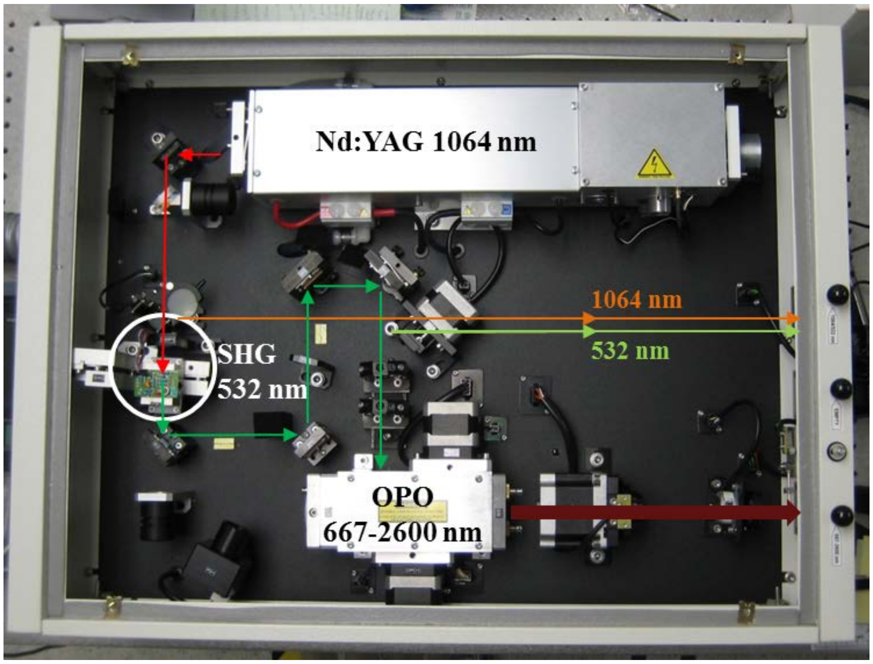

Figure 42: Internal optical components of variable wavelength laser system including Nd:YAG laser source, SHG crystal, and OPO

The second harmonic generating crystal (SHG) is a very efficient frequency doubler (50% conversion efficiency) and outputs the 1064nm Nd:YAG beam at 532 nm such that a mirror bypass can be setup to allow very high energy 532 nm or 1064 nm light out of the system without passing through the OPO (orange and light green arrows in Figure 42). The OPO takes in 532 nm light from the SHG and outputs 667-2600 nm light at up 20% conversion efficiency depending on the desired wavelength.

4.2.1 Preliminary Bulk Laser Damage Experiments in Sapphire

The preliminary experiments of bulk laser damage formation in sapphire wafers required fine positional control of the substrate relative to the focused beam path as well as control of the energy per pulse or average beam power. The manual three-dimensional stage setup was used to define the x,y,z position of a sapphire substrate in space with micrometer resolution, and neutral density (ND) filters in combination with EO delay adjustments were used to control average beam power. The basic experimental setup can be seen in Figure 43.

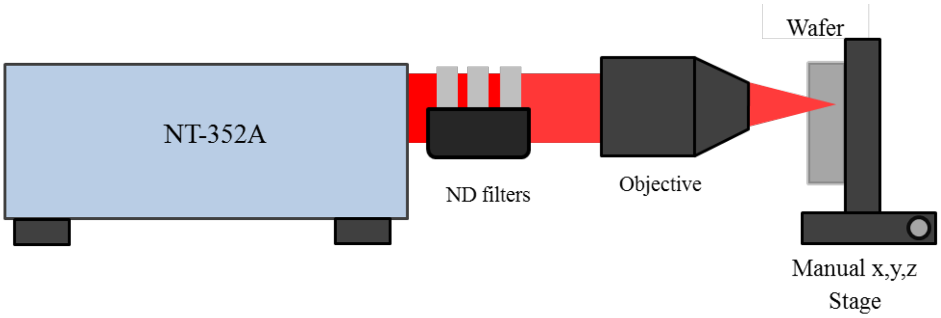

Figure 43: Manuel stage subsurface laser damage formation experimental setup

In early attempts to create damage in the bulk of the material, the focal point was stepped starting from the surface into the bulk and out the rear side at different positions on the wafer and at various power levels for about 10 pulses (1 second). The damage was inspected using an optical microscope focused at the front surface, middle, and on the rear surface to distinguish between surface and subsurface damage. Some of the early damage results for the NA =0.50 objective at 667 nm wavelength can be seen in the following figure (see Figure 44).

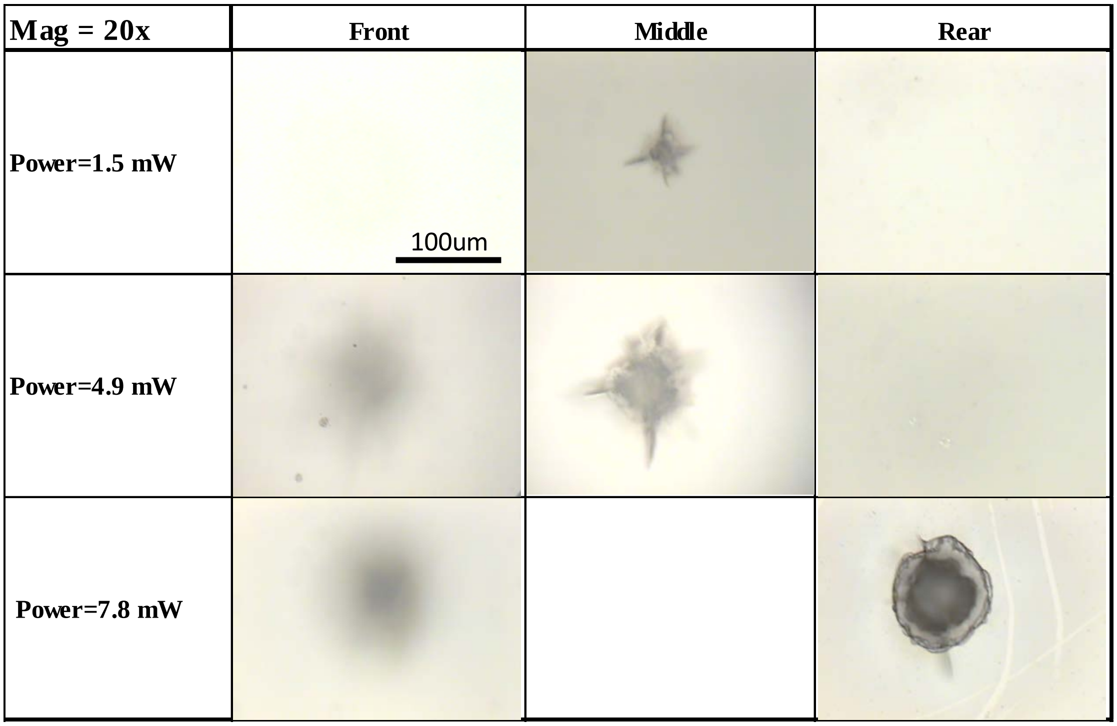

Figure 44: Optical microscope image of preliminary subsurface laser damage in sapphire wafer using variable wavelength nanosecond laser

The front and rear images show no permanent laser damage on the surfaces for the 1.5 mW and 4.9 mW average power. However, for the 7.8mW power at this focus depth, the damage exploded out the back of the wafer and was not contained in the bulk. It can be seen that at 1.5 mW average beam power a smaller subsurface (bulk) damage spot was generated than at 4.9 mW. This was expected and led to the following characterization experiments.

4.2.2 Bulk Laser Damage Characterization: Experimental Setup

In an attempt to expedite experimentation and to make progress on a laser wafering tool, a system was designed using a LabView program to integrate the laser system with a three dimensional automated stage. The stage was built using three

LTS300 stages from Thorlabs with 100 nm control and micrometer repeatability. Following is a table of the automated stage specifications (see Table 5).

Table 5: Specifications for ThorLabs 300mm linear translation stage (LTS300) [107]

Travel Range	300 mm (11.8")
Horizontal Velocity (Max)	50 mm/s
Vertical Velocity (Max)	3 mm/s
Minimum Achievable Incremental Movement	0.1 µm
On-Axis Accuracy	5.0 µm
Bidirectional Repeatability	2 µm
Backlash	2 µm
Horizontal Load Capacity (Max)	15 kg (33.1 lbs)
Vertical Load Capacity (Max)	4 kg (8.8 lbs)

By stacking the stages in an x, y, z orientation, the three-dimensional position of a wafer could be precisely controlled by LabView software. Following is a photograph of the automated stage setup (see Figure 45).

Figure 45: 3D automated stage setup showing x,y and z axis.

The LabView software was programmed to allow for multiple types of laser damage experiments by controlling number of shots, wavelength, energy per pulse, and damage pattern in a recipe format. Following is a screenshot of the LabView control panel (see Figure 46). The programming will not be discussed in detail, but it can be seen from the panel that position in space, space between damage spots, various patterns, and laser parameters can all be decided and set by the program.

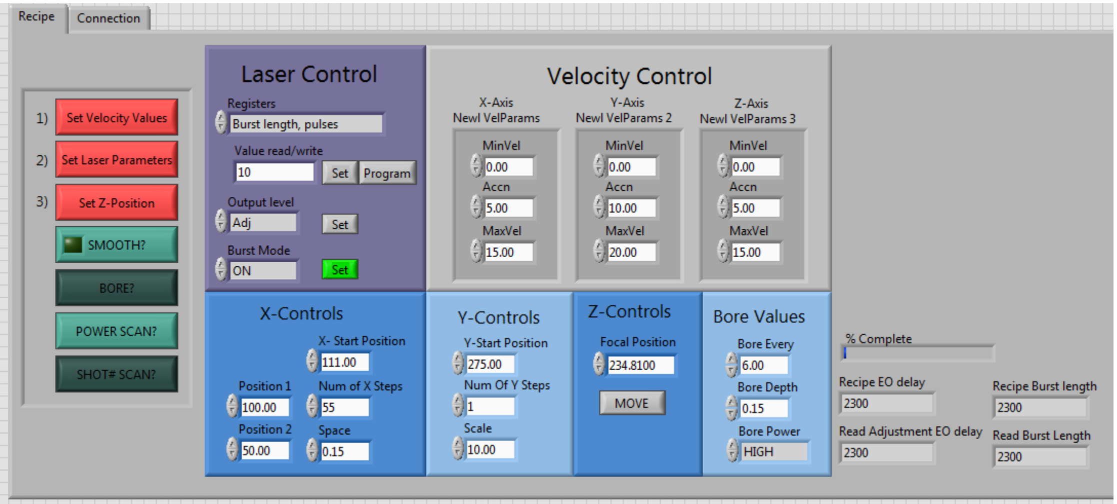

Registers: Burst length, pulses
Value read/write: 10
Output level: Adj
Burst Mode: ON

X-Axis Newl VelParams: MinVel 0.00, Accn 5.00, MaxVel 15.00
Y-Axis Newl VelParams 2: MinVel 0.00, Accn 10.00, MaxVel 20.00
Z-Axis Newl VelParams 3: MinVel 0.00, Accn 5.00, MaxVel 15.00

X- Start Position: 111.00
Position 1: 100.00
Num of X Steps: 55
Position 2: 50.00
Space: 0.15

Y-Start Position: 275.00
Num Of Y Steps: 1
Scale: 10.00

Focal Position: 234.8100

Bore Every: 6.00
Bore Depth: 0.15
Bore Power: HIGH

% Complete
Recipe EO delay: 2300
Recipe Burst length: 2300
Read Adjustment EO delay: 2300
Read Burst Length: 2300

Figure 46: Screenshot of LabView control panel showing laser and stage motion controls

The laser and stage parameters could both be controlled in the custom LabView program. In addition, a few specific experimental recipes were developed to aid in characterizing the subsurface laser damage formation parameters. The basic equipment setup for the subsurface damage characterization experiments can be seen in the following figure (see Figure 47).

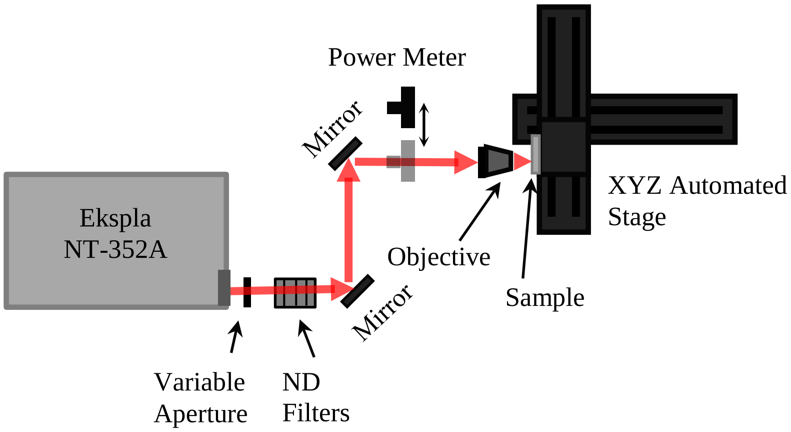

Figure 47: Experimental setup showing laser source, beam path, optics and peripheral instruments

A PC with LabView capabilities was used to run the software controlling the laser and stage. Reflective neutral density (ND) filters were used to further reduce and determine average laser power beyond the internal EO delay control. Two types of completely reflective mirrors were used such that high reflectance (>99%) could be maintained over the large wavelength range. Multiple types of focusing optics were tested before two reflective objectives (NA = 0.50 and NA = 0.28) were decided upon as the preferable beam shaping devices for study.

4.2.3 Clean Cleave Recipe

The LabView control system was programmed with a few predetermined motion pattern recipes for the subsurface damage characterization experiments. The first was a scanning recipe that allowed for smooth scans across the wafer where the scanning velocity, distance between line scans, and scan area could be set. The scan recipe, called "SMOOTH", was mostly used for 2D scans to form subsurface damage arrays and will be discussed further in the following chapter. Another recipe used for characterizing the effects of numerical aperture, energy per pulse, wavelength, and number of shots included a pause at each x, y, and z position in a line. The distance between pauses and the number of shots, energy per pulse, or wavelength could be set for each pause position. In order to observe the subsurface laser damage and quantify it efficiently, a recipe was developed that ensured a clean cleave independent of subsurface damage geometry. A preferential cleavage-plane was formed by laser drilling through the wafer every 1.2 mm which was controlled by the LabView "BORE" recipe. Following is a schematic of the cleavage plane formation process that allowed for cross-sectional inspection of the subsurface damage (see Figure 48).

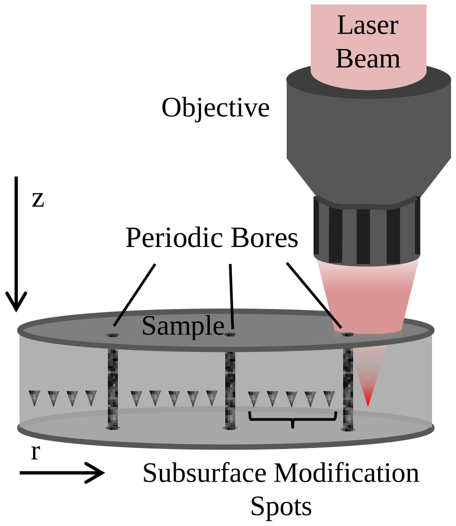

Figure 48: Schematic of subsurface laser damage formation process and preferential cleavage plane formation showing the laser drilled holes (Bores) and subsurface modification spots

Although not necessary for lines of subsurface laser damage of large volume or high pulse energy, the laser "BORE" recipe was developed to improve the yield of the cleaving process and allow for observation of very small subsurface damage geometries.

The spacing between bores was chosen over the course of many attempts to consistently cleave sapphire in any orientation, and although not an optimized parameter, 1.2 mm spacing allowed for very consistent cleaving success.

In addition to the clean cleave recipe using periodic bores, an entirely subsurface laser dicing process was parameterized during the attempts to consistently cleave sapphire along laser damage lines. Successful dicing of 2" round DSP sapphire wafers was performed using 667 nm laser light focused 200 µm into the bulk of the material (see Figure 49).

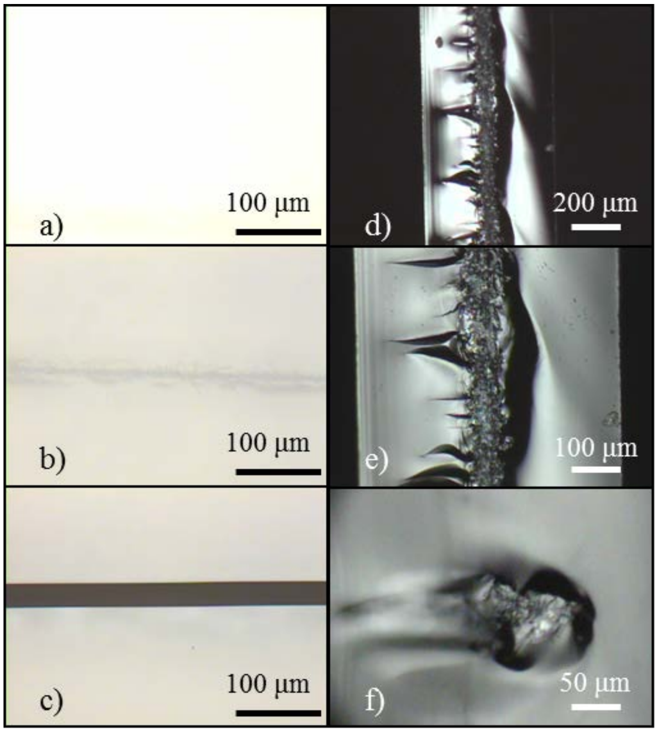

Figure 49: Optical microscope image of subsurface laser dicing. a) microscope focused at top surface, b) microscope focused in bulk, c) top surface after dice, d) cross section of subsurface laser damage, e) cross section at higher magnification, f) cross section of single damage spot

It can be seen from optical microscope images a) and b) that permanent laser damage is contained entirely in the bulk of the material as no surface damage is observable. Image c) shows the cleanness of the cleave from the top down after the dies were separated. Images d) and e) show the cross section of laser damage after dicing. This particular line of subsurface damage was formed using a 0.50 NA objective with pulse energy of 330 µJ and stage scanning velocity of 1.5 mm/s.

Subsurface laser dicing is of use to the semiconductor industry as it reduces particle generation which can cause catastrophic loss and large yield reduction in cleanroom environments. This process was successfully verified in sapphire wafers for a variety of die sizes, pulse energies, and scanning speeds. By optimizing subsurface damage spot volume with numerical aperture of the focusing optic as well as incident beam energy, along with the density of damage spots by varying scan speed of the stage, the dice process can be optimized for desired substrate dimensions, throughput, and/or cleanness of cut. This is not the first time a subsurface laser dicing process has been successfully attempted in transparent crystalline materials. In fact, it is a commercialized process for sapphire [108] and silicon [109], but as far as the author knows, this process has not been attempted at 667 nm or subsequent laser wavelengths and has not been published about revealing successful processing parameters and optimization. Thus, this is the first known discloser of a subsurface laser dicing process for sapphire.

4.2.4 Bulk Laser Damage Characterization: Energy per Pulse

The first subsurface laser damage characterization results to be discussed concern the effect of pulse energy and numerical aperture on damage geometry. The Ekspla NT-352A laser was used to generate 10-500 µJ pulses at 667 nm wavelength. The pulse length was 6 ns and repetition rate was 10 Hz, so the average measured power for the subsurface laser ablation experiments was measured between 0.01 mW and 5.0 mW using a thermopile sensor. For the following results, the beam was focused down to sub-micrometer spot sizes using one of two high numerical aperture objectives: an Edmund Optics Techspec reflective objective (NA = 0.28), and a ThorLabs LMM-40X-UVV reflective objective (NA =0.50). Both had greater than 85% reflectivity at 667 nm wavelength. For these experiments, a line damage was formed beneath the surface of <001>, double side polished, 2" diameter, 440 μm thick sapphire wafers with a spot every 0.2 mm in the r-direction and focused at a z-depth of 100-180 μm into the sample.

After the line of subsurface damage spots and periodic bores were created, the sample was inspected using an optical microscope on the surfaces to look for visible surface damage or ablation. The sample was then cleaved and the cross section imaged using a Zeiss optical microscope at varying magnifications. The z-direction spot depth and r-direction width of the subsurface damage regions were measured and the averages found for varying incident laser power (pulse energy) and numerical aperture.

Following are results from two of the experiments run where the energy per pulse was varied from 15-210 μJ for the NA=0.50 and from 40-475 μJ for the NA = 0.28 objectives for a single laser shot focused at 150 μm depth (see Figure 50). Twenty-five damage spots were made beneath the surface at the specified increments of laser energy per pulse and the damage spot dimensions were measured using the optical microscope. It can be seen that for the higher numerical aperture objective, the aspect ratio (depth: width) is smaller (≈1.3) than for the lower numerical aperture objective (≈3.6) and doesn't vary much with energy per pulse for either objective. The aspect ratio consistency, despite varying incident laser power, would imply that self-focusing is being avoided and an optical filament is not being produced through the bulk of the material resulting from the intensity dependence of the refractive index of sapphire. This is expected because even for 1 mJ pulse energy, the peak power is 0.167 MW for 6 ns pulses were the critical power for self-focusing in sapphire is 1.23 MW.

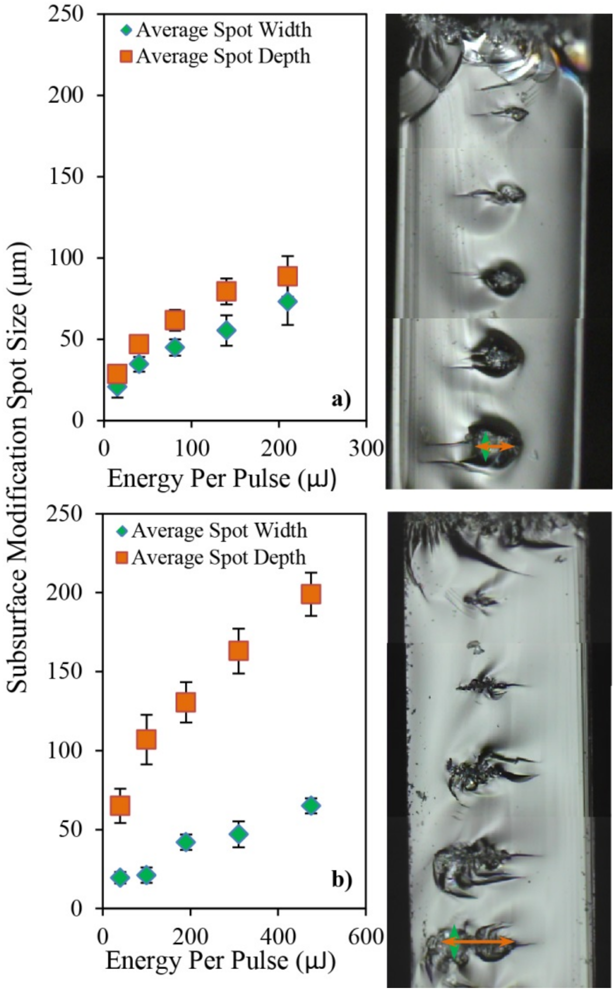

Figure 50: Average spot width and depth of the modified region formed beneath the surface of sapphire from a single laser shot at varying incident pulse energies and optical microscope image of the cross-section of a wafer for a) NA=0.50, and b) NA=0.28 objectives.

It can be seen from the optical microscope images that there was a region of what appeared to be amorphous or polycrystalline sapphire in the focal volume of the beam and stress fractures propagating varying distances away from the modified volume. The smaller spot sizes generated from the higher numerical aperture objective and lower energy per pulse have fewer and smaller observable fractures. It is not known if the fractures are a result of cleaving or from a localized change in material density at the focal point and thus high stress regions formed immediately after laser melting and solidification. Time-dependent stress imaging would need to be used to determine the stress formation process at the focal point, and thermal modeling could help predict cracking regions.

Following is a figure comparing an example of the ray-optics and electron-plasma model results to a microscope image of a cross section of subsurface damage in sapphire (see Figure 51).

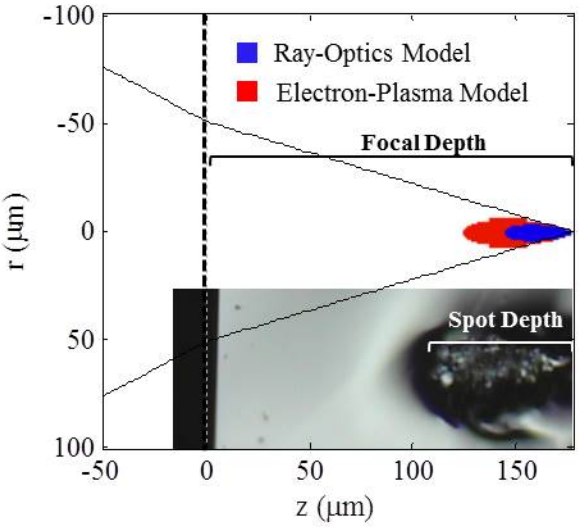

Figure 51: Ray-optics and electron-plasma bulk laser damage models compared to optical microscope image of bulk damage region. Damage spot formed from a single laser pulse at 315 μJ energy per pulse, 667 μm wavelength, focused 100μm beneath the surface with NA=0.50 reflective objective.

Both subsurface focus models seem to somewhat accurately predict the shape and depth of the damage formed in the bulk of sapphire for this case, but both underestimate the damage region. This is expected due to the model ignoring thermal diffusion, electron diffusion, and non-ideal optical effects. A comparison of the modeled and experimental results at a variety of pulse energies can be seen in Figure 52.

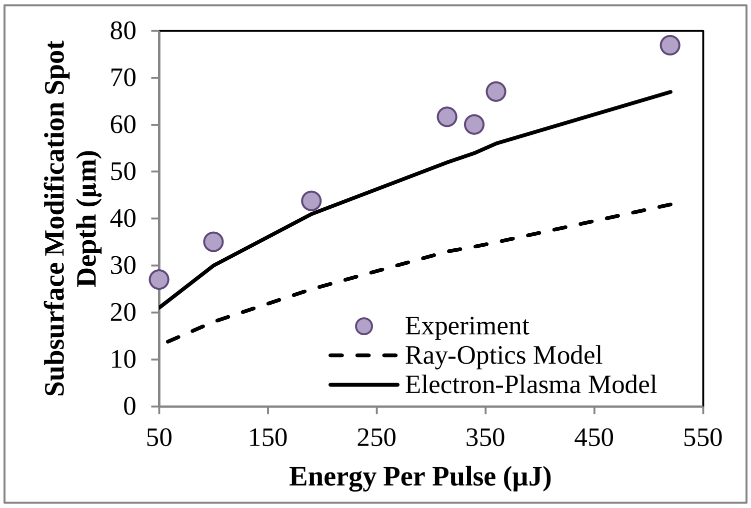

Figure 52: Subsurface laser modification spot depth as a function of pulse energy for NA of 0.50 and 667 nm laser wavelength

Again it can be seen that both models underestimate the damage dimensions albeit just slightly for the electron-plasma model. The electron-plasma model very accurately predicts damage dimensions in the z-direction for this range of pulse energies. Damage in the r-direction or the spot width is not included as it was of less importance to the elimination of surface damage and the reduction of kerf for potential wafering applications. Regardless, the electron-plasma model accurately predicts damage width and volume in general. Following is the subsurface laser damage spot depth as a function of energy per pulse for a NA = 0.75 microscope objective (see Figure 53).

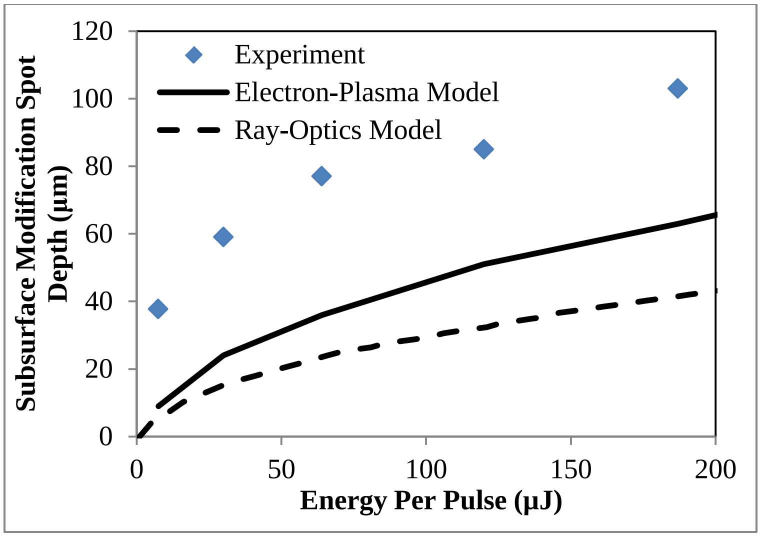

Figure 53: Subsurface laser modification spot depth as a function of pulse energy for NA of 0.75 and 667 nm laser wavelength

The electron-plasma and ray-optics models both more substantially underestimate the experimentally measured subsurface modification spot depth for the 0.75 numSubuerical aperture optic. This larger offset compared to the results for the 0.50 NA objective can be explained by the non-ideal optical effect of spherical aberration. The 0.75 NA lens used in this experiment was a refractive microscope objective comprised of a series of concave and convex glass lenses optimized for microscope viewing. Refractive lenses suffer more from aberration than reflective lenses [110] and thus the actual beam shape and fluence is not accurately predicted by the model. The laser wavelength was also varied to observe its effect on subsurface laser damage formation in sapphire, and no distinguishable effect was observed between 667 and 1200 nm light; this conclusion is supported by the model. Higher wavelengths were not attempted experimentally in sapphire.

4.2.5 Bulk Laser Damage Characterization: Number of Pulses

In order to characterize the effect of number of laser pulses exposed at a given subsurface position in x, y, z space, a set of experiments was run to observe bulk damage volume as it relates to number of pulses. The same "BORE" recipe was used as in the previous section, however instead of varying energy per pulse; the number of pulses was varied. For a given objective, 25 individual damage spots were formed at five different number of shots settings (1, 5, 10, 15 and 25 shots or pulses). Figure 54 shows the increase and plateau of the subsurface damage spot depth with increasing number of laser shots.

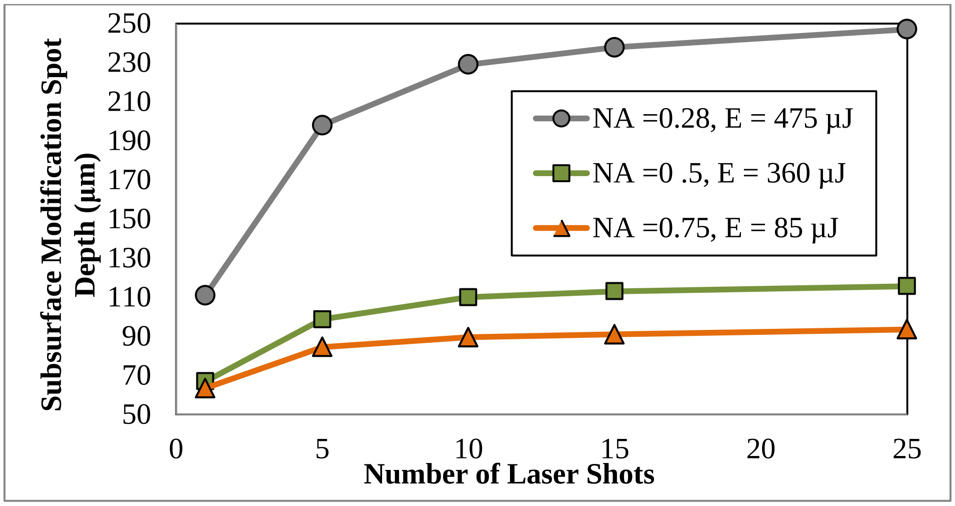

Figure 54: Plot of subsurface modification spot depth as a function of number of laser shots under focus from numerical aperture NA = 0.50, NA = 0.28, and NA = 0.75 objectives

The linear rise and ultimate saturation correlate well with other observed surface ablation experiments in a multitude of materials [111, 112, 113, 114]. It has be shown in other published work that there is a maximum surface ablation hole depth that can be achieved at a given laser power and focus independent of the number of laser shots, specifically at high numerical aperture focus or when self-focusing is avoided [115]. The occurrence of a maximum spot depth seems also to hold true for subsurface damage formation. In addition, the increase in subsurface modification spot depth is linear for low number of shots and is logarithmic until the damage depth reaches saturation which has been seen in previous work for surface ablation [111, 114].

In order to form a comprehensive model describing and predicting subsurface laser damage, an empirical correction factor was calculated for number of shots by fitting a curve to the results in Figure 54. Subsurface Modification spot depth as a function of number of laser shots was best fit by a power function in the form of:

$$f(x) = a * x^b + c \tag{66}$$

Following is a table listing the coefficients for the power fit for three objectives (see Table 6).

Table 6: Coefficients for power fit of spot depth as a function of number of pulses

	NA = 0.28	**NA = 0.50**	**NA = 0.75**	**R^2**
a	-193.7	-66.88	-36.29	0.999
b	-0.3894	-0.4227	-0.5379	0.999
c	304	133.8	99.79	0.999

The R^2 values show that the curve fit to a power function is appropriate. From the curve fit, the correction factor from 1 to any number of pulses could be found. The correction factor was between 1.4 and 2 depending on the focusing optic and pulse energy; representing an increase in subsurface modification spot depth from one to ten pulses. By multiplying the modeled subsurface laser spot damage dimension by the correction factor for number of shots, an accurate prediction of subsurface laser damage depth was found for multiple pulses. Figure 55 shows the subsurface damage spot depth achieved for various pulse energies from 10 laser pulses per damage spot. The modeled results for the 0.28 and 0.50 numerical aperture objectives are compared to the observed modification depths inside the bulk of the sapphire wafer as measured using optical microscopy (see Figure 55).

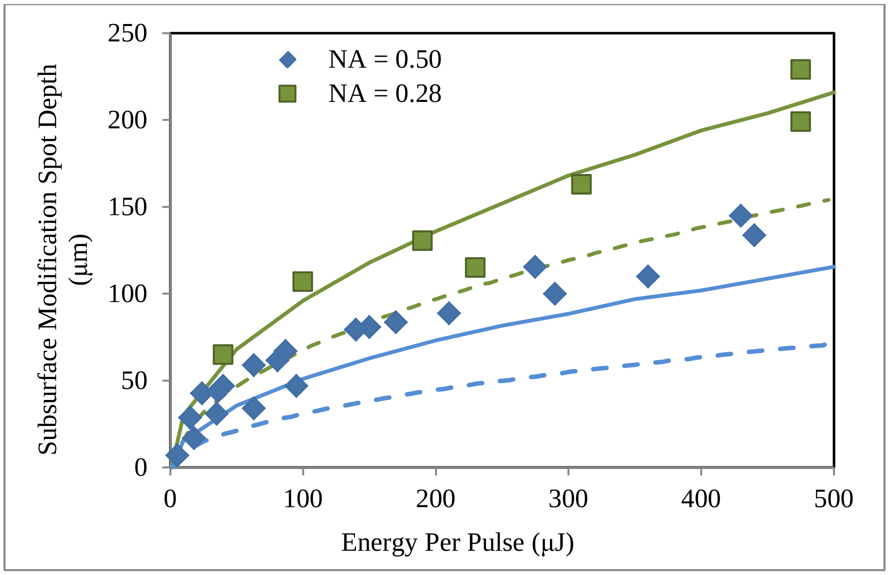

Figure 55: Subsurface laser modification spot depth in sapphire as a function of laser fluence for focus from NA=0.50 and NA=0.28 objectives; observed compared to model results, solid lines are electron-plasma and dashed lines are ray-optics model results

The relationship between spot depth and fluence appears to be proportional to $Epp^{1/2}$ which is consistent with surface ablation results for nanosecond and femtosecond laser sources [116] as well as subsurface femtosecond laser void formation in fused silica [117] and in sapphire [75]. The measured subsurface modification spot depth for 10 laser pulses per damage spot is accurately predicted by the electron-plasma model when multiplied by the correction factor.

Having successfully characterized and modeled the subsurface laser modification process in sapphire at a variety of wavelengths, pulse energies, number of pulses and numerical apertures, the location and volume of damage formed in the bulk could be precisely controlled. With understanding of the methods to control subsurface or bulk laser damage formation in crystalline sapphire, attempts to laser wafer sapphire could ensue.

Chapter 5

SUBSURFACE LASER DAMAGE ARRAYS

This chapter presents the successes and failures of subsurface damage array formation and laser wafering of sapphire. The laser wafering concept revolves around the idea that if dense enough damage is made in a single thin plane beneath the surface, a layer of undamaged material could be lifted off with limited kerf loss. It was proposed that the liftoff process could happen chemically, mechanically or thermo-mechanically once the layer of damage was successfully formed. It can be seen from the following results that subsurface damage arrays of various size and damage density were formed, but no successful liftoff occurred. Two liftoff techniques were pursued; first, a chemical etch using hydrofluoric acid, and second, the application of mechanical stress using various adhesives.

5.1 Subsurface Damage Array Formation

Having characterized control of subsurface damage spot size, depth in the material, and shape, a recipe was designed in the LabView software to form an array of subsurface damage. The recipe used the "SMOOTH" scan mode where stage velocity, scan area, and focal depth could be chosen. In addition, the laser power and wavelength could also be set by the control software as well as other recipe features like a surface ablated outline to the subsurface damage shape or a corner bore mode both of which will be described later. Following is a schematic showing the "SMOOTH" scan recipe functionality (see Figure 56).

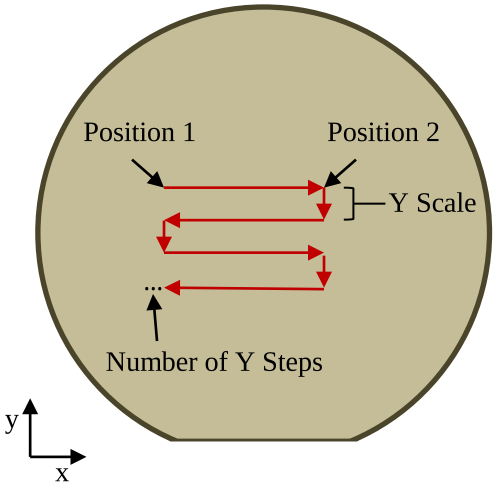

Figure 56: Schematic of laser damage array recipe execution

The LabView recipe for 2D array formation was built to allow for the definition of two x-positions being the start and end position (Position 1 and 2) of the array quadrilateral. Thus the x-side dimension of the array is the difference between the two positions. The y-scale could be specified to determine the distance between row scans, and the number of y-steps could be set to determine the number of scans. Thus the y-side dimension of the array is the product of the y-scale and number of y-steps. The distance between damage spots in the x-direction was set by the x-axis stage scan velocity, and the distance between damage spots in the y-direction was set by the y-scale. The distance between damage spots in the x-direction could be calculated from the laser repetition rate and stage scan velocity such that at 10 Hz and 0.1 mm/s scan, the distance between damage spots (center to center) is 10 µm.

Using the LabView software, subsurface damage arrays could be made of various dimensions and subsurface damage spot densities. Following is an optical microscope image focused into the bulk of the material of three different array recipe settings (see Figure 57).

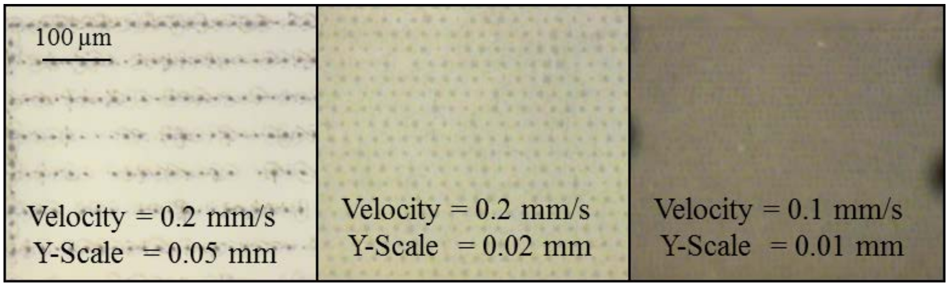

Figure 57: Optical microscope image focused in the bulk of three subsurface damage arrays at different recipe settings. All damage was formed at ~70 µJ pulse energy, 0.50 NA and 667 nm wavelength

As the stage velocity and y-scale were reduced, a denser array of subsurface damage was formed as expected. For an array of 2 mm x 2 mm, the recipe took about 1.5 hours to complete. For a laser wafering process to reach production, kHz or MHz laser repetition rates would need to be used to reduce processing time.

5.2 Liftoff Attempts: Chemical and Mechanical

During the subsurface damage array formation study, it was noticed that for extremely dense damage arrays, where the damage spots significantly overlapped, and the damage plane was in close proximity to the back surface (<80 µm), exfoliation of a layer of sapphire seemed to begin occurring without any further treatment. The appearance of the onset of layer liftoff can be seen in the following microscope images (see Figure 58).

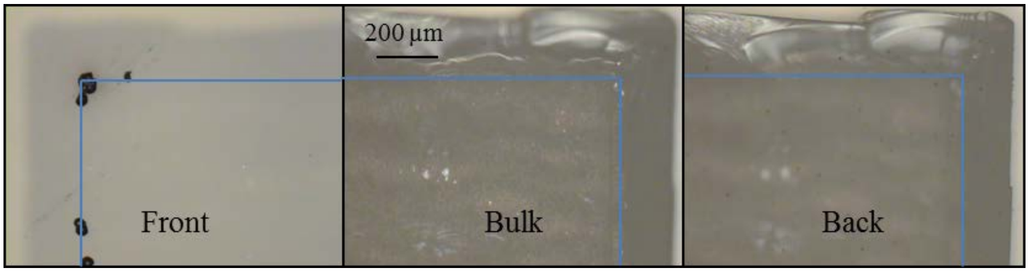

Figure 58: Optical microscope image focused at front, in the bulk, and back of sapphire wafer with subsurface damage array formed at 85 µJ pulse energy, 0.50 NA and 667 nm wavelength. Subsurface laser damage region is outlined in blue.

The scan velocity was 0.1 mm/s and y-scale was 0.01 mm. This means that there was a damage spot formed every 10 µm in both directions. Because 85 µJ pulse energy was used under focus from the 0.50 NA objective, the damage width can be assumed to be about 20 µm meaning that about half the damage region is overlapping with the next damage spot. It can be seen that a shadow region continues outward about 200 µm from the subsurface laser damage region. The shadow region implies a large section of material at a different stress and orientation than the material surrounding around it and because no surface damage is visible, it implies material separation from the substrate has begun. On the "Front" surface microscope image a few spots of surface damage can be seen along the left side of the damage region. These are intentionally the result of a laser drilling recipe intended to observe the effect of chemical etchant on the laser damage as well as provide a preferential etch path from the surface into the bulk laser damage. Having begun to show what is believed to be material liftoff from the high stress region formed in the bulk of the sapphire, investigation into chemical and mechanically aided liftoff began.

The first liftoff technique attempted was a chemical liftoff process in an aqueous solution of hydrofluoric acid (HF). HF has been shown to preferentially etch femtosecond laser damaged sapphire faster than undamaged sapphire. Multiple groups have used subsurface laser damage techniques combined with an HF etch to form micro-channels in the bulk of fused silica [118] and sapphire [119, 120, 121, 122]. An etching ratio of 1:10,000 was measured for crystalline vs. laser amorphized sapphire by Wortmann et al. [120]. Thus an HF assisted chemical liftoff process was attempted. Multiple regions varying subsurface laser damage density and damage plane depth were prepared. Densities from 2.5-50 µm damage spot spacing were formed. Multiple techniques to expose the subsurface damage plane to the etchant were also designed and attempted. As mentioned earlier, one technique used was to laser drill at the corners of the damage region to allow a path for the etchant to the subsurface damage array (see Figure 59).

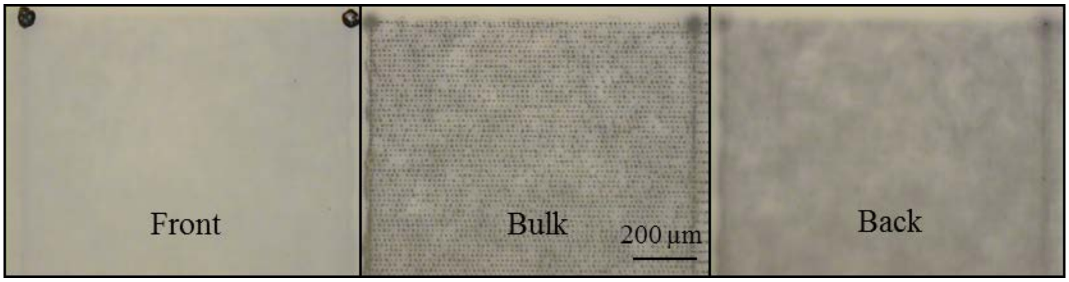

Figure 59: Optical microscope image focused at front, in the bulk, and back side of a sapphire wafer containing a plane of subsurface damage array formed at 70 µJ pulse energy, 667 nm wavelength, and 0.50 NA

The corners were drilled at about 300 µJ pulse energy, and for this example, the stage velocity was 0.15 mm/s meaning subsurface damage spots were 15 µm apart. Another technique involved the formation of surface ablated outline to the subsurface damage region at a depth allowing chemistry to access the bulk laser damage from the sides (see Figure 60).

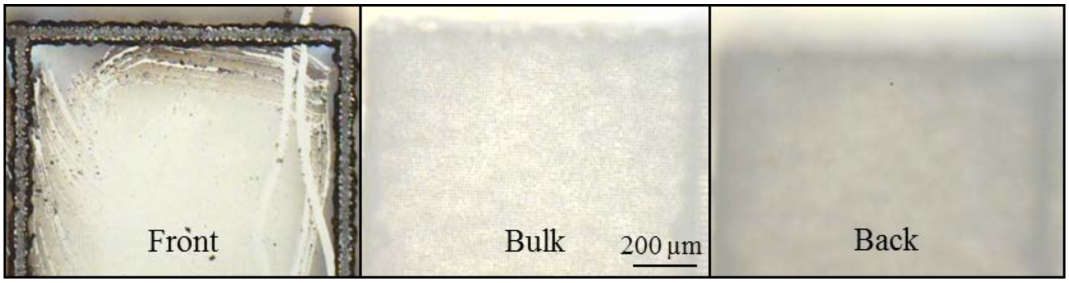

Figure 60: Optical microscope image focused at front, in the bulk, and back side of a sapphire wafer containing a plane of subsurface damage array formed at 57 µJ pulse energy, 667 nm wavelength, and 0.50 NA

The surface ablated outline was formed at 400 µJ pulse energy, and for this example, the stage velocity was 0.10 mm/s meaning the damage spots were 10 µm apart. The final method used to expose the bulk damage to the etchant was to cleave the wafer along the edges of the damage region using a surface or subsurface laser cleave process. All preparation methods were placed in a solution of 49% hydrofluoric acid at room temperature for 4-96 hours. Although not well understood, the etch rate of crystalline sapphire in HF is <0.01 nm/min, but for femtosecond laser damaged sapphire it can reach >80 nm/min [121]. Thus 96 hours should have been plenty of time for the etchant to remove all of the laser damaged material. However, no change was observed using the optical microscope for the laser damaged material at 4,24,48,72, and 96 hours, and no successful layer liftoff occurred. This is best explained by the fact that although the material is permanently modified only in a narrow plane in the bulk of the material, at nanosecond pulse lengths, laser damaged material can recrystallize. So instead of forming an amorphous region of extremely high pressure and stress, which when done with highly focused femtosecond lasers has been shown to form material voids [75], a polycrystalline region might instead be what is formed or might be separating small regions of amorphous damage. There would be little to no improvement in etch rate for polycrystalline sapphire vs. crystalline sapphire, meaning that either femtosecond laser damage would need to be used to achieve the extreme stress required [121], or another liftoff method should be pursued.

Following the failure of chemical assisted layer liftoff, a mechanical liftoff method was pursued. Various adhesives were used to connect a plastic tweezers to the surface of the bulk laser damage regions. After the adhesive was cured, separation was attempted by hand. Krazy Glue®, Super Glue, Gorilla Glue®, and Rubber Cement were all used to attempt layer liftoff. Unfortunately, none of these methods proved successful. The adhesive force between the tweezers edge and the sapphire substrate was not strong enough to overcome the remaining material bonds in the subsurface damage region. Thus continued work would need to occur to achieve full proof of concept of a laser wafering process in sapphire.

Chapter 6:

CONCLUSION AND FUTURE WORK

6.1 Conclusion

In this work, the interaction of high fluence laser light and transparent crystalline materials was studied for the purpose of developing a laser wafering tool. A complete model was developed utilizing ray-optics assumptions and the full Keldysh multiphoton photoionization theory in conjuncture with Thornber's and Drude's impact (avalanche) ionization models to accurately predict the region where permanent material modification could occur. The model described beam propagation, absorption (both linear and non-linear), and material breakdown due to achievement of the critical electron density and strong electron-plasma absorption. It accurately predicted the shape, size, and location of permanently modified material in the bulk of sapphire for multiple focusing optics, laser wavelengths, number of pulses, and a wide range of beam power. The model also helped explain the difficulty encountered in forming and observing subsurface damage in silicon.

An automated stage and variable wavelength nanosecond laser tool were integrated using a custom LabView program to aid in the characterization of wavelength, energy per pulse, numerical aperture and the resulting subsurface damage spot geometry in crystalline sapphire. Damage regions from 50-300 µm depth into the material were controllably formed using 667 nm wavelength laser light and a 0.50 NA reflective objective. By varying energy per pulse and numerical aperture, the thickness of the damage region in the z direction was controlled and observed at 3-250 µm, reflecting the range of potential kerf loss from this wafering technique. A method to dice sapphire using subsurface damage contained entirely in the bulk of the material was also parameterized for the nanosecond laser tool.

Lastly, having characterized the parameters controlling subsurface damage spot formation, arrays of damage were formed in the bulk of a crystalline sapphire wafers to attempt layer liftoff. Multiple samples of varying spot size, depth, spacing, and array area were prepared as well as some additional laser machining processes like outline surface ablation and corner drilling to allow preferential etch penetration. An unsuccessful preferential chemical etch of 49% HF was attempted to remove the laser damaged material and cause layer liftoff. In addition, mechanical liftoff was also attempted using multiple types of household adhesives. However, this method also proved to be unsuccessful. In order to fully define a laser wafering process, other methods of damage layer preparation and/or material liftoff should be attempted.

6.2 Future Work

6.2.1 Model Improvements

The electron-plasma model used to predict subsurface damage geometry in sapphire was based off the Keldysh multiphoton photoionization theory and Thornber's description of avalanche ionization. It assumed negligible electron diffusion, carrier recombination, and an infinite source of electrons. These assumptions are not realistic. There is a corrected equation that limits the number of available electrons to local valance electrons as well as a recombination term. The following equation has been proposed by Wu et al. as a more thorough representation of transient carrier density [64]:

$$\frac{dN}{dt} = (W_{PI} + n_{ava}N)\left(1 - \frac{N}{N_{max}}\right) - \frac{N}{\tau_s} \tag{67}$$

In order to more accurately describe carrier generation and localized carrier density, a term defining maximum electron density in the valance band is included (N_{max}) as well as a recombination lifetime τ_s. N is still the carrier concentration or density as a function of space and time, W_{PI} is the photoionization rate, and n_{ava} is the avalanche ionization rate. These values can be solved for using the same methods as described and solved for in this work; Keldysh multiphoton photoionization and Thornber or Drude impact ionization. Solving the full rate equation including recombination and maximum carrier density might prove to be a more accurate calculation of actual carrier density in time. In addition to a more complete evaluation of transient carrier generation, more modeling effort could ensue to better describe the beam propagation aspect of the model.

Basic ray-optics assumptions were used to calculate the shape and intensity of the beam in space. However, non-ideal effects like spherical aberration, and the nonlinear refractive index were not taken into account. Even though the critical power for self-focusing was not approached in sapphire for any of the modeling or experimental efforts of this work, it could be valuable to include the nonlinear refractive index in the modeling of beam shape especially for silicon. As discussed in the nonlinear theory section of Chapter 2, the nonlinear refractive index of materials can cause filamentation or premature self-focusing at high intensities resulting in surface damage or drilling when bulk damage was expected by the model. By solving for the intensity dependence of the index of refraction, the failures to form and observe subsurface damage in silicon might have been better predicted and more thoroughly explained. In addition, including the nonlinear refractive index would better describe surface reflection at high intensities, which instead was calculated from the linear index of refraction for a given wavelength of light.

It was concluded in this work that phonon interaction and thus thermal effects were insignificant to the modeling of laser material modification in the ones of nanoseconds time scale (<10 ns). However, electron-phonon scattering and thermal diffusion do happen on the pico- and nanosecond time scale [123]. Thus despite the increased complexity of including the thermal effects of linear absorption coefficient and heat diffusion during and after the pulse, they would provide an even more complete description of laser modification in the bulk of a transparent material. Moreover, it has already been shown that at the hundreds of nanosecond time scale, changes in absorption coefficient due to lattice heating and thermal diffusion can accurately describe bulk material modification in silicon [77]. It has also been shown that femtosecond lasers might be fundamentally unable to generate subsurface damage contained in the bulk due the very low surface damage threshold at ultra-short pulse widths [78]. Thus a modeling delineation between short, ultra-short and long pulses should exist, and some balance between the thermal and non-thermal effects could be struck for the various pulse width time scales. By applying a transient heat conduction model after the pulse by calculating material temperature at the focal point, the effect of heat diffusion could be adequately described.

A brief modeling investigation into two-dimensional thermal conduction was performed to observe the effect of heat dissipation after the laser pulse. The model applied 3000 °C to one side of a 10x10 µm array and the model results after 250 ns can be seen in the following figure (see Figure 61).

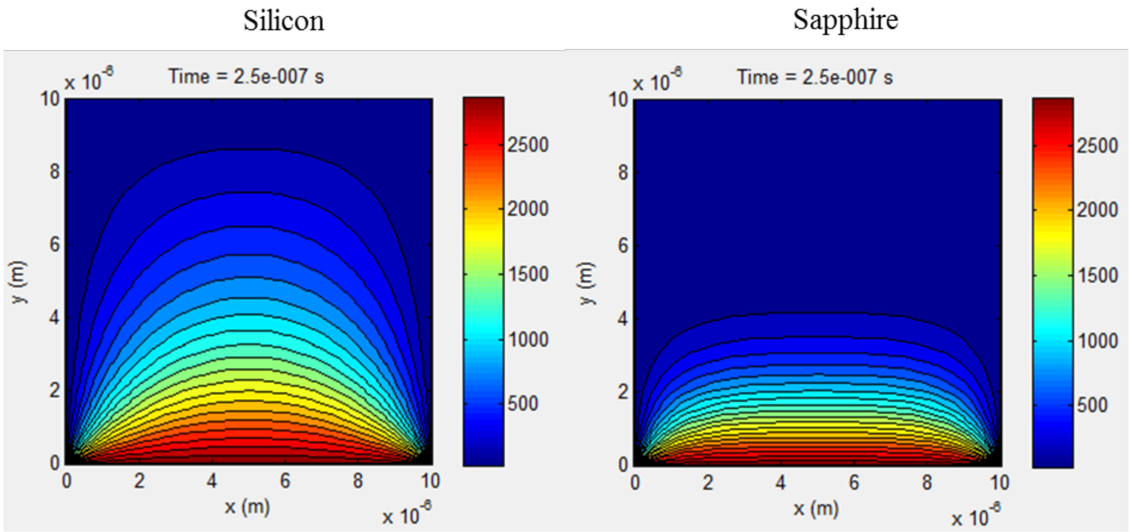
Silicon

Sapphire

Figure 61: Transient Heat Conduction Model results for silicon and sapphire.

It can clearly be seen that 250 ns after the pulse, heat has diffused much further in silicon than in sapphire. In addition, if the melting points of silicon (1414 °C) and sapphire (2040 °C) are taken as assumed material modification thresholds, it can be seen that after 250 ns, about 3 µm of material is affected in silicon and about 1 µm in sapphire. Thermal diffusivity values of 8.9E-6 and 9.2E-5 m^2/s for sapphire and silicon respectively were used in this investigation. This brief thermal modeling effort solidifies the concepts already presented in this paper; although thermal effects are not the most important contributor to the material modification process for nanosecond laser pulses, they are still important for a complete modeling picture, especially in silicon.

6.2.2 Layer Liftoff

Although successful layer liftoff from a laser wafering process did not occur, much progress was made towards understanding laser material interaction and modification in the bulk of a transparent material. There are a few more experimental opportunities that could be pursued and might result in success. Firstly, it was observed that HF did not preferentially etch the nanosecond laser damaged material at the 10,000:1 ratio as reported for femtosecond laser damage [118]. It has been proposed that femtosecond pulse width laser damage is required to achieve the pressure shock necessary to cause amorphization and void formation in the bulk of sapphire [121], where nanosecond damage results in recrystallization [123]. Preliminary studies using a Ti:sapphire Quantronix femtosecond laser system at the ASU Solar Powered Lab were performed. The system produced a pulse train of about ten 130 fs pulses at 1 kHz or 5kHz and 800 nm wavelength. The energy per pulse was in the micro joules, and was filtered down to a few microwatts average beam power. The 0.28 NA gold coated reflective objective was used to focus the beam down to small spot sizes and the motion control was performed by the Innolas system in which the laser was housed. Subsurface damage experimentation was attempted in 2" round double side polished sapphire wafers. Following is an optical microscope image of some of the damage created in a line using the femtosecond laser compared to a single point of nanosecond bulk damage (Figure 62).

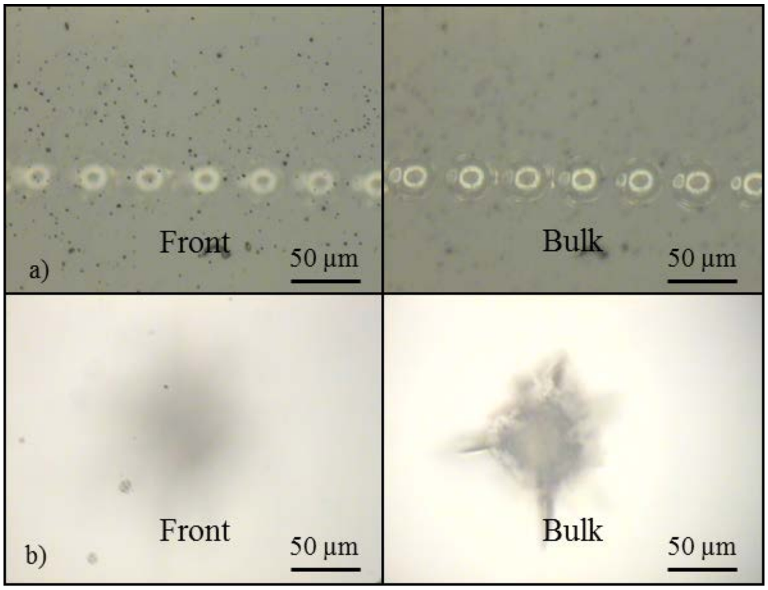

Figure 62: Optical microscope images focused on front surface and in the bulk for a) 130 fs pulse width laser damage and b) 6 ns pulse width laser damage

The damage formed using the femtosecond laser seems to be contained in the bulk of the material, and the modified area is much smaller in diameter using similar average power and optical focus. There also are no visible cracks propagating from the damage pit characteristic of longer pulse width damage. Characterization of the cross section of damage geometry for the femtosecond system using the methods presented in this work will optimize numerical aperture, focal depth, beam power and scan speed and aid in the formation of controlled damage arrays. Arrays of subsurface femtosecond laser damage should have more positive results when processed with the HF etch and could ultimately lead to successful layer liftoff.

Other techniques for mechanically assisted layer liftoff after subsurface laser damage plane formation can be attempted. A thermo-mechanical cleave process could be developed utilizing differences in thermal expansion to induce stress. Through metal deposition of a layer of Al or Ag on the sapphire substrate combined with a heating process, the different stress properties of the materials could induce cleaving. This process has been proven as a method for thin-film silicon wafering using screen printed layers of Ag and Al followed by a 900 C annealing process for bonding. After cooling, the mismatch in coefficients of thermal expansion causes high stress and cleaving of a thin layer of silicon. This process has proven successful in silicon of crystal orientation <100> and <111> [124] and could be adapted for layer liftoff of sapphire.

The laser wafering project originally began with an investigation into subsurface laser damage formation in silicon. As the market for large area thin silicon wafers is very favorable, this investigation should continue. Even though subsurface laser damage was not successfully observed with the nanosecond laser source at a variety of wavelengths from 667-2600 nm, under focus from 0.28-0.75 NA objectives, and at a variety of pulse energies, the investigation should continue. It has been recently reported that laser damage can be formed in the bulk of silicon using NIR (1549 nm) nanosecond pulses (3.5 ns) under 0.70 NA focus using a few micro joules of pulse energy (0.43-5 µJ) [125]. The reported damage was observed using infrared microscopy as well as SEM and optical microcopy on cleaved cross-sections. For the attempts performed in our work, infrared microscopy and cross-sectional optical microscopy imaging techniques were attempted for the variety of wavelengths, pulse energies, and focusing optics listed without successful observation. However, exact recreation of the published methods was not attempted. The use of infrared microscopy as a damage observation technique occurred early during the silicon subsurface laser damage formation investigation and the energy per pulse used for those experiments was far higher than suggested by the published work; thus damage occurred only on the front surface. In addition, the resolution of the infrared microscope system used in the LeRoy Eyring center at ASU is very low. When reasonable pulse energies were later used, a method for successful cleaving along the damage plane was not readily found, and cross-sectional images could not be obtained. It is suggested that an array of subsurface damage formation is attempted in silicon using the methods described in this work and imaged using optical microscopy at the surfaces and infrared microscopy in the bulk to look for subsurface damage. The array will overcome the need for large damage spot sizes due to the low resolution of the microscope system. Other observation methods could be attempted like photoluminescence imaging, or cross-sectional XRT.

REFERENCES

[1] A. Goodrich. et. al., "A wafer-based monocrystalline silicon photovoltaics roadmap: Utilizing known technology improvement opportunities for further reductions in manufacturing costs," *Solar Energy Materials & Solar Cells,* vol. 114, p. 110, 2013.

[2] M. Woodhouse, A. Goodrich, T. James, R. Margolis, D. Feldman and T. Markel, "An Economic Analysis of Photovoltaics versus Traditional Energy Sources: Where are We Now and Where Might We Be in the Near Future?," IEE PVSC, 2011.

[3] J. L. Bromberg, The Laser in America, 1950-1970, 1991.

[4] A. Schawlow and C. Townes, "Infrared and Optical Masers," *Phy. Rev.,* vol. 112, p. 84, 1958.

[5] K. Renk, Basics of Laser Physics, 2012.

[6] A. Chatak, Optics, 2009.

[7] S. Unlimited, "The Worldwide Market for Lasers: Market Review and Forecast 2014," 2014.

[8] M. Rose, "A History of the Laser," 2010. [Online]. Available: http://www.photonics.com/Article.aspx?AID=42279. [Accessed 2014].

[9] E. Gu, C. Jeon, H. Choi and et. al., "Micromachining and dicing of sapphire, gallium nitride and micro LED devices with UVcopper vapour laser," *Thin Solid Films,* vol. 453, pp. 462-466, 2004.

[10] D. Karnakis, E. Illy, M. Knowles, E. Gu and M. Dawson, "High Throughput Scribing for the Manufacture of LED components," *Proceedings of SPIE 5366,* 2004.

[11] T. Lizotte, "Laser Dicing of Chip Scale and Silicon Wafer Scale Packages," in *Electronics Manufacturing Technology Symposium, 2003. IEMT 2003. IEEE/CPMT/SEMI 28th International,* 2003.

[12] A. Tamhankar and R. Patel, "Optimization of UV laser scribing process for light emitting diode sapphire wafers," *Journal of Laser Applications*, vol. 23, no. 3, 2011.

[13] G. Chryssolouris, Laser Machining Theory and Practice, 1991.

[14] M. Perry, B. Stuart, P. Banks, M. Feit, V. Yanovsky and A. Rubenchik, "Ultrashort-pulsed laser machining of dielectric materials," *Journal of Applied Physics,* vol. 85, p. 6803, 1999.

[15] D. P. Korfiatis, K. Thoma and J. C. Vardaxoglou, "Conditions for Femtosecond Laser Melting of Silicon," *Journal of Physics D.,* pp. 6803-6808, 2007.

[16] D. Korfiatis, K.-A. Thoma and J. Vardaxoglou, "Numerical modeling of ultrashort-pulse laser ablation of silicon," *Applied Surface Science,* vol. 255, pp. 7605-7609, 2009.

[17] C. Momma, S. Nolte, B. Chichkov, F. Alvensleben and A. Tunnermann, "Precise laser ablation with ultrashort pulses," *Applied Surface Science,* vol. 109, p. 15, 1997.

[18] J. Meijer, K. Du, A. Gillner, D. Hoffmann, V. Kovalenko, T. Masuzawa, A. Ostendorf, R. Poprawe and W. Schulz, "Laser Machining by short and ultrashort pulses, state of the art and new opportunities in the age of the photons," *CIRP Annals - Manufacturing Technology*, vol. 51, no. 2, pp. 531-550, 2002.

[19] M. Amer, M. El-Ashry, L. Dosser, K. Hix, J. Maguire and B. Irwin, "Femtosecond versus nanosecond laser machining: comparison of induced stresses and structural changes in silicon wafers," *Applied Surface Science,* vol. 242, no. 1-2, pp. 163-167, 2005.

[20] M. Fleischer, "Recent estimates of the abundances of the elements in the earth's crust," *Geological Survey Circular,* vol. 285, 1953.

[21] P. Mints and J. Donnelly, "Photovoltaic Manufacturer Shipments, Capacity and Competitive Analysis 2010/2011," *Navigant Solar Services Program,* 2011.

[22] D. M. Powell, M. T. Winkler, H. J. Choi, C. B. Simmons, D. B. Needleman and T. Buonassisi, "Crystalline Silicon Photovoltaics: a Cost Analysis Framework for Determining Technology Pathways to Reach Baseload Electricity Costs," *Energy and Environmental Science,* 2012.

[23] A. Materials, "Applied Materials Whitepaper: Wafer Wire Sawing Economics and Total Cost of Ownership Optimization," Applied Materials, 2011.

[24] F. Henley, S. Kang, A. Brailove and A. Fujisaka, "Kerf-Free Wafering for High-Volume, High-effeciency c-Si Cell," 2011.

[25] S. Bowden and J. LeBeau, "Laser Wafering," in *Photovoltaic Specialists Conference (PVSC), 2012 38th IEEE,* Austin, 2012.

[26] M. Balkanski and R. Wallis, Semiconductor Physics and Applications, 2000.

[27] J. Palais, Coherent Optical Engineering.

[28] A. Einstein, " Über einen die Erzeugung und Verwandlung des Lichtes betreffenden heuristischen Gesichtspunkt," *Annalen der Physik,* vol. 17, no. 6, pp. 132-148, 1905.

[29] J. M. Palmer, "The Measurement of Transmission, Absorption, Emission and Reflection," in *Handbook of Optics Volume II*, Mcgraw-Hill, 1995.

[30] M. Fukuda, Optical Semiconductor Devices, 1999.

[31] J. Singh, Optical Properties of Condensed Matter and Applications, John Wiley and Sons, 2006.

[32] J. Pankove, Optical Processes in Semiconductors, Curier Dover Publications, 1971.

[33] F. Urbach, "The Long-Wavelength Edge of Photographic Sensitivity and of the Electronic Absorption of Solids," *Phys. Rev.* , vol. 92, p. 1324, 1953.

[34] M. Beaudoin, A. J. G. DeVries, S. R. Johnson, H. Laman and T. Tiedje, "Optical absorption edge of semi-insulating GaAs and InP at high temperatures," *Appl. Phys. Lett.* , vol. 70, p. 3540, 1997.

[35] J. I. Pankove, "Absorption Edge in Impure Gallium Arsenide," *Phy. Rev.*, vol. 140, p. 2059, 1965.

[36] S. Johnson and T. Tiedje, "Temperature dependence of the Urbach edge in GaAs," *Journal of Applied Physics,* vol. 78, no. 9, p. 5609, 1995.

[37] G. Macfarlane, T. McLean, J. Quarrington and V. Roberts, "Direct Optical Transitions and Further Exciton Effects in Germanium," *Proc. of the Phy. Soc.* , vol. 71, no. 5, p. 863, 1958.

[38] M. Sturge, "Optical Absorption of Gallium Arsenide between 0.6 and 2.75 eV," *Phy. Rev.,* vol. 127, p. 768, 1962.

[39] D. K. Schroder, R. N. Thomas and J. C. Swartz, "Free Carrier Absorption in Silicon," *Journal of Solid State Circuits,* vol. 13, p. 180, 1978.

[40] D. A. Clugston and P. A. Basore, "Modelling Free-carrier Absorption in Solar Cells," *Prog. Photovolt. Res. Appl.* , vol. 5, p. 229, 1997.

[41] W. Spitzer and J. Whelan, "Infrared Absorption and Electron Effective Mass in n-Type Gallium Arsenide," *Phy. Rev.*, vol. 114, p. 59, 1959.

[42] H. Casey, D. Sell and K. Wecht, "Concentration dependence of the absorption coefficient for n-and p-type GaAs between 1.3 and .16 eV," *Journal or Applied Physics,* vol. 46, p. 250, 1975.

[43] M. A. Green, "Self-consistent optical parameters of intrinsic silicon at 300 K including temperature coefficients," *Solar Energy Materials and Solar Cells,* vol. 92, p. 1305, 2008.

[44] K. Rajkanan, R. Singh and J. Shewchun, "Absorption Coefficient of Silicon for Solar Cell Calculations," *Solid-State Elect.,* vol. 22, p. 793, 1979.

[45] C. Kittel, Introduction to Solid State Physics-8th ed., John Wiley and Sons, 2005.

[46] P. Franken, A. Hill, C. Peters and G. Weinreich, "Generation of Optical Harmonics," *Phys. Rev. Letters,* vol. 7, p. 118, 1961.

[47] R. Boyd, Nonlinear Optics 3rd ed, Academic Press, 2008.

[48] R. Sutherland, Handbook of Nonlinear Optics 2nd ed, Marcel Dekker, 2003.

[49] J. Leuthold, C. Koos and W. Freude, "Nonlinear Silicon Photonics," *Nature Photonics*, vol. 4, p. 535, 2010.

[50] D. Ristau, Laser-Induced Damage in Optical Materials, CRC Press, 2014.

[51] A. Major, F. Yoshino, I. Nikolakakos, J. Aitchison and P. Smith, "Dispersion of the nonlinear refractive index in sapphire," *Optics Letters,* vol. 29, no. 6, p. 602, 2004.

[52] M. Dinu, F. Quochi and H. Garcia, "Third-order nonlinearities in silicon at telecom wavelengths," *Applied Physics Letters,* vol. 82, 2003.

[53] R. DeSalvo, M. Sheik-Bane, A. Said, D. Hagan and E. Van Stryland, "Z-scan measurements of the anisotropy of the nonlinear refraction and absorption in crystals," *Optics Letters,* vol. 18, no. 3, p. 194, 1993.

[54] M. Sheik-Bahae, D. Hutchings, D. Hagan and E. Van Stryland, "Dispersion of bound electronic nonlinear refraction in solids," *Journ. of Quant. Elec.,* vol. 27, no. 6, p. 1296, 1991.

[55] H. Garcia and R. Kalyanaraman, "Phonon-assisted two-photon absorption in the presence of a dc-field: the nonlinear Franz–Keldysh effect in indirect gap semiconductors," *J. Phys. B: At. Mol. Opt. Phys.,* vol. 39, p. 2737, 2006.

[56] J. Yee, "The Two-photon Transition in Indirect-Band-Gap Semiconductors," *J. Phys. Chem. Solids,* vol. 33, p. 643, 1972.

[57] J. Yee and H. Chau, "Two-Photon Indirect transition in GaP Crystal," *Optics Communications,* vol. 10, p. 56, 1974.

[58] A. Bristow, N. Rotenberg and H. Van Driel, "Two-photon absorption and Kerr coefficients of silicon for 850-2200 nm," *Applied Physics Letters,* vol. 90, 2007.

[59] T. Boggess, K. Bohnert, K. Mansour, S. Moss, I. Boyd and A. Smirl, "Simultaneous Measurement of the Two-Photon Coefficient and Free-Carrier Cross Section Above the Bandgap of Crystalline Silicon," *J. of Quant. Elect.,* vol. 22, no. 2, p. 360, 1986.

[60] V. Gruzdev, "Photoionization rate in wide band-gap crystals," *Physical Review B,* vol. 75, 2007.

[61] L. Keldysh, "Ionization in the field of a strong electromagnetic wave," *Soviet Physics JETP,* vol. 20, no. 5, p. 1307, 1965.

[62] C. Schaffer, A. Brodeur and E. Mazur, "Laser-induced breakdown and damage in bulk transparent materials induced by tightly focused femtosecond laser pulses," *Meas. Sci. Technol.,* vol. 12, p. 1784, 2001.

[63] A. Tien, S. Backus, H. Kapteyn, M. Murnane and G. Mourou, "Short-Pulse Laser Damage in Transparent Materials as a Function of Pulse Duration," *Phys. Rev. Lett.,* vol. 82, no. 19, p. 3883, 1999.

[64] A. Wu, I. Chowduhry and X. Xu, "Femtosecond laser absorption in fused silica: Numerical and experimental investigation," *Phys. Rev. B,* vol. 72, 2005.

[65] E. Arola, "Theoretical Studies on Multiphoton Absorption of Ultrashort Laser Pulses in Sapphire," *Journ. of Quant. Elect.,* vol. 50, no. 8, p. 709, 2014.

[66] A. Vaidyanathan, T. Walker and A. Guenther, "Two-photon absorption in several direct-gap crystals," *Phys. Rev. B,* vol. 21, no. 2, p. 743, 1980.

[67] K. Mikami, S. Motokoshi, T. Somekawa, T. Jitsuno, M. Fujita and K. Tanaka, "Laser-Induced Damage Thresholds at Different Temperature for Optical Devices," *Proc. of SPIE ,* vol. 8786, 2013.

[68] P. Pronko, P. VanRompay, C. Horvath, F. Loesel, T. Juhasz, X. Liu and G. Mourou, "Avalanche ionization and dielectric breakdown in silicon with ultrafast laser pulses," *Physical Review B,* vol. 58, no. 5, p. 2387, 1998.

[69] A. Lietoila and J. Gibbons, "Computer modeling of the temperature rise and carrier concentration induced in silicon by nanosecond laser pulses," *Journal of Applied Physics,* vol. 53, no. 4, p. 3207, 1982.

[70] A. Fridman and L. Kennedy, Plasma Physics and Engineering, CRC Press, 2004.

[71] M. Lenzer, J. Kruger, S. Sartania, Z. Cheng, C. Speilmann, G. Mourou, W. Kautek and F. Krausz, "Femtosecond Optical Breakdown in dielectrics," *Phys. Rev. Lett.,* vol. 80, no. 18, p. 4076, 1998.

[72] B. Stuart, M. Ferit, S. Herman, A. Rubenchik, B. Shore and M. Perry, "Nanosecond-to-femtosecond laser-induced breakdown in dielectrics," *Phys. Rev. B,* vol. 53, no. 4, p. 1749, 1996.

[73] D. Du, X. Liu, G. Korn, J. Squier and G. Mourou, "Laser-induced breakdown by impact ionization in Si02 with pulse widths from 7ns to 150 fs," *Appl. Phys. Lett.*, vol. 64, p. 3071, 1994.

[74] D. McMorrow, W. Lotshaw, J. Melinger, S. Buchner and R. Pease, "Subbandgap Laser-Induced Single Event Effects: Carrier Generation via Two-Photon Absorption," *IEE Transactions on Nuclear Science*, vol. 49, no. 6, p. 3002, 2002.

[75] E. Gamaly and e. al., "Laser-matter interaction in the bulk of a transparent solid: Confined microexplosion and void formation," *Phys. Rev. B*, vol. 73, 2006.

[76] S. Joudkazis, K. Nishimura and H. Misawa, "In-bulk and surface structuring of sapphire by femtosecond pulses," *Applied Surface Science*, vol. 253, p. 6539, 2007.

[77] E. Ohmura, F. Fukuyo, K. Fukumitsu and H. Morita, "Internal Modified-Layer Formation Mechanism into Silicon with Nanosecond Laser," *Journal of Achievements in Materials and Manufacturing Engineering*, pp. 381-384, 2006.

[78] P. Verburg, G. Romer and A. Huis in 't Veld, "Two-temperature model for pulsed-laser-induced subsurface modification in Si," *Applied Physics A*, vol. 114, pp. 1135-1143, 2013.

[79] H. Haus, Waves and Fields in Optoelectronics, New Jersey: Prentice-Hall, 1984.

[80] M. Jeppesen, "Some Optical, Thermo-Optical, and Piezo-Optical Properties of Synthetic Sapphire," *Journal of the Optical Society of America*, vol. 48, no. 9, pp. 629-623, 1958.

[81] J. Ashcom, "The role of focusing in the interaction of femtosecond laser pulses with transparent materials," Harvard university, Cambridge, 2003.

[82] R. S. Quimby, Photonics and Lasers An Introduction, New Jersey: Wiley & Sons, 2006.

[83] I. Malitson, "Refraction and dispersion of synthetic sapphire," *JOSA*, vol. 52, no. 12, pp. 1377-1379, 1962.

[84] W. Primak, "Refractive Index of Silicon," *Applied Optics*, vol. 10, no. 4, pp. 759-763, 1971.

[85] O. Uteza, B. Bussiere, F. Canova, J.-P. Chambaret, P. Delaporte, T. Itina and M. Sentis, "Laser-induced damage threshold of sapphire in nanosecond, picosecond and femtosecond regimes," *Applied Surface Science*, vol. 254, pp. 799-803, 2007.

[86] X. Wang, Z. Shen, J. Lu and X. Ni, "Laser-induced damage threshold of silicon in millisecond, nanosecond, and picosecond regimes," *Journal of Applied Physics,* vol. 108, 2010.

[87] X. Liu, D. Du and G. Mourou, "Laser Ablation and Micromachining with Ultrashort Laser Pulses," *Journ. of Quant. Elect.,* vol. 33, no. 10, pp. 1706-1716, 1997.

[88] J. Poate, Laser Annealing of Semiconductors, Elsevier, 2012.

[89] E. Dobrovinskaya, L. Lytvynov and V. Pishchik, Sapphire Material Manufacturing Applications, 2009.

[90] "PVEducation.org," [Online].

[91] A. Smith and B. Do, "Bulk and surface laser damage of silica by picosecond and nanosecond pulses at 1064 nm," *Applied Optics,* vol. 47, no. 26, p. 4812, 2008.

[92] L. Sudrie, A. Couairon, M. Franco, B. Lamouroux, B. Prade, S. Tzortzakis and A. Mysyrowicz, "Femtosecond Laser-Induced Damage and Filamentary Propagation in Fused Silica," *Phy. Rev. Let.* , vol. 89, no. 19, 2002.

[93] V. Gruzdev, "Photoionization rate in wide band-gap crystals," *Physical Review B,* vol. 75, 2007.

[94] V. Gruzdev and J. Chien, "Laer-induced ionization and intrinsic breakdown of wide band-gap solids," *Applied Physics A,* vol. 90, pp. 255-261, 2008.

[95] H. Guangsheng and S. Liu, Physics of Nonlinear Optics, 1999.

[96] K. Thronber, "Applications of scaling to problems in high-field electronic transport," *Journal of Applied Physics,* vol. 52, p. 279, 1981.

[97] F. e. a. Wang, "Electronic charge transport in sapphire studied by optical-pump/THz-probe spectroscopy," *International Society for Optics and Photonics,* pp. 216-221, 2004.

[98] B. Stuart, M. Fiet, A. Rubenchik, B. Shore and M. Perry, "Laser-Induced Damage in Dielectrics with Nanosecond to Subpicosecond Pulses," *Physical Review Letters,* vol. 74, no. 12, pp. 2248-2251, 1995.

[99] M. Feit, A. Rubenchik, B. Shore, B. Stuart and M. Perry, "Laser-induced damage in dielectrics with Nanosecond to subpicosecond Pulses II. Theory," *Lawerence Livermore National Labratory,* 1994.

[100] A. Oraevsky, L. Da Silva, A. Rubenchik, M. Feit, M. Glinsky, M. Perry, B. Mammini, W. Small and B. Stuart, "Plasma Mediated Ablation of Biological Tissues with Nanosecond-to-Femtosecond Laser Pulses: Relative Role of Linear and Nonlinear Absorption," *IEEE Journal of Selected Topics in Quantum Electronics,* vol. 2, no. 4, p. 801, 1996.

[101] A. Smith, B. Do and M. Soderlund, "Deterministic Nanosecond Laser-induced Breakdown Threshols in Pure Yb3+ Doped Fused Silica," *Fiber Lasers IV: Technology Systems and Applications (SPIE),* vol. 6453, 2007.

[102] M. Kimmel, B. Do and A. Smith, "Deterministic single shot and multiple shot Bulk laser damage thresholds of borosilicate glass at 1.064 μm.," *XLIII Annual Symposium on Optical Materials for High Power Lasers. International Society for Optics and Photonics,* 2011.

[103] K. Davis, K. Miura, N. Sugimoto and K. Hirao, "Writing waveguides in glass with a femtosecond laser," *Optics Letters,* vol. 21, no. 21, pp. 1729-1731, 1996.

[104] R. Moser, M. Ojha, M. Kunzer and U. Schwarz, "Sub-surface channels in sapphire made by ultraviolet picosecond laser irradiation and selective etching," *Optics Express,* vol. 19, no. 24, pp. 24738-24745, 2011.

[105] E. Glezer, M. Milosavljevic, L. Huang, R. Finlay, T.-H. Her, J. Callan and E. Mazur, "Three-dimensional optical storage inside transparent materials," *Optics Letters,* vol. 26, no. 21, pp. 1726-1728, 1996.

[106] E. Website, "www.ekspla.com," [Online].

[107] T. L. Website, "www.thorlabs.us," [Online].

[108] Disco, "DiscoUSA," [Online]. Available: http://www.discousa.com/eg/solution/library/sapphire.html.

[109] M. Kumagai, N. Uchiyama, E. Oshmura, R. Sugiura, A. Kazuhiro and K. Fukumitsu, "Advanced Dicing Technology for Semiconductor Wafer-Stealth Dicing," *IEEE: Transactions on Semiconductor Manufacturing,* pp. 259-265, 2007.

[110] E. O. U. M. a. Objectives, "www.edmundoptics.com," [Online].

[111] D. Ashkenasi, A. Rosenfeld, H. Varel, M. Wahmer and E. Campbell, "Laser processing of sapphire with picosecond and sub-picosecond pulses," *Applied Surface Science,* vol. 120, no. 1-2, pp. 65-80, 1997.

[112] T.-C. Chen and R. Darling, "Parametric studies on pulsed near ultraviolet frequency tripled Nd:YAG laser micromachining of sapphire and silicon," *Journal of Materials Processing Technology,* vol. 169, pp. 214-218, 2005.

[113] P. Mannion, J. Magee, E. Coyne, G. O'Conner and T. Glynn, "The effect of damage accumulation behaviour on ablation thresholds and damage morphology in ultrafast laser micro-machining of common metals in air," *Applied Surface Science,* vol. 233, pp. 275-287, 2004.

[114] H. Varel, D. Ashkenasi, A. Rosenfeld, M. Wahmer and E. Campbell, "Micromachining of quartz with ultrashort laser pulses," *Applied Physics A,* vol. 65, no. 4-5, pp. 367-373, 1997.

[115] C. Schaffer, A. Brodeur and E. Mazur, "Laser-induced breakdown and damage in bulk transparent materials induced by tightly focused femtosecond laser pulses," *Measurement Science and Technology,* vol. 12, no. 11, pp. 1784-1794, 2001.

[116] J. Yoo, S. Jeong, X. Mao, R. Greif and R. Russo, "Evidence for phase-explosion and generation of large particles during high power nanosecond laser ablation of silicon," *Applied Physics Letters,* vol. 76, no. 6, pp. 783-785, 2000.

[117] C. Schaffer, A. Jamison and E. Mazur, "Morphology of femtosecond laser-induced structural changes in bulk transparent materials," *Applied Physics Letters,* vol. 84, no. 9, pp. 1441-1443, 2004.

[118] C. Hnatovsky, R. Taylor, E. Simova, P. Rajeev, D. Rayner, V. Bhardwaj and P. Corkum, "Fabrication of microchannels in glass unsing focused femtosecond laser radiation and selective chemical etching," *Appl. Phys. A,* vol. 84, pp. 47-61, 2006.

[119] M. Jungemann, J. Gottmann and M. Keggenhoff, "3D-Microstructuring of Sapphire using fs-Laser Irradiation and Selective Etching," *Journal of Laser Micro/Nanoengineering*, vol. 5, no. 2, p. 145, 2010.

[120] D. Wortmann, J. Gottmann, N. Brandt and H. Horn-Solle, "Micro- and nanostructures inside sapphire by fs-laser irradiation and selective etching," *Optics Express*, vol. 16, no. 3, p. 1517, 2008.

[121] S. Joudkazis, K. Nishimura, H. Misawa, T. Ebisui, R. Waki, S. Matsuo and T. Okada, "Control of ther Crystalline State of Sapphire," *Advanced Materials*, vol. 18, p. 1361, 2006.

[122] R. Gattass and E. Mazur, "Femtosecond laser micromachining in transparent materials," *Nature Photonics*, vol. 2, no. 4, pp. 219-225, 2008.

[123] S. Sundaram and E. Mazur, "Inducing and probing non-thermal transitions in semiconductors using femtosecond laser pulses," *Nature Materials*, vol. 1, p. 217, 2002.

[124] F. Dross, J. Robbelein, B. Vandevelde, E. Van Kerschaver, I. Gordon, G. Beaucarne and J. Poortmans, "Stress-induced large-area lift-off of crystalline Si films," *Applied Physics A*, vol. 89, p. 149, 2007.

[125] P. Verburg, G. Romer and A. Huis in't Veld, "Two-Photon-Induced Modification of Silicon by Erbium-Doped Fiber Laser," *Optics Express*, vol. 22, no. 18, 2014.